Measurement of Refractive Index and Thickness of Multi Layer Systems Using Fourier Domain Optical Coherence Tomography

Payman Rajai

Thesis submitted to the

Faculty of Graduate and Postdoctoral Studies

in partial fulfillment of the requirements

for the Doctor of Philosophy degree in Physics

Department of Physics

Faculty of Science

University of Ottawa

Abstract

A multilayered system is a good model for many optical systems. An optical coherence tomography (OCT) system can provide fundamental information about the refractive index distribution of the sample and enables images to be corrected for geometric accuracy, but this requires the separation of refractive index and physical thickness for each layer from the measured optical paths. In this thesis a novel approach for simultaneous extraction of index and thickness of multi layer systems and the last medium index of refraction in a single experiment using only the object's spectral response available by any Fourier Domain OCT system without using any additional outside measurements is introduced. The method is based on a novel matrix equation that uses the reflected spectrum from the object and the measured optical thickness. In the presence of slight error of measuring optical thickness, the parameters extraction has wavenumber dependency. A novel method is used to select the suitable set of spectral components that reduces the extracted parameters error. The parameters extraction method is followed by a fitting process for optimized results. The method works the best for low contrast index distribution even in the presence of relatively large optical thickness measurement error.

Acknowledgment

First, and foremost, I would like to express my deepest gratitude to my supervisor, Dr. Rejean Munger for giving me the opportunity to explore a new area in science. I have had a peaceful period under his supervision and his patience gave me the chance to complete this research program. I need also to thank Dr. Henry Schriemer, my co-supervisor, for his encouragement and advice.

During the research period, I received generous and valuable help from my friends and other sources. A very special thanks goes to Mr. Mohammad Salehi for helping me with mathematical derivations. We spent time together and discussed this project. For computer programming and simulation, I received extensive help on Mathcad programming from the PTC Community which saved me great deal of time and I learned many programming skills from them. Mr. Radin Tahvildari introduced me to a great tool for reference managing that saved a lot of time during the writing of this thesis. Finally I would like to thank Mr. Zack Dube, my officemate for his helps and sharing thoughts during this period.

Most importantly, thanks to my parents for their unconditional spiritual and financial support. My father Ahmad and my mother Shahla, all I have is dedicated to them. Also I am grateful to my three lovely sisters Mojy, Gisoo and Rayhi.

Payman Rajai

Dedication

To my father and mother

Table of Contents

List of Tables

List of Figures

Acronyms

Bifocal Optical Coherence Refractometry	BOCR
Diffuse Optical Tomography	DOT
Dynamic Range	DR
Fast Fourier Transformation	FFT
Filtered Backpropagation Algorithm	FBP
Fourier Domain Optical Coherence Tomography	FD-OCT
Generalized Projection Slice	GPS
Low-Coherence Interferometry	LCI
Mutual Coherence Function	MCF
Optical Coherence Tomography	OCT
Optical Diffraction Tomography	ODT
Optical Thickness	OT
Phase Shifting Interferometry	PSI
Signal to Noise Ratio	SNR
Spectral Domain Optical Coherence Tomography	SD-OCT
Time Domain Optical Coherence Tomography	TD-OCT
Transfer Matrix Method	TMM

Chapter 1. Introduction

One of the main and most promising implementation of photonic investigations of structures is Optical Coherence Tomography (OCT). This is a non-invasive interferometric imaging technique that provides morphological cross-sectional information of biological tissues and materials. This technology enables 3D reconstruction of the reflectivity profile of sample structures using a short temporal coherence light source. Under current technology, OCT imaging of structures is based on optical thickness (product of index and layer thickness). In order to find out the optical properties and/or the true structure size of the object under investigation, the separation of refractive index and physical thickness from the OCT measured optical paths is needed.

Non-invasive and direct measurement of the optical properties could have broad industrial and medical applications, from testing optical devices like coating quality and device structure to medical diagnostics like in-vivo imaging of the internal organs. Knowledge of the refractive index of tissue for example, enables earlier disease detection and more accurate diagnosis and better planning of optical treatment and surgery. Some medical diagnostics are directly related to the change in the index distribution in the biological tissue due to altered tissue morphology like breast cancer [1] [2], prostate cancer [3], hemoglobin concentration and oxygenation [4] [5], cornea surgery [6], etc. Therefore non invasive and direct measurement of the refractive index distribution can help to distinguish between

healthy and no-healthy tissues or organs as well as correcting for geometric accuracy.

1.1. Thesis Hypothesis and Goals

The working hypothesis of this thesis is that there is sufficient information in the optical spectrum acquired by currently available implementations of Fourier Domain OCT to extract both the physical structure and the refractive index profile of a stratified medium. Multi layered system is a good model for a wide array of samples when the measurement tool is photonic, (i.e. thin films optics, coating engineering, biomedical optics, material science, atmospheric science). Stratified media were chosen in this research work because (1) They allow a wide design space of biological significance to be explored since indices and thicknesses can be tailored; (2) "mathematical phantoms" can be built for models whose optical responses can be exactly described and so OCT results can be compared for validity.

The goal of this research project is to find a theoretical framework for the analysis of OCT spectral data that decouples refractive index and distance of stratified medium without having previous information about the item under investigation. The goal is also to create a practical methodology to implement this new formulation and validate the accuracy and the range of applicability for practical applications.

1.2. Design and Methodology

In this thesis, a new theoretical framework for solving the problem of decoupling refractive index and physical thickness from the interference spectrum obtained from standard FD-OCT system is going to be introduced. The heart of the formalism

is a matrix equation that uses the interference spectrum and optical thickness obtained from FD-OCT system to extract refractive index and physical thickness of multilayer systems plus the last medium index of refraction.

We will use computer simulations to implement the methodology associated with the new framework. A realistic FD-OCT signal will be generated using Transfer Matrix Method to simulate real life data acquisition. We will use the new formalism to extract two and three layer system parameters (refractive index and thickness of all the layers and the last medium index of refraction) to validate the new framework in perfect situation and realistic situations affected by optical thickness measurement error, noise, etc. We will test the methodology for wide range of index contrasts and thickness of two layer systems. Although there might be applications for the work presented in this thesis outside of the OCT framework, the work presented here is focused on biological applications of OCT.

1.3. Thesis Structure

This thesis work is presented in eight chapters and one appendix. Following the Introduction (this present chapter), the foundation of FD-OCT is presented in chapter 2. Since FD-OCT is founded on optical diffraction tomography (ODT), detailed discussion on ODT and its relation to FD-OCT is given in this chapter. Chapter 3 is a literature review on optical methodologies used for simultaneous index- thickness measurement at fixed illumination-detection angle with normal direction to the object surface, the same restrictions that exist in OCT imaging technique. This chapter also included a history and overview on FD-OCT. The theoretical foundation and methodology of our novel method for simultaneous

index- thickness measurement is given in chapter 4. In chapter 5, the simulation system in this study is discussed. Chapter 6 is the implementation of the theoretical solution in realistic situations in the presence of error in measured optical thickness. In this chapter we explore the impact of optical thickness measurement error on the accuracy of the framework developed in chapter 4 and introduce a method to reduce (or minimize) the impact. In chapter 7, two different optimization approaches are presented that optimize the final outcome of the methodology and the range of applicability of the methodology is explored. Chapter 8 consists of the conclusion about the results obtained and suggestions for future improvements to the introduced method.

1.4. Statement of Contribution

To the best of the author's knowledge, the method for the simultaneous extraction of refractive index and thickness of multi layer systems as well as the methodology introduced for selecting the best spectral components are novel and the only method by now for extracting the object's optical parameters and morphology as well as the last medium index in a single experiment using only the object's spectral response available by any FD-OCT system without using any additional outside measurements.

Chapter 2. Foundation of Fourier-Domain Optical Coherence Tomography

In a typical configuration, OCT records a series of adjacent axial scans (A-scans) to construct a cross-sectional image of the object. Each of the A-scans contains the depth-dependent intensity of reflections or back-scattering in the sample along the beam's path that reaches a static detector that is usually coaxial with the source. Peaks in the processed A-Scan originate at sample sites of refractive index change. The separation between peaks in an A-scan is the optical distance, the product of the refractive index and the geometric distance between. Thus the refractive index profile is the contrast mechanism in the image and allows one to distinguish the optical structure, of the object. In OCT, one uses interference of the sample's signal with a reference optical signal to extract the time of flight (phase) of the signal returning from the sample. This can be implemented using either a Michelson interferometer, a Mach-Zehnder interferometer, or an in-line interferometer [7]. Without loss of generality, we assume a Michelson interferometer to describe an OCT system throughout this thesis and is illustrated in Figure 2.1.

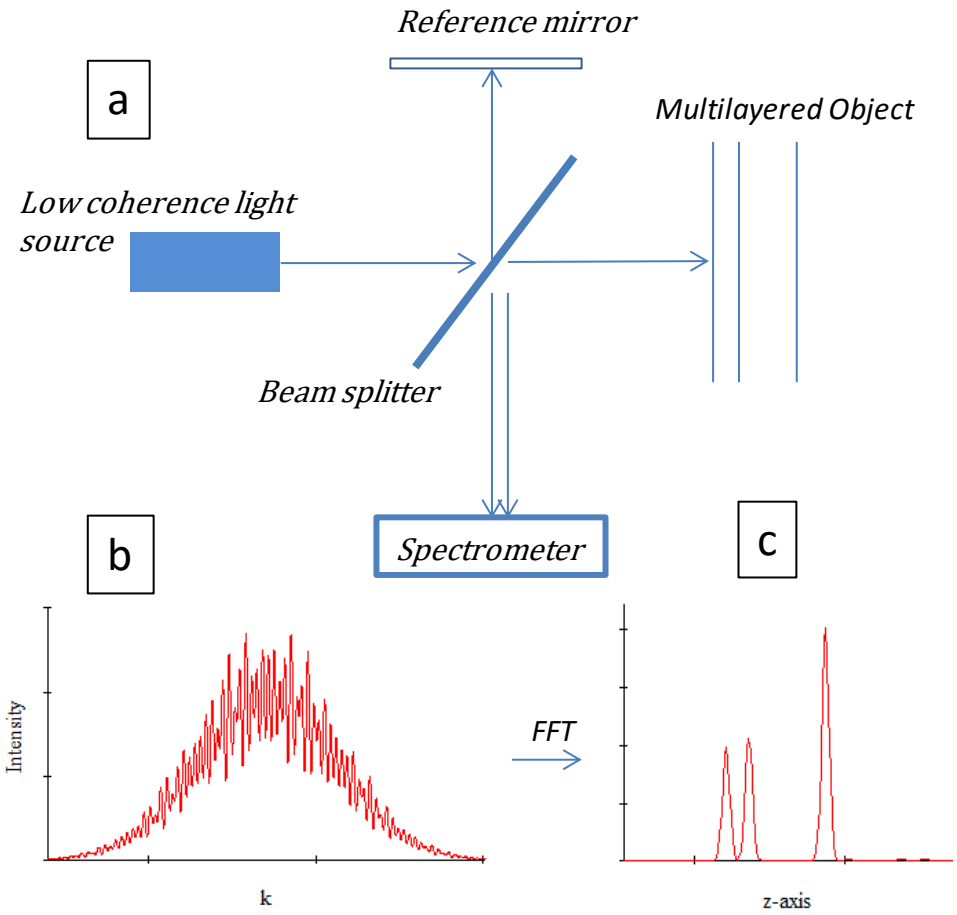

Figure 2.1: a) Michelson interferometer for spectral domain optical coherence tomography. b) Interference spectrum captured by spectrometer. c) The object's reflectivity profile that shows the interfaces position.

For an incident polychromatic plane electromagnetic field propagating in the z direction and linearly polarized in either the x or y direction the electric field is described by

$$E(k,\omega) = s(k,\omega)e^{i(kz-\omega t)}, \qquad (2.1)$$

where $s(k,\omega)$ is the electric field spectral amplitude as a function of the spatial $(k = \frac{2\pi}{\lambda})$ and temporal $(\omega = 2\pi\upsilon)$ frequencies. These frequencies for each spectral component are related by $\lambda\upsilon = c/n$, where n is the index of refraction and c the

speed of light in vacuum. For dispersive media, the refractive index is wavelength dependent. Because of the usually narrow spectrum of light for the source used in OCT, it is usually accepted that n is constant in the treatment of OCT. We also assume that the object is transparent, which means that its refractive index is real, and is an isotropic medium.

The electric field can be decomposed into parallel and perpendicular components (s and p waves) with respect to the plane of incidence. Both s and p states of polarization remain unaltered with propagation through, or reflection from, an isotropic media. Any elliptically polarized field can be obtained by linear combination of the aforementioned components. In this thesis normal incidence is used to conform to experimental requirements. Therefore, there is no distinction between s and p states of polarization so the polarization of the incident electric field is not going to be considered in this study. For this reason we shall employ scalar fields.

Visible light frequencies are on the order of 10^{14} Hz. No detector has the temporal resolution to be able to resolve such oscillations. Detectors actually measure the time average of the intensity, which is proportional to the square of the electric field over a time range much larger than a period of oscillation. We will therefore suppress the time dependence and consider only the spatial part of the fields.

The test OCT technology used throughout this thesis is an implementation of Fourier Domain OCT that can be performed in two ways; spectral domain OCT (SD-OCT) using a spectrometer [8], [9], or swept source OCT (SS-OCT) using a rapidly

tunable laser source [10], [11]. In FD-OCT, the source beam (polychromatic) is split into a probe and a reference beam at a reference mirror fixed in space. The signal returning from the sample is then combined with the reference beam before feeding it into a spectrometric analysis system. All the information about the object is obtained by analyzing the spectral content of the interference signal and is schematically shown in Figure 2.1 . Our focus is on a multi-layered object having a homogeneous and isotropic index of refraction in each segment. This model is not as restrictive as might be first thought since along any given A-Scan, any scattering site can be considered as an interface between two regions (with some size restrictions) and each A-Scan is independent. The system described above is illustrated in Figure 2.1 where the detection system, a spectrometer, is placed at the exit of the interferometry system (Michelson interferometer) and the object's structure is reconstructed from the Fourier transform of the spectral interference signal.

Since FD-OCT described above is an implementation of optical diffraction tomography, in the following section I discuss the foundations of diffraction tomography and show how FD-OCT is a particular implementation of it for backscattered field detection that exploits a multi wavelength illuminating light source.

2.1. The Scalar Theory of Scattering

The study of light- matter interaction starts with Maxwell's equations, which describe the relation between electric and magnetic fields and their interaction with matter. From Maxwell equations one can obtain differential equations that the electric and magnetic field vectors must separately satisfy. We assume that the field

is propagating in a linear[1] and isotropic[2] medium. For regions where both current and charge vanish and the conductivity is zero (i.e. dielectrics), the spatial part of the electric field must satisfy the following differential equation [12],[13]

$$\nabla^2 \boldsymbol{E}(\boldsymbol{r}) + k^2 n^2(\boldsymbol{r})\, \boldsymbol{E}(\boldsymbol{r}) + 2\boldsymbol{\nabla}\big[\boldsymbol{E}(\boldsymbol{r}).\boldsymbol{\nabla}\ln\big(n(\boldsymbol{r})\big)\big] = 0, \tag{2.2}$$

where the vector $\boldsymbol{r}$ denotes a point in space, $k = \omega/c$ is the wave number of the electromagnetic field in free space, and $n(\boldsymbol{r})$ is the spatially dependent index of refraction. The first approximation to simplify this equation assumes that $n(\boldsymbol{r})$ is a slowly varying function of position, and that the change in refractive index over one wavelength is small. This allows the wave equation to take the simpler form [13],

$$\nabla^2 \boldsymbol{E}(\boldsymbol{r}) + k^2 n^2(\boldsymbol{r}) \boldsymbol{E}(\boldsymbol{r}) = 0. \tag{2.3}$$

Since in Eq(2.3) the Cartesian components of the electric field are no longer coupled, the field can be described by a single scalar wave equation. Hence, we can use the scalar form of Eq(2.3) for a scalar field $U(r)$ as [13]

$$\nabla^2 U(\boldsymbol{r}) + k^2 n^2(\boldsymbol{r}) U(\boldsymbol{r}) = 0. \tag{2.4}$$

In diffraction theory, the validity of the scalar treatment is governed by two main conditions: (I) the diffracting aperture (i.e., the size of the inhomogeneity) must be large compared with the wavelength, and (2) the diffracting fields must be observed in the far field (i.e., not too close to the aperture) [14].

For the homogeneous case where $n(\boldsymbol{r}) = constant$ and the incident field is a plane wave, the solution to Eq(2.4) is also a plane wave. While a plane wave

[1] A medium in which the polarisation-vector is parallel and proportional to the electric field
[2] A medium in which physical properties are independent of direction

propagating through a homogeneous refractive index media retains its form, its amplitude will change in transferring from one medium to another. At the interface of two media, the incident field is both partially reflected and transmitted, satisfying the boundary conditions.

Various approaches have been taken to solve Eq(2.4) for an inhomogeneous index distribution: 1) the geometrical optics approximation; 2) perturbation theories that break out along two different paths, the Born (Small Perturbation) and the Rytov (Smooth Perturbation) approximations [15],[16]; and 3) the extended Huygens-Fresnel principle for media that exhibit a random spatial variation in the index of refraction [17]. Since the geometrical optics approximation ignores diffraction effects, which are important in OCT, it will not be discussed in this thesis. The Born and Rytov approximation will be briefly explained in this section and the approach using the extended Huygens-Fresnel will be described in section 4.4.2.

2.1.1. The Born Approximation (Small Perturbation)

Following the treatment given in reference [13], in Eq(2.4), U($\mathbf{r}$) is the total field which includes both the incident and scattered field; i.e., $U(\boldsymbol{r}) = U^i(\boldsymbol{r}) + U^s(\boldsymbol{r})$ and $U^i(\boldsymbol{r})$ satisfies homogeneous Helmholtz equation. So Eq(2.3) can be rewritten as an inhomogeneous Helmholtz equation

$$(\nabla^2 + k^2)U^s(\boldsymbol{r}) = -4\pi F(\boldsymbol{r})U(\boldsymbol{r}), \tag{2.5}$$

where $F(\boldsymbol{r}) = (1/4\pi)k^2[n^2(\boldsymbol{r}) - 1]$ is the scattering potential[3]. Eq(2.5) can be solved using a Green's function approach, where the solution for the scattered field is the convolution of the source term $F(\boldsymbol{r})U(\boldsymbol{r})$ with the Green's function

$$U^s(\boldsymbol{r}) = \int g(\boldsymbol{r} - \boldsymbol{r}')U(\boldsymbol{r}')F(\boldsymbol{r}')d\boldsymbol{r}'. \tag{2.6}$$

The integration is over the volume of the object since outside this region $F(\boldsymbol{r})$ is zero. In Eq(2.6), the left and right hand sides both contain the scattered field and no general solution for the scattered field exists.

One approach for a specific class of problems is to employ a field expansion, where the field is expressed as the sum of ever-smaller perturbations

$$U = U_0 + U_1 + U_2 + \cdots. \tag{2.7}$$

The various approximations define the problem class; i.e., the constraints the system must obey for the approximation to be valid. The Born approximation drops terms higher than U_1, thus demanding that inside the object $|U^s(\boldsymbol{r}')| \ll \left|U^i(\boldsymbol{r}')\right|$ or $|U(\boldsymbol{r}')| \approx \left|U^i(\boldsymbol{r}')\right|$. This therefore neglects multiple scattering, setting a limitation on the applicability of this method [13]. This assumption permits only small fluctuations in refractive index (i.e., a weakly scattering object). The index distribution can then be written as

$$n(\boldsymbol{r}) = 1 + \delta n(\boldsymbol{r})\ ;\ |\delta n(\boldsymbol{r})| \ll 1. \tag{2.8}$$

[3] It is also conventional in diffraction tomography literatures to use $O(\boldsymbol{r}) = [n^2(\boldsymbol{r}) - 1]$ which is called the object function

In this case the scattering potential is reduced to $F(\boldsymbol{r}) \approx k^2 \delta n(\boldsymbol{r})/2\pi$. It has been shown that in the first Born approximation, the solution for the scattered field is [15]

$$U_B^s(\boldsymbol{r}) \cong U_B^1(\boldsymbol{r}) = \frac{k^2}{2\pi} \int g(\boldsymbol{r} - \boldsymbol{r}') U^i(\boldsymbol{r}') \delta n(\boldsymbol{r}') d\boldsymbol{r}', \tag{2.9}$$

where U_B^1 is the first Born approximation. Higher order terms can be obtained by substituting $U^i(\boldsymbol{r}')$ with $U^i(\boldsymbol{r}') + U_B^1(\boldsymbol{r}')$ in Eq(2.9) to obtain the second Born approximation $U_B^2(\boldsymbol{r})$.

2.1.2. Limit of validity

If we define the field components by their amplitudes and phases as per [15]

$$\begin{aligned} U(\boldsymbol{r}) &= A(\boldsymbol{r}) e^{i\varphi(\boldsymbol{r})}, \\ U^i(\boldsymbol{r}) &= A^i(\boldsymbol{r}) e^{i\varphi^i(\boldsymbol{r})}, \\ U^s(\boldsymbol{r}) &= A^s(\boldsymbol{r}) e^{i\varphi^s(\boldsymbol{r})}, \end{aligned} \tag{2.10}$$

then,

$$\ln\big(U(\boldsymbol{r})\big) = \ln\left(U^i(\boldsymbol{r}) + U^s(\boldsymbol{r})\right) = \ln\Big(U^i(\boldsymbol{r})\Big) + \ln\left(1 + \frac{U^s(\boldsymbol{r})}{U^i(\boldsymbol{r})}\right). \tag{2.11}$$

In the Born approximation, where $U^s/U^i \ll 1$, the last term is approximated as $\ln(1 + U^s/U^i) \approx U^s/U^i$ and we obtain the real and imaginary parts as

$$\mathrm{Re}\left(\frac{U^s(\boldsymbol{r})}{U^i(\boldsymbol{r})}\right) = \ln\left(\frac{A(\boldsymbol{r})}{A^i(\boldsymbol{r})}\right), \tag{2.12}$$

and

$$\mathrm{Im}\left(\frac{U^s(\boldsymbol{r})}{U^i(\boldsymbol{r})}\right) = \varphi(\boldsymbol{r}) - \varphi^i(\boldsymbol{r}) = \varphi^s(\boldsymbol{r}). \tag{2.13}$$

In conclusion, from Eq(2.12) and Eq(2.13) we see that for the Born approximation to be valid, it is required that both amplitude and phase fluctuations be small; i.e., $\left|\ln(A(\boldsymbol{r})/A^i(\boldsymbol{r}))\right| \ll 1$ and $|\varphi^s(\boldsymbol{r})| \ll 1$.

The Born approximation is very restricting and is usually only effective for small objects unless the refractive index variation is very small. As per Iwata [18], for a very small spherical object of radius $a \ll 1$ mm and for light in the visible range, the index fluctuation must be as small as $\delta n(\boldsymbol{r}) \sim 10^{-4}$. In biological applications, the thickness of a single biological cell is typically 10 μm, with index perturbations to the medium about 0.03. Thus, the phase delay induced by typical cells is approximately π for a source wavelength of $\lambda = 633$ nm. Therefore, one would not expect the Born approximation to be valid for imaging biological cells even if attenuation is negligible [19], [20].

2.1.3. The Rytov Approximation (Smooth Perturbation)

In order to remove the severe restrictions in the Born approximation, Tatarski introduced the Rytov transformation which is a modified version of Eq(2.4) [21], [15]. In the Rytov approach the field is written in the form $U(\boldsymbol{r}) = \exp(\psi(\boldsymbol{r}))$, or $\psi(\boldsymbol{r}) = \ln(U(\boldsymbol{r}))$. Substituting this into Eq(2.4) transforms the wave equation into a Riccati equation [21]

$$\nabla^2\psi(\boldsymbol{r}) + \boldsymbol{\nabla}\psi(\boldsymbol{r}).\boldsymbol{\nabla}\psi(\boldsymbol{r}) + k^2n^2(\boldsymbol{r}) = 0, \tag{2.14}$$

where $\psi(\boldsymbol{r}) = \psi^i(\boldsymbol{r}) + \psi^s(\boldsymbol{r})$. The field is now represented as a multiplicatively perturbed version of the free space solution rather than an additively perturbed version. From Eq(2.14) for a weakly scattering object ($|\delta n(\boldsymbol{r})| \ll 1$), we obtain [15]

$$\nabla^2\psi^s(\boldsymbol{r}) + \boldsymbol{\nabla}\psi^s.\left(2\boldsymbol{\nabla}\psi^i + \boldsymbol{\nabla}\psi^s\right) + 2k^2\delta n(\boldsymbol{r}) = 0. \tag{2.15}$$

In the Rytov approximation $|\boldsymbol{\nabla}\psi^s| \ll \left|\boldsymbol{\nabla}\psi^i\right| \sim k$. Applying this approximation to Eq(2.15), we obtain the relation between the complex phase and the scattered field as [15]

$$\psi^s(\boldsymbol{r}) = \frac{k^2}{2\pi U^i(\boldsymbol{r})}\int g(\boldsymbol{r}-\boldsymbol{r}')U^i(\boldsymbol{r}')\delta n(\boldsymbol{r}')d\boldsymbol{r}'. \tag{2.16}$$

Comparison of Eq(2.7) with Eq(2.16) shows that $\psi^s(\boldsymbol{r}) = U_B^s(\boldsymbol{r})/U^i(\boldsymbol{r})$. Using the field components as defined in Eq(2.10**)**, the phase in the Rytov approach takes the form [15]

$$\psi^s(\boldsymbol{r}) = \psi(\boldsymbol{r}) - \psi^i(\boldsymbol{r}) = \ln\left(\frac{A(\boldsymbol{r})}{A^i(\boldsymbol{r})}\right) + j\left(\varphi(\boldsymbol{r}) - \varphi^i(\boldsymbol{r})\right), \tag{2.17}$$

and the scattered field in the Rytov approach takes the form

$$U_{Rytov}^s(\boldsymbol{r}) = U^i(\boldsymbol{r})\psi^s(\boldsymbol{r}) = U^i(\boldsymbol{r})\ln\left(\frac{U(\boldsymbol{r})}{U^i(\boldsymbol{r})}\right). \tag{2.18}$$

2.1.4. Limit of validity

The condition $|\boldsymbol{\nabla}\psi^s| \ll \left|\boldsymbol{\nabla}\psi^i\right| \sim k$ can be read as

$$\lambda|\boldsymbol{\nabla}\psi^s| \ll 2\pi, \tag{2.19}$$

therefore this approximation requires that changes in ψ^s be small over distances on the order of one wavelength. Eq(2.19) can also be written as $\lambda\Delta\psi^s/\Delta x \ll 2\pi$. If Δx is chosen on the order of a wavelength, then within that interval the change in ψ^s << 2π. In the Rytov approximation the short range change in scattered phase over one wavelength is critical, no condition is placed on the total phase and amplitude

change across the medium thickness. Hence, unlike the Born approximation, there is no restriction on the size of the object.

The inequality in Eq(2.19) implies a small change in relative amplitude and phase fluctuations over the distance of a wavelength. This can be shown using Eq(2.17) for the real and imaginary part as [22]

$$\lambda \left| \boldsymbol{\nabla} \left(\ln \frac{A(r)}{A^i(r)} \right) \right| \ll 2\pi, \tag{2.20}$$

and

$$\lambda \left| \boldsymbol{\nabla} \left(\varphi(\boldsymbol{r}) - \varphi^i(\boldsymbol{r}) \right) \right| \ll 2\pi. \tag{2.21}$$

For a weakly scattering object, the amplitude condition is always fulfilled since $\delta n(\boldsymbol{r}) \ll 1$. The phase condition implies that the angle of inclination of the ray to the initial direction is small. In order to show this, suppose the wave is propagating in x-direction. Then $\varphi^i(\boldsymbol{r}) = kx$. Since $\varphi(\boldsymbol{r}) = \varphi^i(\boldsymbol{r}) + \varphi^s(\boldsymbol{r})$, we have

$$\begin{aligned} \frac{\partial \varphi(\boldsymbol{r})}{\partial x} &= k + \frac{\partial \varphi^s(\boldsymbol{r})}{\partial x} \\ \frac{\partial \varphi(\boldsymbol{r})}{\partial y} &= \frac{\partial \varphi^s(\boldsymbol{r})}{\partial y} \\ \frac{\partial \varphi(\boldsymbol{r})}{\partial z} &= \frac{\partial \varphi^s(\boldsymbol{r})}{\partial z}. \end{aligned} \tag{2.22}$$

Using Eq(2.21) we obtain $|\partial\varphi(\boldsymbol{r})/\partial x| \sim k$, $|\partial\varphi(\boldsymbol{r})/\partial y| \ll k$ and $|\partial\varphi(\boldsymbol{r})/\partial z| \ll k$. This confirms that the field maintains its original direction as it propagates through the medium.

Both the Born and Rytov approximations produce the same results for small size object having slight difference in refractive index with the surrounding media. For

small size objects with large deviations in refractive index, the Born approximation produces a better estimate of the scattering amplitude. For large size objects with small deviations in refractive index, the Rytov approximation produces a better estimate of the scattered phase [23]. Although the Rytov approximation has shown advantages to the Born approximation for large size objects, the Rytov model is a near field model and thus is not suitable for the more common case of far field detection [24] which is the detection mode in FD-OCT.

2.2. The Basic Theorem of Diffraction Tomography

The solution for the scattered field using either the Born or Rytov approximation for the angular spectrum representation establishes a relationship between the scattered field (projected data) and the internal structure of the object. This is the essence of Fourier diffraction theorem, introduced by Wolf in 1969 [25] for weakly scattering objects. This theorem was, developed for diffraction tomography by Devaney in 1982 as a reconstruction technique [26] and by Fercher for Fourier Domain Optical Coherence Tomography in 1995 [8]. The diffraction tomography theorem provides a frequency domain relation between the object's spatial structure and the measured scattered field. Wolf's solution for the scattered field is valid on any plane external to the object but not necessarily in the far field. The theorem states that within the Born approximation, when an object is illuminated with a plane wave, the Fourier transform of the scattered field measured on a plane on either side of the object, gives the values of the 2-D transform of the object along a spherical surface in the frequency domain. Looking at an object illuminated by a

plane wave from an arbitrary direction with field vector defined by $k\hat{s}_0$ and the outgoing scattered field in any direction defined by $k\hat{s}$, where $\hat{s}_0$and $\hat{s}$ are unit vectors. For the homogeneous part of the scattered field, the Fourier diffraction tomography theorem states that [13]

$$\tilde{F}[k(\hat{s}-\hat{s}_0)] = \frac{ks_z}{2\pi i}\tilde{U}^s\left(ks_x, ks_y; z^{\pm}; s_0\right)e^{\mp iks_z z^{\pm}}. \qquad (2.23)$$

The left hand side of Eq(2.23) is the three dimensional Fourier transform of the scattering potential and the right hand side is the two dimensional Fourier transform of the detected field. The $\pm$ sign indicates the position of the measurement plane on either side of the object. Eq(2.23) can also be adopted with Rytov approximation [27]. In order to access to the Fourier data, either multi-directional or multi wavelength illumination can be used [28]. Also In practical diffraction tomography, the projection data is recorded on a plane perpendicular to the illumination direction to avoid rapid phase variation. The adopted version of Eq(2.23) in rotated coordinates can be found for example in [29].

Note that for each illumination angle in Eq(2.23), the accessible spatial frequency components of the object lie on a sphere, known as the Ewald sphere, centered at $(-k\hat{s}_0)$ with a radius equal to$|K| = |k(\hat{s}-\hat{s}_0)|$. K is called the scattering vector whose end points are the locus of available Fourier component of the scattering potential associated with all possible scattering directions. For each illuminating wavelength, the magnitude of K vector in forward scattering detection is within $|K| \in \left[0, \sqrt{2}k\right]$ and in backward scattering detection $|K| \in (\sqrt{2}k, 2k]$. Therefore, higher Fourier components of the scattering potential (such as discontinuities) can

be more easily detected with backscattered light. Also for two different illuminating wavelengths, as is shown on Figure 2.2, backward scattering detection covers a larger area between two different illuminating wavelengths than forward detection. This implies that using multiple illumination wavelengths increases the range of accessible Fourier components of the scattering potential in the backward detection mode whereas it is ineffective in the forward mode [30]–[32].

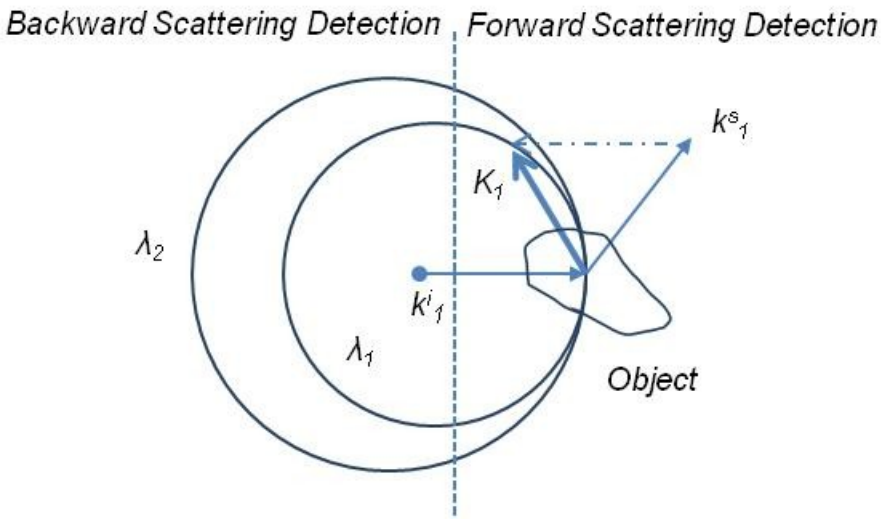

Figure 2.2: The Ewald spheres corresponding to two different illuminating wavelengths λ_1 and λ_2

2.3. Reconstruction Algorithm

In the previous section, it was shown that there exists a relation between the measured scattered field and an object's internal structure (or refractive index distribution). The inverse problem of extracting the object function from the measured scattered field is the ultimate goal of diffraction tomography. In practice, the index distribution of the object is not simply the inverse Fourier transform of Eq(2.23) . This is because we have discrete data sampling and bandwidth limited

data set as well as sometimes irregularly spaced data. So the inverse Fourier transform is not complete. Some reconstruction algorithms have been introduced to deal with these practical limitation [26], [33], [34].

The most popular algorithm is the "Filtered Backpropagation" algorithm. The advantage of this algorithm is that it directly uses the recorded field [26]. This algorithm is derived from the "Filter Backprojection", FBP, algorithm used in X-ray tomography [35]. The inputs to the FBP algorithm are the amplitude and phase of the recorded field. when a light source is used, only the field intensity is directly measured. The phase information can be determined by various methods such as in-line hologram, iterative method or phase shifting interferometry [36]. With the knowledge of both the intensity and the phase of the scattered light, optical diffraction tomography (ODT) techniques are able to reconstruct the complex refractive index profile of semi-transparent objects. Experimental measurements of index gradients have been reported for: optical fibers with 7 μm diameter [37] up to 130 μm [36]; semi-transparent birefringent fibers with diameters in the range 8 - 110 μm [38]; pollen grains (30 μm diameter) [39]; planar gradient-index microlenses [40]; and 6-10 μm polystyrene beads [20]. A major drawback of ODT applicability for measuring refractive-index structure is its low dynamic range for weakly scattering objects. As the result, only structures with small refractive-index variations can be measured.

2.4. Far Field Approximation

In the first order Born approximation, the solution for the scattered field in the far field has a simple form. At distances very large compared with the dimensions of the object ($kr \to \infty$) the Green's function can be approximated by [13]

$$g(\boldsymbol{r}-\boldsymbol{r}') = \frac{e^{ik|\boldsymbol{r}-\boldsymbol{r}'|}}{|\boldsymbol{r}-\boldsymbol{r}'|} \sim \frac{e^{ikr}}{r} e^{-ik\hat{s}.\boldsymbol{r}'}. \tag{2.24}$$

Substituting in Eq(2.9) gives

$$U_B^S(\boldsymbol{r}) = \frac{1}{4\pi}\frac{e^{ikr}}{r}\int F(\boldsymbol{r}')e^{-ik(\hat{s}-\hat{s}_0).\boldsymbol{r}'}d\boldsymbol{r}'. \tag{2.25}$$

Eq(2.25) shows that the scattered field is a spherical wave at distances much larger than the object's size. The integral in Eq(2.25) is the Fourier transform of the scattering potential

$$\tilde{F}[\boldsymbol{K}] = \int F(\boldsymbol{r}')e^{-i\boldsymbol{K}.\boldsymbol{r}'}d\boldsymbol{r}', \tag{2.26}$$

therefore

$$U_B^S(\boldsymbol{r}) \propto \tilde{F}[\boldsymbol{K}]. \tag{2.27}$$

Eq(2.25) implies that for the far field, the scattering potential can be obtained from the inverse Fourier transform of the scattered field.

2.5. Fourier Domain Optical Coherence Tomography

Wolf in his Fourier diffraction theory showed that within the first Born approximation, The three dimensional Fourier components of the scattering potential can be determined from the knowledge of the two-dimensional Fourier components of the scattered field. Fercher [8], was the first to apply the far field

approximation of the diffraction tomography theorem to low coherence interferometry to extract depth profile information from weakly scattering objects. His work was the foundation of Fourier Domain Optical Coherence Tomography. In his work, multi-directional illumination was succeeded by illumination with a multi wavelength source to obtain the necessary Fourier components of the object in a single measurement. The multi wavelength light source must be spatially coherent in order to provide interference between the various reflected light fields. Light sources emitting spatially coherence light with large spectral bandwidth could for example be multi-mode laser diodes or superluminescent diodes.

In the original FD-OCT method, the backward scattered light was detected by a point detector rather than an array of line (or plane) detectors. Thus, only Fourier data along K_z (depth information), as depicted in Figure 2.3, is accessible; i.e.,

$$\tilde{F}[k(\hat{s} - \hat{s}_0)] = \tilde{F}[\boldsymbol{K}] = \tilde{F}[0,0,K_z]. \tag{2.28}$$

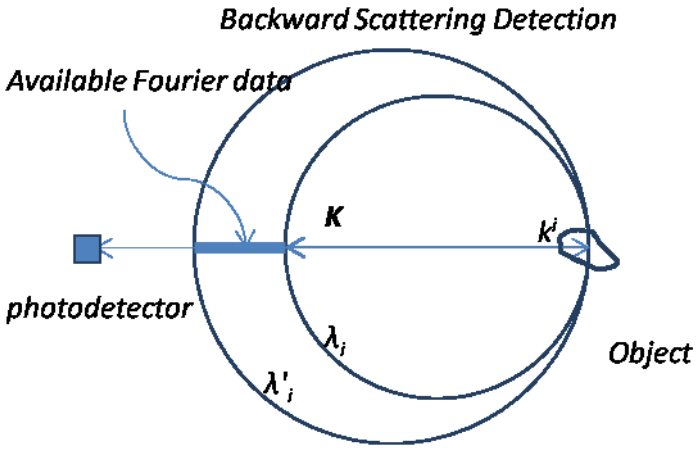

Figure 2.3: Backscattering detection and available Fourier data

In this case, the projection of the scattering potential in the plane normal to the incident field vector is [30], [32]:

$$FT^{-1}\{\tilde{F}[0,0,K_z]\} = \iint F(x,y,z)dxdy = F(z). \tag{2.29}$$

This assumes that the scattering potential is constant in the x and y direction within the illuminated volume of the object. The transverse resolution is thus defined by the width of the illuminating light beam and the longitudinal (depth) resolution from the Fourier uncertainty principle. If we substitute Eq(2.29) into Eq(2.25) and assume a distance D (much larger than the depth of the object structure) between the object and the point detector located at position P, we obtain the scattered field as [8][4]

$$U_B^S(P) = W\frac{e^{ikD}}{D}.FT\{F(z)\}, \tag{2.30}$$

where W is a constant factor of the scattering potential in x and y direction. Therefore, $F(z)$ can be obtained by an inverse Fourier transform of $U_B^S(P)$ if we know both the amplitude and phase of the scattered field. In order to perform the inverse Fourier transform we need to know the backscattered field for a range of k-values. This means that we have to use a multi-wavelength source ("white light source") or a wavelength-tuning source. For a multi-wavelength source, we need to replace the point detector with a spectrometer to measure the scattered field intensity for various wavelength (or wavenumber) components. Fercher's brilliant work showed that the rather complicated theorem (Eq(2.23)) can be reduced

[4] In the original reference, a constant 4π is at the denominator on the right hand side of Eq(2.30). in our notation this factor is inside the scattering potential

(within a reasonable approximation) to a relatively straightforward picture. From Eq(2.30), the detected light intensity is

$$I(P,k) = |U_B^S(P,k)|^2 \propto |FT\{F(z)\}|^2. \tag{2.31}$$

Taking the inverse Fourier transform of both sides of Eq(2.31) yields

$$FT^{-1}\{I(P,k)\} \propto \langle F^*(z)F(z+Z)\rangle = ACF\{F(Z)\}, \tag{2.32}$$

where the star represents complex conjugation, and ACF is the autocorrelation function. The last equality in Eq(2.34) follows from the convolution theorem. Only for very simple objects can the autocorrelation function reveal the true scattering potential. An approach that has been successful in extracting the sample scattering potential is to mix the returning signal with a reference beam (usually obtained by amplitude division of the probe beam) at the detector [8], [41]. In this case the scattering potential can be described as a sum of the object's scattering potential, $F_O(z)$, plus a delta function representing the scattering potential of the reference mirror located at $z = z_R$ [42]:

$$F(z) = F_O(z) + R\delta(z - z_R); \tag{2.33}$$

where R is the beam amplitude reflectivity with respect to the probe beam. Then Eq(2.35) into Eq(2.32) yields

$$\begin{aligned} &ACF\{F(Z)\} \\ &\quad = ACF\{F_O(Z)\} + RF_O{}^*(z_R - Z) + RF_O(z_R + Z) + R^2\delta(Z), \end{aligned} \tag{2.34}$$

where the third term on the right hand side gives the object scattering potential, centered at $Z = -z_R$, and the second term its complex conjugate (mirror image) – these are cross-correlation terms. The first and last terms are the autocorrelations

of the object and the reference mirror (centered at $Z = 0$), respectively. Overlap between cross correlations and autocorrelations can be avoided by setting the difference between reference and probe beam arm length larger than the object's depth.

Chapter 3. Literature Review

Over the last 50 or more years there has been extensive work done on the problem of object reconstruction from scatter data, a full review of this topic is outside the scope of this literature review. We limit the review to papers that are directly relevant to the hypothesis under test - there is sufficient information in Fourier Domain Optical Coherence Tomography (FD-OCT) data to extract both refractive index and distance information from the object under test. The geometry used in FD-OCT reduces the relevant literature to a detection system (a point detector) coaxial with the probe beam in the backscattered direction and considering the case on normal incidence only. FD-OCT theory (see section 2.5 for details) further limits the applicable literature to the measurement of samples where the scattered field << incident field and is from single scatter events only.

In Section 3.1 an overview of FD-OCT technology is presented since the theory in covered in more detail in chapter 2. Section 3.2 presents the relevant literature on the simultaneous measurement of index and thickness in layered system.

3.1. FD-OCT History and Overview

Optical coherence tomography (OCT) is a noninvasive interferometric imaging technique that can be used to obtain high resolution information of a sample's internal structure. OCT is a particular type of tomographic imaging technique. Tomographic imaging is generally used to refer to techniques that obtain cross section images (slice image) from a three dimensional object. "*Tomos*" means section in Greek and a tomogram is an image slice of the internal structure of a

three-dimensional object [43]. OCT has been used almost exclusively for medical imaging, most notably in ophthalmic, but also in: dentistry, neurosurgery, cancer diagnosis, tissue optics, tissue engineering. Further applications have been found in other areas, such as the paper industry, the characterization of optical fibres and polymer composites [44],[45], fingerprint sensing in security and forensics [46] and in the jade industry [47].

OCT was introduced in 1991, well after X-ray, magnetic resonance imaging and ultrasound tomography. It filled a need in the imaging world, especially in biomedical science because optical waves are safer than X-rays, their probing depth is greater than that of ultrasound waves and it is much cheaper to use than MRI. Maybe more importantly, these traditional medical imaging techniques are unable to detect morphological changes at the micrometer level. OCT allows a non–contact way of measuring distances, a great advantage for medical applications, especially for intraocular investigations.

The depth resolution of an OCT system is in the range of $1 - 15$ μm, which is 10– 100 times finer than standard ultrasound imaging [48]. The resolution of clinical ultrasound imaging is typically 0.1– 1 mm as it depends on the imaging frequency (3– 40 MHz). For higher ultrasound frequencies (~100 MHz), a resolution of 15– 20 μm can be achieved. However high frequencies are strongly attenuated in biological tissues [49] limiting measurement depth. Other optical techniques, such as confocal microscopy, can provide, micron level resolution but they suffer from limited imaging depth and are difficult to perform in vivo. By contrast, one micrometer resolution for in vivo OCT imaging has been reported by Drexler using a

femtosecond laser as the light source [50]. Nanometer resolution has also been reported for broad-bandwidth XUV and soft X-ray radiation in OCT [51]. Therefore from the resolution and imaging depth perspective, OCT can fill the gap between optical imaging (confocal and multi-photon microscopy) and conventional clinical imaging (ultrasound, X-ray, MRI) techniques [49].

In OCT, the axial and the transversal imaging resolutions are independent. The axial resolution is mainly determined by the coherence length of the light source and is decoupled from the beam focusing which determines the transverse imaging resolution. In OCT the probe beam sources exhibit short temporal coherence length, high spatial coherence and point-source-like properties some examples would be superluminescent diodes, femto second pulses, wavelength scanning sources.

First generation OCT systems, called Time-Domain OCT (TD-OCT) were first reported in 1991 by Huang et al. for imaging of the human retina in vitro [52]. The first in vivo images (human retina) were obtained in 1993 by Fercher et al. [53] and Swanson et al. [54],[55]. In TD-OCT the reference arm scan depth is used to measure the time-of-flight of the optical signal reflected from the sample. Interference is detected only if the object path length equals the reference path length. For sufficiently short coherence length sources, inhomogeneity sites within the sample will produce independent interference patterns when their positions equal to the reference arm length. Fundamentally, the coherence length of the source should thus be less than or equal to the sample's internal structure scale. This principle makes time domain OCT techniques very useful for imaging discrete features formed either by: layer structures, discrete scatterers, and by mixtures of both.

However, the imaging speed is limited because of the need to scan the reference distance, and it requires sensitive mechanical systems.

Fourier Domain OCT (FD-OCT) was introduced by Fercher in 1995 [8], based on his early insights [56], [57]. Fercher's solution was based on Wolf's inverse scattering solution for weakly scattering objects which provides a relation between the Fourier components of the object's scattering potential and the Fourier components of the scattered field detected outside the object [25]. In FD-OCT, the reference arm is fixed and the internal structure of the object is encoded in the spectral response of the sample field interfered with the reference beam and can be extracted by Fourier transformation. Replacing the moving mirror with a dispersive grating was also introduced independently by Schwider in 1994 to evaluate the surface profile of an object [58]. The spectral information can be obtained either by employing a spectrometer at the exit of the interferometer system (Spectral Domain OCT, SD-OCT) [8],[9] or by using wavelength tuning source (Swept Source OCT, SSOCT) [8],[59]. FD-OCT can be adapted for measurements on the (transparent) eye [8] as well as for measurements of strongly scattering skin [9], [60].

FD-OCT, dramatically improves the detection sensitivity and enables significantly higher scan speeds than earlier TD-OCT [61]–[63]. The short acquisition time, the elimination of moving parts and the inherently direct access to spectral information has made FD-OCT favored over TD-OCT.

FD-OCT does suffer from some artifacts; the signal contains direct current (DC), autocorrelation (AC) and cross-correlation (CC) components. The desired object structure information is embedded in the CC terms. In order to avoid AC and CC

component overlap the mismatch length between the sample and the reference arms should be larger than the optical thickness of the sample. This brings its own issues like higher frequency features in the spectral response which require the use of a higher resolution spectrometer to maintain the same detectable range inside the sample [64]. FD-OCT signals also exhibit conjugate artifacts: since the spectral signal is a real function, its Fourier transform is Hermitian, and the reconstructed image contains both the object and its mirror image. These artifacts can be removed by phase shifting interferometry (PSI) also referred to as Phase Sampling as well as Phase Stepping Interferometry. [41], [65], [66][67].

3.2. Approaches to Simultaneous Index/Thickness Measurements

Multi layered systems are a good modeling approximation widely used in thin films optics, coating engineering, biomedical optics, material science, atmospheric science, etc. In this modeling technique, it is assumed that each layer has homogeneous refractive index, the surface roughness is much less than the incident wavelength and the surfaces are free of local defects. Generally the output of the optical system under the test can be the transmitted and/or reflected light. However in some cases like in the OCT system, there is no access to the transmitted light and only reflected light is available.

Theoretically, reconstructing a multilayer system from an optical probe beam can be done using scanning incident angles and/or scanning probing beam frequencies [68], [69]. In devices like OCT, the direction of the incident light and detection position are fixed at normal incidence / reflection to the sample's surface therefore the only approach to obtain a set of information about the object is to scan a range

of wavelengths. The techniques described below thus summarize those methods of refractive index measurement that use reflection mode and normal illumination direction with respect to the object surface without prior knowledge about the thickness.

3.2.1. Methods Based on Spectral Components

The simplest case is a one layer transparent slab sandwiched between two semi-infinite transparent media. For illumination normal to the slab surface, the detected reflected intensity (Reflectance) which is defined as the ratio of reflected energy to the incident energy is given by [70], [71]

$$R = \frac{{r_1}^2 + {r_2}^2 + 2r_1 r_2 cos\,(2kn_1 d)}{1 + (r_1 r_2)^2 + 2r_1 r_2 cos\,(2kn_1 d)}, \tag{3.1}$$

where n_1 and d are the index and the thickness of the slab and r_1 and r_2 are the Fresnel coefficients at the two surfaces. Oscillations in the spectral intensity profile can be seen from measurements over several wavelengths or use of a multi-wavelength light source as indicated by the $\cos(2kn_1 d)$ term in Eq(3.1). The oscillations show maximums/minimums when the optical path in the sample is an even or odd multiple of quarter a wavelength: $\cos(2kn_1 d) = \pm 1$. There is an analytic relationship between the odd orders of the reflectance extrema and the index of the slab, and between the even orders of the extrema and the last medium index of refraction [72]–[74]. Once the refractive index is obtained, the physical thickness can be extracted from either odd or even orders. This analytic solution for the refractive index and thickness is limited to a one layer transparent slab with total optical thickness of less than half and greater than quarter a wavelength due to

the 2π-ambiguity problem [74]. It is also expected that the index of refraction will have an accuracy of $\pm 1\%$ using this method [73].

Abelès in 1950 introduced another solution from measurement of the reflectance at two different wavelengths. His solution was not an explicit relation and had to be solved by numerical methods [71], [74]. The choice of wavelength was important and better accuracy could be obtained by choosing the wavelengths corresponding to points about halfway down the reflectance curve on either side of the maximum. The method applied to a titanium oxide film and the index determined with accuracy of $\pm 1\%$.

3.2.2. Methods Based on the Envelope of the Spectrum

The idea of using the envelopes of the reflectance spectrum (the tangent curves to the maximum and minimum points of the reflected spectrum) for weakly absorbing thin films was introduced by Kushev in 1986 for semi-infinite substrates [75] and by Minkov in 1989 for finite dimension substrates [76], [77]. They were derived from earlier works based on transmission mode by Manifacier in 1976 for semi-infinite [78] and by Swanepoel in 1983 for finite substrates dimension [79]. For the semi infinite dimension of the transparent substrate and normally incidence light, the envelopes were fitted by a quadratic interpolation to the maximum or minimum points [75]. It was shown that theoretically the real and imaginary parts of the slab's optical properties for a given optical frequency could be obtained from the maximum, $R^{max}(\omega)$, and minimum, $R^{min}(\omega)$, reflectance envelopes at that frequency. This method was tested by simulation on a 2 μm film of SnTe

(semiconductor film) on an infinite transparent substrate of index 1.8. The magnitude of the real part of the slab refractive index ranged from 5 to 6 across the measured spectrum and its imaginary part from 0.5 to 0.09. The simulation results showed accuracy better than 1% for both index and thickness of the film.

For taking into account the effect of the finite dimension of the substrate, the method was tested experimentally for a thin amorphous layer $Ge_{19}As_{21}S_{60}$ on a substrate of index of 1.458 and thickness of 1256 nm. The extracted refractive index (as a function of frequency) ranged between 2.3 to 2.6. The accuracy of the calculated refractive index was reported to be 0.2% and that of the absorption index to be 1.5%. Using an improved algorithm, the errors for the calculated index and thickness were smaller than 0.1% [81].

In 2007 Humphrey suggested using the midpoint envelope for calculating the optical constants and thickness of a thin film deposited on a bulk substrate [80]. The midpoint envelope corresponded to the zero values of the cosine term in Eq(3.1) and provided better accuracy in measuring the thickness of the film. The calculation could also be performed without the need to determine the refractive index or the absorption coefficient of the base substrate. In the reported reference the physical thickness of a thin film of alumina on a glass substrate from the extrema calculation was 569.2 ± 0.4 nm which agreed with the midpoint calculation value of 569.08 ± 0.03 nm.

3.2.3. Immersion Methods

Immersion Spectroscopic Reflectometry (ISR) was another method developed to measure the index/thickness of a transparent thin film [81]–[84]. This method was

also shown to work for multi layer systems (up to three layers). In this method spectral reflectance was measured at normal incidence in various transparent ambient (e.g., liquids) or substrate media. The basic idea of this method was first introduced by Ellis in 1963 for measuring only the refractive index of one layer thin films [85], [86]. Ohlidal in 1980 developed a method for measuring both index and thickness of thin films that was applicable for analysing multi layer systems (up to three layers) if the substrate index of refraction is known. The ambient medium in ISR could be either liquid (liquid immersion spectroscopic reflectometry or LISR) [82] or solid (solid immersion spectroscopic reflectometry or SISR) [83]. The general idea is to modify the environment around the slab using know parameters and to extract the optical properties from the change in spectral response. The two methods differ slightly in implementations. In LISR, different non absorbing ambient media with known indices are used to change the spectral response of the system whilst in SISR a deposited film with known index but with varying thicknesses is used to create different spectral responses. SISR was based on a previously reported technique by Fränz in 1970 which obtained the same information destructively by gradually etching the film thickness [87]. Another ISR implementation based on measuring four spectral reflectances for all combinations of refractive indices of two different transparent ambient media and two different non-absorbent substrates, double-immersion spectroscopic reflectometry (DISR), was also developed for analyzing three layer systems [88].

The foundation of ISR was based on the fact that for a two layer system when the index of the ambient medium matches the index of the film ($n_0 = n_1$), the effect of

the first layer can be eliminated and the reflectance of the system is the same as the reflectance of the system immersed in an ambient of refractive index n_1. In that situation, the problem of finding the optical parameters of a two-layer system would be reduced to analyzing a single layer problem. For a non-absorbing double layer formed on a non-absorbing substrate with known refractive index, the indices of the layers can be obtained from the odd order of the reflectance spectrum oscillations [82]. The same procedure also applies for solid immersion spectroscopic reflectometry [83].

This method was used to analyze non-absorbing single layer of Si_3N_4, non-absorbing double layers of SiO_2, and Si_3N_4 thin films by measuring the spectral reflectance in air and in water. Double-immersion spectroscopic reflectometry was used for triple layers formed by TiO_2 and SiO_2 films ($n_1 = 1.48 \pm 0.03, d_1 = (185 \pm 3)$ nm; $n_2 = 2.41 \pm 0.07, d_2 = (189 \pm 2)$ nm; $n_3 = 1.49 \pm 0.02, d_3 = (195 \pm 5)$ nm) deposited on glass substrates. This last procedure was strongly sensitive to the choice of the initial guesses for the parameters sought in the case of the sample studied were relatively thick so the parameter could not be obtained with sufficient accuracy [88].

3.2.4. Confocal Microscopy Methods

A dual beam confocal microscopy methodology utilizing a single wavelength source was also reported for the simultaneous measurement of thickness and refractive index of a stepped specimen as depicted in Figure 3.1 [89]. In this method the incident 45^o polarized beam was split into its p and s channels using a Nomarski

prism in front of the scanning objective lens. The prism created two closely spaced lateral confocal gates for the two orthogonal polarization states of the laser beam. Each channel was pointed toward two close lateral regions of the object with different unknown thickness d_1 and d_2 and the intensity of each channel was detected separately. The index of the object could then be determined from measuring the travelled distances of the scanning objective lens to the front (h_1 and h_2) and rear surfaces of the object for each channel. This method could not be performed on flat surface samples since the required two channels would not be distinguishable. The experimental validation was performed using a microscope cover glass, with thickness ranging between 165 and 175 μm and with a refractive index of 1.5255. With an objective lens of $NA = 0.25$ the index was measured as $1.512 \pm \%0.8$. With an objective lens of $NA = 0.8$ the index was measured as $1.510 \pm \%1.0$.

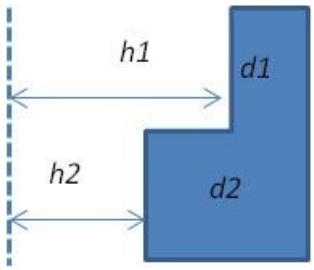

Figure 3.1: A stepped object corresponding to reference [89]

3.2.5. Low Coherence Interferometry and OCT

Multi wavelength light sources produce short coherence light, the wider the source bandwidth the shorter the coherence length. These sources enable optical measurement of samples thicker than a wavelength as inferred earlier in this

review. In Low Coherence Interferometry (LCI) and OCT theory it is shown that optical thicknesses shorter than the source coherence length are not detectable and that the maximum detectable layer thickness is limited by the spectral resolution of the spectrometer for large optical paths [90], [91]. These technologies allow the detection of multiple layers in terms of optical thickness, the geometric thickness multiplied by the refractive index. We discuss below a few approaches that have been tried to decouple the index of refraction and thicknesses in these systems.

3.2.5.1. Focus Tracking Methods

This approach depends on the older OCT technology used in Time Domain OCT to measure the refractive index distribution. This method combines confocal microscope and LCI to decouple the measurements of distance and refractive index. In this method the focus point of the sample arm beam is scanned through the sample from the front surface to the rear surface by moving the sample stage (object scanning) or by moving the focusing lens toward the sample (lens scanning). The physical position of the beam focus is obtained from the confocal signal and the change of phase information is obtained using the scanning reference arm. This method enables the measurement of both the phase and group refractive index (n_p and n_g) of the sample at each point. The measurement accuracy in this method is usually limited by the resolution of translation stages (moving the focus point or the sample) installed in the system.

The first study reported by Tearney in 1995 measured only the refractive index [92]. He determined the refractive indices of BK7 as 1.515 ± 0.01, and fused silica

as 1.458 $\pm$ 0.018. Also he used this method for in vivo measurement of human tissue (stratum corneum, 1.51 $\pm$ 0.02 and epidermis 1.34 $\pm$ 0.01).

Ohmi in 1997 further extended the usefulness of this technique by assuming that the phase and group refractive indices were equal. They performed measurements on z-cut sapphire (Al_2O_3) and glass plates nearly 1 mm thick and on a $LiTaO_3$ plate nearly 0.5 mm thick. Using scanning through the sample by moving the object, an index of refraction measurement accuracy of $\leq$ 0.3% was reported [93]. In another study by Ohmi in 2000 [94], measurements on biological samples such as chicken tissue, human tooth, and human nail were reported for thicknesses ranging from 150 μm to 550 μm with a refractive index range of 1.37 to 1.65 with an accuracy of $\pm$1% assuming that the index of refraction was homogeneous across the sample thickness. In the same study this method was used on a two layer system, a piece of crab-leg crust which consisted of a white viscous layer (the first layer) and semitransparent carapace (the second layer). They were able to obtain individual measurements for each layer ($n_1 = 1.375$, $d_1 = 113$ μm and $n_2 = 1.411, d_2 =$ 147μm) with a reported accuracy of $\pm$1% on all values.

In an attempt to improve on these measurements, the confocal scanning has also been used in combination with spectral domain OCT. In this case optical thicknesses were determined from the Fourier transform of the spectral response data. By moving the objective lens to focus on the front and rear surface of the single layer object, the index and thickness could be calculated. The experiment was performed on liquid solutions (water, air and oil) inside a container 250 μm deep. The measurements were in agreement with reference values within ~1% error range.

When applied to multilayer biological tissues, two fish cornea (overall thickness of 338 μm and 292 μm), three layers were detected. The corresponding index of each layer for the first specimen was measured to be 1.448 ± 0.015, 1.345 ± 0.002 and 1.436 ± 0.009 respectively. For the second specimen, the index for the respective layers was measured to be 1.446 ± 0.011, 1.372 ± 0.005 and 1.392 ± 0.012 [6].

In the Focus Tracking method, if the phase and group index of the object are not the same, another set of information is needed to solve for three unknown (phase index, group index and thickness). The additional information can be the dispersion relation, or quantification of the thickness from an independent method. In one such method [95], [96], the sample is placed in a special holder, between two reference glass plates with known separation. By measuring the gaps between the sample and the glass plates by OCT technique, the single layer thickness can be found independently. The experiment was done on z-cut sapphire, electro optic crystals such as x-cut $LiNbO_3$ and z-cut $LiTaO_3$ plates, fused quartz, flint glass (HOYA FD60), and Crown glass (HOYA BaCD14) and the birefringence of x-cut $LiNbO_3$. The phase and group refractive indices were measured with an error of 0.3% or less. The index range was in the range of 1.45 to 2.25 for the thickness range between 0.5 mm to 1 mm. In separate papers using the special holder approach, similar experiments were performed in Fourier domain OCT [97], [98]. In the reference [97], the samples were Glass slide, BK7 and Fused Silica with thickness about 1000 μm and in reference [98], the measured sample was a slab of ITO glass of thickness ~700 μm where the measurement error was reported around $\sim 7 \times 10^{-4}$ for both the index and thickness.

Sometimes using the special holder is not practical. In these cases if it is possible to obtain an expression for the chromatic dispersion of the Index under. One possible approach to obtain dispersion information is to repeat the measurement with two or more different central frequency sources for a single layer object [99]. This method was used for samples materials of BK7, B270, and CaF_2 , Silica, cover glass, C.C film with wide range of thicknesses between 0.023 mm~ 5.2 mm and group and phase indices ranging between 1.43~1.53. The reported average measurement errors were ~%0.061 in geometrical thickness, ~%0.066 in phase index, and ~%0.057 in group index.

Maruyama in 2000 introduced an approximate expression of the chromatic dispersion in terms of the phase index so that the phase and group refractive index and physical thickness of a single layer object could be determined without special holder [100]. The experiment was reported for single layer samples like z-cut sapphire, x-cut $LiNbO_3$ and z-cut $LiTaO_3$, BaCD14 and Poly vinyl chloride plates. The indices ranged between 1.45 and 2.17 and thickness in the range between 282 μm to 1028 μm and the measurements were reported to have accuracy of 0.3% or better. Separate measurements using this approach was reported on a 500 μm thick fused-quartz plate and a 125 μm thick *z*-cut $LiNbO_3$ plate with accuracy of 0.3% or better [101]. In this reference also a multi point measurement of a radial-graded-index rod lens was made to generate an estimate of the index gradient profile. The using physical stage displacement of 200 μm along the radius of the lens it was shown that the radial distribution of the phase index fitted a biquadratic equation. No more verification about the result was given in this paper.

A generalized formula has been published for the application of the focus scanning method in multi layer systems for both the object [102] and the lens scanning methods [103]. For the object scanning method, the method was tested using a stack of commercial cover slips sample composed of 13 layers of glass and air [102]. Although the layers were detected by the method, no quantitative information about the accuracy of the measured index or thicknesses was reported.

In a more complicated way, bifocal optical coherence refractometry (BOCR) was introduced by Alexandrov in 2003 [104]. The technique was based on the simultaneous creation of two closely spaced confocal gates in a sample by using two lenses in the sample arm beam with different focal lengths such that two axially separated focal points were formed. The optical path-length difference between the gates was measured by means of low-coherence interferometry and used to determine the refractive index. An implementation of this method creating the two confocal gates using an adaptive liquid-crystal lens has also been reported [105]. The experimental measurement reported was *in vivo* measurement of the refractive index of the stratum corneum of the thick skin on the dorsal surface of a human thumb. The refractive index reported to be 1.50 ± 0.02. Also measurements were made of commercially available milk (nominal 2% fat content by volume) at various dilutions.

In a different application, the Focus Tracking method, the sample is moved toward the objective lens so a defocus occurs at the image plane. The objective is then moved to compensate the amount of defocus to obtain optical path distances., In 2012, Min proposed numerically shifting the image plane to find the focusing

position instead of moving the objective [106]. This procedure was shown to be extendible to multilayer systems [107]. The experiment was performed on several combinations of fused silica, BK7 glass and the resolution test target as the first layer and water or oil as the second layer with thicknesses ranging between 0.15 to 1.5 μm. The average errors of the measured indices of layers 1 and 2 were reported to be 0.062% and 0.128% respectively. For thickness measurements, the average errors were 0.180% and 1.394% respectively. For multilayer tests, various combinations of plates and films, up to 7 layers were stacked, on a 0.153 mm thick oil layer. The index and thickness of the oil layer were measured with an average error of 0.065% and 0.990% respectively.

3.2.5.2. Interferometry Methods

In this section another series of techniques for index and thickness measurements of a single layer objects is presented. In the following methods the object was either partially inserted into a Michelson interferometer, or the measurement was performed two times once without sample and once with sample, or sometimes a reference reflector was placed behind the sample.

The first experiment of this type was reported by Fochs in 1950 [113], [75]. He used a white light Michelson interferometer and placed a spectrometer to record the spectral response pattern. The measurement was performed three times, once in the absence of the sample, once in presence of the sample and finally in the presence of the sample but covered the interferometer mirrors. The method gave the thickness of a mica specimen as 12.19 ± 0.02 μm, and the refractive index as 1.601 ± 0.003.

In a similar method, Jin in 2010 used a Michelson interferometer to measure the index and thickness of a single slab where the sample was partially inserted in the sample arm of the interferometer [108]. The spectral response was the combination of the beam travelling in free space and the beam travelling through the sample. The sample optical thickness was measured from the Fourier transform of the spectral response of the perturbed beam. The measurement results obtained from a double-sided polished Silicon wafer with the thickness of 334.85 μm and the index of 3.5 with standard deviation of the index and thickness 0.004 and 0.49 μm respectively. The same theoretical framework was used by Cheng in 2010 with an OCT system having two reference arms and one sample arm [109]. In the first step the OPD between the sample arm and the reference arms was adjusted equal to zero without a sample. Then the sample is placed in the sample arm and the upper reference arm scanned to detect interference signals with the sample signal while the other reference arm was kept fixed. The experiment was performed on a BK7 glass sample with a group refractive index of 1.501 at a wavelength of 1550nm and thickness of 0.71mm and on B270 Glass with the index of 1.52 and thickness of 2.0mm with reported experimental error of 3.81% and 1.1% respectively.

Using an idea first introduced by Sorin in 1992 [110], both thickness and group index measurements were performed using optical low-coherence reflectometry in an arrangement very similar to the OCT system where a reflecting mirror was placed in the sample arm at a known position. The sample was inserted in the sample arm in front of the mirror and the surfaces, including that of the mirror was detected by scanning the reference mirror. The index and thickness could be

obtained from the amount of optical path displacement of the detected reflecting mirror position with the introduction of the sample. The method was performed to measure the thickness (6.753 ± 0.004 mm) and index (1.511 ± 0.001) for a piece of Tygon tubing. Also for two fused silica samples 9 mm and 12 mm where the index was obtained to be 1.4616 with uncertainty of 6×10^{-4} . In another experiment, the combination of LCI with a reflector plate and moving reference arm also reported for measuring PMMA with thickness of 1.9 mm and index 1.6634 with accuracy of 0.04% [111].

In a new implementation of this method, Na in 2009 used FD-OCT instead of TD-OCT and measured a 1.555 mm thick fused silica plate, the thickness was measured at a standard deviation of $\pm 2 \times 10^{-4}$ mm and deviation of $\pm 2 \times 10^{-4}$ in the group index. In another report, this technique was also used to measure the index and thickness of a glass plate ($n \approx 1.5, d \approx 1$ mm) by both TD-OCT and FD-OCT systems. The experiment showed the average error for refractive index and thickness in TD-OCT were 1.74% and 1.65% respectively while the error using FD-OCT was reduced to 0.03% and 0.26% [112].

Using a FD-OCT system, a particularly stepped layer of thin film was used to measure the index of the layer of SiO2 thin-film layers deposited on silicon substrate with thickness ranging from 0.5 to 4.0 μm [113]. The theoretical formula was the same as the technique given in section 3.2.4. The refractive index of the film layer reported to an accuracy of 10^{-3} without prior knowledge of geometrical thickness.
A simultaneous measurement of physical thickness and group refractive index based on the spectral-domain optical low coherence interferometry with two

sample probes facing each other was reported by Park in 2011 [114]. The technique can be used for transparent as well as absorptive or opaque samples. Measurements were made without and with the sample. After Fourier transformation of the interference spectrum, the optical thickness obtained by each probe made it possible to calculate the index and physical thickness. Samples measured thickness ranged from 0.15 mm to 3 mm with indices around 1.5 (Cover glass, BK7, Silica, CaF2, NG9). The average measurement error for the group refractive index and thickness was reported to be ~0.06%.

Tandem interferometer has also used to measure the index and thickness of single layer objects. This technique is insensitive to group delay dispersion and is used for thick samples and broad source spectral line widths. In their experiment three BK7 glass plates approximately 100, 150, and 300 μm thick were set in the interferometers. The index was found with difference from the catalog data by 7×10^{-4} [115]. A variation of this method was reported without employing compensators where the index of BK7 glass plates with thicknesses 10.1 mm and 3.5 mm were measured with difference to the catalog data by 1.852×10^{-4} with a standard deviation of 5.1×10^{-6} [116].

3.2.6. Summary

In summary, the literature on the simultaneous measurement of index/thickness in stratified media is mostly limited to methods that work for one layer systems and its substrate. Double-immersion spectroscopic reflectometry (DISR) was reported to be applicable for three layer films but this method must be done with different ambient and substrate materials with known indices, furthermore the index of the last

medium must be known in this technique. For optical thicknesses larger than a few wavelength, short coherence light source must be used in systems like LCI or OCT. In these applications a reference reflector, or stepped object, or partially inserted object were required to measure the index/thickness of one layer object simultaneously. All the reported techniques for thicker samples were only suitable for one layer objects. The only reported system capable of measuring multi layer system was the Track and Focus technique. The accuracy of this technique is highly dependent on mechanical movement accuracy.

Chapter 4. Theoretical Framework for the Simultaneous Measurement of Index/Thickness in Multilayer Systems

In this chapter we present the theoretical framework on which the methodology used to provide the simultaneous measurement of refractive index and thickness is based. This framework includes a model of the sample signal based on the simple summation method and a methodology for extracting the needed information from the resulting FD-OCT signal.

4.1. The Summation Method

In the FD-OCT arrangement discussed in chapter 2, the field from the reference arm is interfered with the field reflected from the object. In order to describe the interference signal, we model the expected signal using the summation method in which the field components arising from multiple scattering between interfaces (multiple reflections) inside the sample are neglected. This approximation is valid as long as the second orders of reflectance are negligible. For most samples such as biological tissues imaged with OCT, the sample reflectance at interfaces are typically very small (on the order of 10^{-4} to 10^{-5}) [117]. Therefore for biological applications, the summation method is a good approximation to describe the total reflected field from the sample. Within this approximation, the total field reflected from the sample is the sum of the fields from each discrete reflector as depicted in Figure 4.1.

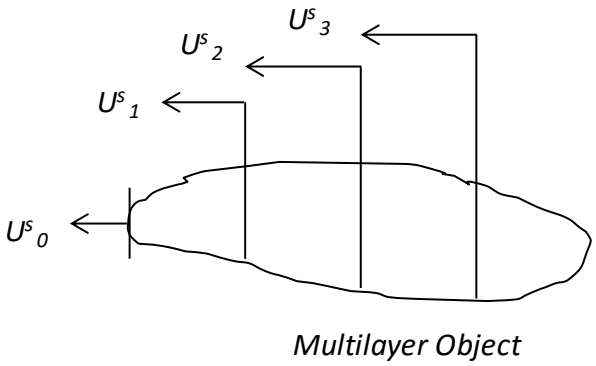

Figure 4.1: The total field reflected from the sample is the sum of the fields from each discrete reflector.

In the system under consideration a short coherence light field is sent to a Michelson interferometer in which one arm contains the reference mirror and the other arm contains the multilayered sample, Figure 4.2. In the modeling the incident field is set to be a unit amplitude plane wave. At the beam splitter position the field reflected from the reference mirror has traveled a round trip distance $2\mathcal{Z}_R = 2n_0 z_R$. The reference reflected field, U^R, is then given as

$$U^R(k) = r_R s(k) e^{i2k\mathcal{Z}_R}, \tag{4.1}$$

where r_R represents the reflectivity of the reference mirror and $s(k)$ is the source spectral amplitude.

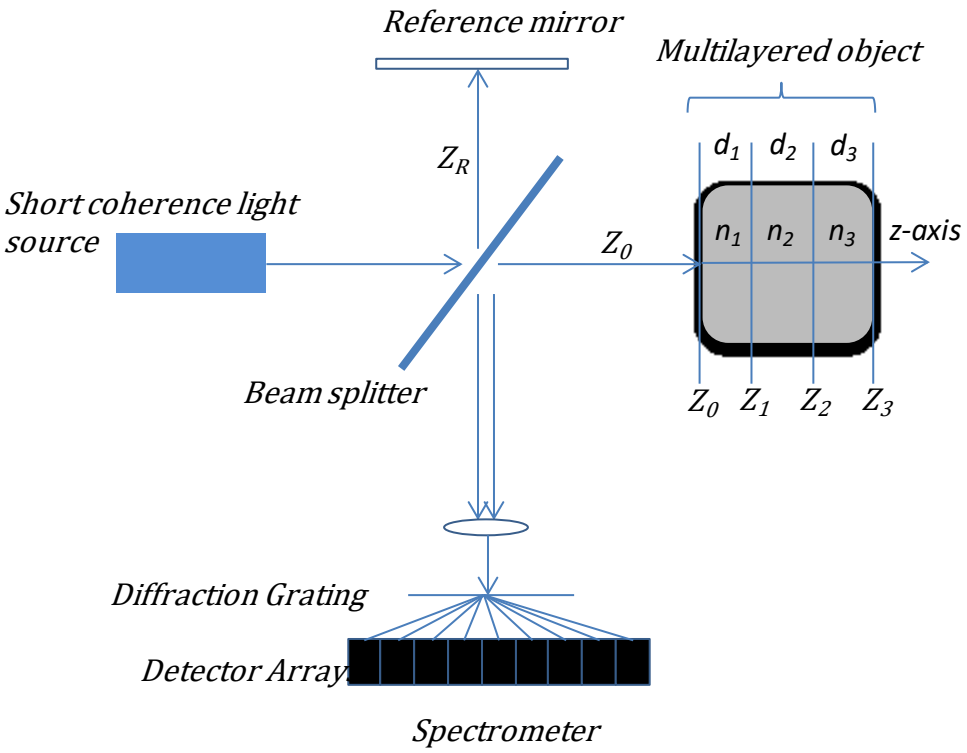

Figure 4.2: Schematic presentation of the FD-OCT system. $\{n_i, d_i\}$ represent the index and thickness of each layer of the sample.

The total field reflected from the object at the beam splitter position is the sum of the fields reflected from each interface is [45]

$$U^s(k) = (U^s{}_0 + U^s{}_1 + U^s{}_2 + \cdots) = s(k)\sum_0^N r_j e^{i2k\mathcal{Z}_j} = s(k)\sum_0^N r_j e^{i2k\sum_{l=0}^{j} n_l d_l}, \tag{4.2}$$

where N is the number of layers; n_l and d_l are the refractive index and the physical thickness of the l^{th} layer; the r_j terms are the field amplitudes reflected from each layer; and the $\mathcal{Z}_j$'s are the optical paths of each interface to the beam splitter

position with $\mathcal{Z}_0 = n_0 d_0$. The detected signal intensity by the detector after interference between the two arms is

$$I(k) = |U^R + U^s|^2 = (U^R + U^s) \times (U^R + U^s)^*, \tag{4.3}$$

where the star sign indicates the complex conjugate. The expansion of Eq(4.3) yields [117]

$$\begin{aligned} I(k) = S(k)\{|r_R|^2 + |r_1|^2 + |r_2|^2 + \cdots\} \\ +2S(k)\left\{\sum_{n=0}^{N} r_R r_n \cos[2k(\mathcal{Z}_R - \mathcal{Z}_n)]\right\} \\ +2S(k)\left\{\sum_{n\neq m=0}^{N} r_n r_m \cos\left[2k(\mathcal{Z}_m - \mathcal{Z}_n)\right]\right\}, \end{aligned} \tag{4.4}$$

which describes the spectral response of the FD-OCT system. Eq(4.4) contains three group of terms.

1. The first group, the constant or DC terms consists of terms independent of the path lengths of the layers.

2. The second group contains cross correlation terms (CC) dependent on the optical path length difference between each interface and the reference mirror.

3. The last group contains autocorrelation terms (AC) due to the interference between fields from the different interfaces.

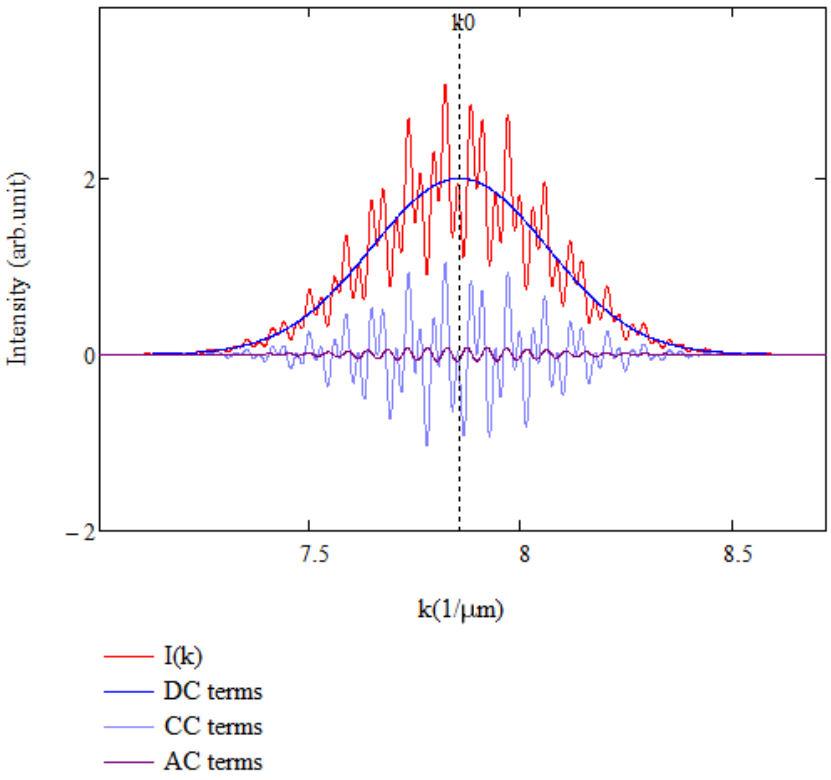

Figure 4.3: Spectral interference pattern and its components for a single layer object.

As discussed earlier, the Diffraction Theorem allows us to do a Fourier transform of Eq(4.4) to obtain the object's scatter function. The Fourier transform of Eq(4.4) is

$$
\begin{aligned}
i(z) = \\
\Gamma(z)\{|r_R|^2 + |r_1|^2 + |r_2|^2 + \cdots\} + \\
\Gamma(z) \otimes \sum_{n=0}^{N} r_R r_n \, \delta[\mathrm{z} \pm 2(\mathcal{Z}_R - \mathcal{Z}_n)] + \\
\Gamma(z) \otimes \sum_{n \neq m = 0}^{N} r_n r_m \, \delta[z \pm 2(\mathcal{Z}_m - \mathcal{Z}_n)],
\end{aligned}
\tag{4.5}
$$

where $\otimes$ is the convolution operator and $\Gamma(z)$ is the Fourier transform of the source power spectrum. Using the sifting property of the Dirac delta function we can write,

$$i(z) =$$

$$\Gamma(z)\{|r_R|^2 + |r_1|^2 + |r_2|^2 + \cdots\} +$$

$$r_R r_n \sum_{n=0}^{N} \Gamma[\mathrm{z} \pm 2(\mathcal{Z}_R - \mathcal{Z}_n)] + \tag{4.6}$$

$$r_n r_m \sum_{n \neq m=0}^{N} \Gamma[z \pm 2(\mathcal{Z}_m - \mathcal{Z}_n)]\,;$$

where $i(z)$ is an A-scan of the FD-OCT image and contains the entire information about the sample reflectivity and thus its structure along that beam path. It is, in general, a complex function and only its magnitude is used to construct the image. This equation is the sum of three groups of terms, DC, CC, and AC, respectively and they are shown on Figure 4.4 for a two layer system as an example. As we can see from Eq(4.6), the image of the FD-OCT system reveals the structure of the object based on the optical thickness where the refractive index and physical thickness of each layer are coupled together.

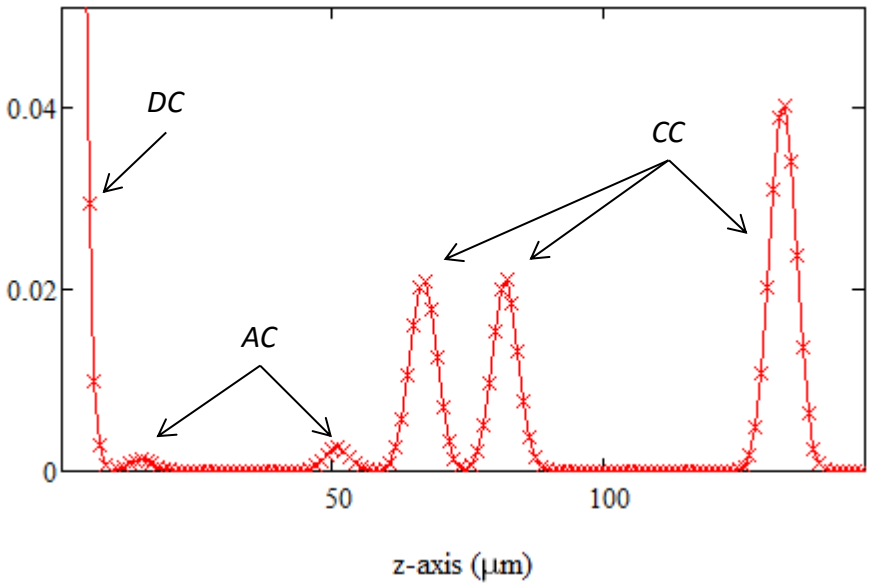

Figure 4.4: Plot of $i(z)$ corresponding to a two layer system. DC, AC and CC terms are indicated on the plot. Mirror images have been removed.

Usually the reflectivity of the reference mirror is much stronger than the reflectivity of the sample layers. Therefore the DC terms provides a strong background light. The constant terms correspond to zero spatial frequency and appear at the position $z = 0$. The autocorrelation terms also do not depend on the mismatch arm's length $(\mathcal{Z}_R - \mathcal{Z}_0)$ and their positions are fixed. Therefore there is a chance that images due to the AC and CC terms overlap each other. In order to avoid this, the mismatch arm's length should be large enough to send the CC image further than the AC image. A FD-OCT signal also exhibit conjugate artifacts as can be seen from the +/- components in Eq(4.6). These occur because the spectral signal is a real function, hence its Fourier transform is Hermitian and the reconstructed image must be symmetrical about $z = 0$ which leads to mirror images. In conventional FD-OCT system, the DC and AC terms as well as the mirror images are considered

unwanted noise terms. The DC terms can be simply removed from the spectral interference by blocking one arm and measuring the spectral intensity of the other arm and then subtracting it from the total signal. There is also a phase shifting interferometry technique that can be used remove DC, AC and mirror images [41], [65], [66][67].

The peaks amplitude of the CC terms in Figure 4.4 depends on the index difference between the two sides of an interface. However they cannot be used to measure the indices since we cannot measure the whole light incident on and reflected from a particular interface. Furthermore no information is available about the sign of the reflectivity (low to high index or vice versa) of the targeted interface. With OCT we are normally looking into highly inhomogeneous scattering samples. That means the amount of light that we can collect from a certain depth in the sample depends on many other factors besides the refractive index distribution (local density and size distribution of scattering objects in the bulk sample, configuration of the imaging optics, position of the focus, etc.).

Therefore, in order to find the true interfaces reflectivity (both amplitude and phase), we may look at the spectral response rather than the Fourier transformed data. This approach was first used by Tomlins in 2006 for the simultaneous index/thickness measurement using FD-OCT system [44], [45], [118]. In his proposed method, Tomlins fitted the spectrum to a modeled signal searching for index and thickness. A computer program had to search for wide range of all possible index and thickness combinations until it found the best fit. Since this approach is purely a

fitting process without measuring index/thickness, this thesis attempts to find a more direct means to obtain this information.

In search for a new approach, we first consider the 2 layer case and expand Eq(4.4) into its individual components:

$$I_{sum}(k) = S(k)(1 + {r_1}^2 + {r_2}^2) +$$

$$2S(k)\{r_1 cos(2k\Delta_{rz_0}) + r_2 cos[2k(\Delta_{rz_0} - \delta_1)] + r_3 cos[2k(\Delta_{rz_0} - \delta_1 - \delta_2)]\} \quad (4.7)$$

$$+2S(k)\{r_1 r_2 cos(2k\delta_1) + r_1 r_3 cos[2k(\delta_1 + \delta_2)] + r_2 r_3 cos(2k\delta_2)\}$$

Here, $\Delta_{rz_0} = \mathcal{Z}_R - \mathcal{Z}_0$ is the mismatch in arm length in a medium with refractive index n_0, $\delta_1 = n_1 d_1$ and $\delta_2 = n_2 d_2$ are the optical thickness of each layer and $S(k)$ is the source power spectral density. The normalized signal after removing the DC and AC terms (as per our earlier discussion) is

$$\begin{aligned} I(k) &= \frac{I_{sum} - DC - AC}{2S(k)} \\ &= r_1 \cos(2k\Delta_{rz_0}) + r_2 \cos[2k(\Delta_{rz_0} - \delta_1)] + r_3 \cos[2k(\Delta_{rz_0} - \delta_1 - \delta_2)], \end{aligned} \quad (4.8)$$

where r_1, r_2, r_3 are the Fresnel coefficients and related to index contrast as

$$r_1 = \frac{n_0 - n_1}{n_0 + n_1}, r_2 = \frac{n_1 - n_2}{n_1 + n_2}, r_3 = \frac{n_2 - n_3}{n_2 + n_3}. \quad (4.9)$$

In the next section, we develop a new mathematical formalism to measure indices from Eq4.8 and Eq(4.9) .

4.2. Illustrating the Mathematical Formalism- The Two Layer System

4.2.1. Matrix Formulation

In this section a method is introduced for the simultaneous measurement of index/thickness in a two layer system without previous knowledge about the actual thicknesses of the layers. The starting input point for the new approach is the optical thickness (OT) of each layer (δ_1, δ_2), which is the output from a conventional FD-OCT. When this information is fed back into the signal presented in Eq(4.8), the only unknowns left are the Fresnel coefficients. For a two layer system with three interfaces, there are three Fresnel coefficients to be calculated. Therefore we need three independent equations to solve for the hree unknowns. We can choose three appropriate values of k (k_1, k_2, k_3) such that their application in Eq(4.8) gives three linearly independent equations as follows [5]

$$\begin{aligned} I(k_1) &= r_{(1)}\cos\left[2k_1\left(\Delta_{rz_0}\right)\right] + r_{(2)}\cos\left[2k_1\left(\Delta_{rz_0}-\delta_1\right)\right] \\ &\quad + r_{(3)}\cos\left[2k_1\left(\Delta_{rz_0}-\delta_1-\delta_2\right)\right], \\ I(k_2) &= r_{(1)}\cos\left[2k_2\left(\Delta_{rz_0}\right)\right] + r_{(2)}\cos\left[2k_2\left(\Delta_{rz_0}-\delta_1\right)\right] \\ &\quad + r_{(3)}\cos\left[2k_2\left(\Delta_{rz_0}-\delta_1-\delta_2\right)\right], \\ I(k_3) &= r_{(1)}\cos\left[2k_3\left(\Delta_{rz_0}\right)\right] + r_{(2)}\cos\left[2k_3\left(\Delta_{rz_0}-\delta_1\right)\right] \\ &\quad + r_{(3)}\cos\left[2k_3\left(\Delta_{rz_0}-\delta_1-\delta_2\right)\right]. \end{aligned} \tag{4.10}$$

These equations can be presented as a matrix equation

[5] The Fresnel coefficient's indices are indicated by parentheses to not be confused with the wavenumber indices.

$$\begin{bmatrix} I(k_1) \\ I(k_2) \\ I(k_3) \end{bmatrix}$$

$$= \begin{bmatrix} \cos(2k_1\Delta_{rz_0}) & \cos[2k_1(\Delta_{rz_0}-\delta_1)] & \cos[2k_1(\Delta_{rz_0}-\delta_1-\delta_2)] \\ \cos(2k_2\Delta_{rz_0}) & \cos[2k_2(\Delta_{rz_0}-\delta_1)] & \cos[2k_2(\Delta_{rz_0}-\delta_1-\delta_2)] \\ \cos(2k_3\Delta_{rz_0}) & \cos[2k_3(\Delta_{rz_0}-\delta_1)] & \cos[2k_3(\Delta_{rz_0}-\delta_1-\delta_2)] \end{bmatrix} . \begin{bmatrix} r_{(1)} \\ r_{(2)} \\ r_{(3)} \end{bmatrix}, \tag{4.11}$$

which can be solved for the Fresnel coefficients as

$$\begin{bmatrix} r_{(1)} \\ r_{(2)} \\ r_{(3)} \end{bmatrix} = \boldsymbol{P}^{-1} \begin{bmatrix} I(k_1) \\ I(k_2) \\ I(k_3) \end{bmatrix}, \tag{4.12}$$

where

$$\boldsymbol{P} = \begin{bmatrix} \cos(2k_1\Delta_{rz_0}) & \cos[2k_1(\Delta_{rz_0}-\delta_1)] & \cos[2k_1(\Delta_{rz_0}-\delta_1-\delta_2)] \\ \cos(2k_2\Delta_{rz_0}) & \cos[2k_2(\Delta_{rz_0}-\delta_1)] & \cos[2k_2(\Delta_{rz_0}-\delta_1-\delta_2)] \\ \cos(2k_3\Delta_{rz_0}) & \cos[2k_3(\Delta_{rz_0}-\delta_1)] & \cos[2k_3(\Delta_{rz_0}-\delta_1-\delta_2)] \end{bmatrix}. \tag{4.13}$$

After expansion of the inverted matrix we obtain

$$r_{(1)} =$$

$$\frac{I(k_1)}{|P|}\Big\{\{\cos[2k_2(\Delta_{rz_0}-\delta_1)]\cos[2k_3(\Delta_{rz_0}-\delta_1-\delta_2)]\}$$

$$-\{\cos[2k_3(\Delta_{rz_0}-\delta_1)]\cos[2k_2(\Delta_{rz_0}-\delta_1-\delta_2)]\}\Big\}+ \tag{4.14}$$

$$\frac{I(k_2)}{|P|}\Big\{\{\cos[2k_3(\Delta_{rz_0}-\delta_1)]\cos[2k_1(\Delta_{rz_0}-\delta_1-\delta_2)]\}$$

$$-\{\cos[2k_1(\Delta_{rz_0}-\delta_1)]\cos[2k_3(\Delta_{rz_0}-\delta_1-\delta_2)]\}\Big\}+$$

$$\frac{I(k_3)}{|P|}\Big\{\{\cos\big[2k_1(\Delta_{rz_0}-\delta_1)\big]\cos\big[2k_2(\Delta_{rz_0}-\delta_1-\delta_2)\big]\}$$

$$-\{\cos\big[2k_2(\Delta_{rz_0}-\delta_1)\big]\cos\big[2k_1(\Delta_{rz_0}-\delta_1-\delta_2)\big]\}\Big\},$$

$r_{(2)} =$

$$\frac{I(k_1)}{|P|}\Big\{\{\cos\big(2k_2\Delta_{rz_0}\big)\cos\big[2k_3(\Delta_{rz_0}-\delta_1-\delta_2)\big]\}$$

$$-\{\cos\big(2k_3\Delta_{rz_0}\big)\cos\big[2k_2(\Delta_{rz_0}-\delta_1-\delta_2)\big]\}\Big\}$$

$$+\frac{I(k_2)}{|P|}\Big\{\{\cos\big(2k_1\Delta_{rz_0}\big)\cos\big[2k_3(\Delta_{rz_0}-\delta_1-\delta_2)\big]\}$$

$$-\{\cos\big(2k_3\Delta_{rz_0}\big)\cos\big[2k_1(\Delta_{rz_0}-\delta_1-\delta_2)\big]\}\Big\}$$

$$+\frac{I(k_3)}{|P|}\Big\{\{\cos\big(2k_2\Delta_{rz_0}\big)\cos\big[2k_1(\Delta_{rz_0}-\delta_1-\delta_2)\big]\}$$

$$-\{\cos\big(2k_1\Delta_{rz_0}\big)\cos\big[2k_2(\Delta_{rz_0}-\delta_1-\delta_2)\big]\}\Big\},$$

$r_{(3)} =$

$$\frac{I(k_1)}{|P|}\Big\{\{\cos\big(2k_2\Delta_{rz_0}\big)\cos\big[2k_3(\Delta_{rz_0}-\delta_1)\big]\}$$

$$-\{\cos\big(2k_3\Delta_{rz_0}\big)\cos\big[2k_2(\Delta_{rz_0}-\delta_1)\big]\}\Big\}$$

$$+\frac{I(k_2)}{|P|}\Big\{\{\cos\big(2k_3\Delta_{rz_0}\big)\cos\big[2k_1(\Delta_{rz_0}-\delta_1)\big]\}$$

$$-\{\cos\big(2k_1\Delta_{rz_0}\big)\cos\big[2k_3(\Delta_{rz_0}-\delta_1)\big]\}\Big\}$$

$$+\frac{I(k_3)}{|P|}\Big\{\{\cos\big(2k_1\Delta_{rz_0}\big)\cos\big[2k_2(\Delta_{rz_0}-\delta_1)\big]\}$$

$$-\{\cos\big(2k_2\Delta_{rz_0}\big)\cos\big[2k_1(\Delta_{rz_0}-\delta_1)\big]\}\Big\},$$

where the determinant $|P|$ is

$$
\begin{aligned}
|P| = \; & \cos(2k_1\Delta_{rz_0})\left\{\{\cos[2k_2(\Delta_{rz_0}-\delta_1)]\cos[2k_3(\Delta_{rz_0}-\delta_1-\delta_2)]\}\right. \\
& \left. -\{\cos[2k_2(\Delta_{rz_0}-\delta_1-\delta_2)]\cos[2k_3(\Delta_{rz_0}-\delta_1)]\}\right\} \\
& +\cos[2k_1(\Delta_{rz_0}-\delta_1)]\left\{\{\cos[2k_2(\Delta_{rz_0}-\delta_1-\delta_2)]\cos(2k_3\Delta_{rz_0})\}\right. \\
& \left. -\{\cos(2k_2\Delta_{rz_0})\cos[2k_3(\Delta_{rz_0}-\delta_1-\delta_2)]\}\right\} \\
& +\cos[2k_1(\Delta_{rz_0}-\delta_1-\delta_2)]\left\{\{\cos(2k_2\Delta_{rz_0})\cos[2k_3(\Delta_{rz_0}-\delta_1)]\}\right. \\
& \left. -\{\cos[2k_2(\Delta_{rz_0}-\delta_1)]\cos(2k_3\Delta_{rz_0})\}\right\}.
\end{aligned}
\tag{4.15}
$$

Once the Fresnel coefficients are found, the refractive indices may then be calculated directly, assuming the front medium index n_0 is known. Using Eq(4.9), n_1 can be calculated from r_1; n_2 can then be calculated from r_2, and the last medium then from r_3 using:

$$
\begin{aligned}
n_1 &= -n_0\frac{r_{(1)}-1}{r_{(1)}+1}, \\
n_2 &= -n_0\frac{r_{(1)}+r_{(2)}-r_{(1)}r_{(2)}-1}{r_{(1)}r_{(2)}+r_{(1)}+r_{(2)}+1}, \\
n_3 &= -n_0\frac{r_{(1)}+r_{(2)}+r_{(3)}-r_{(1)}r_{(2)}-r_{(1)}r_{(3)}-r_{(2)}r_{(3)}+r_{(1)}r_{(2)}r_{(3)}-1}{r_{(1)}r_{(2)}+r_{(1)}r_{(3)}+r_{(2)}r_{(3)}+r_{(1)}+r_{(2)}+r_{(3)}+r_{(1)}r_{(2)}r_{(3)}+1}.
\end{aligned}
\tag{4.16}
$$

Not all sets of 3 points on the spectral response can be used to solve Eq(4.12) since for some sets, the determinant of the matrix $\boldsymbol{P}$ is zero and hence the equation is unsolvable. This occurs when the chosen wavenumber components do not provide linearly independent equations. The wavenumber components in which the determinant is zero are obtained in the next section.

4.2.2. Roots of the Determinant

The matrix equation is solvable for those spectral components for which the matrix determinant is not zero. The full derivation of the roots is presented in the appendix (section 0). The final results are presented and discussed here. For non-zero mismatch arm lengths, the determinant for a two layer system is given by Eq(4.13). The determinant is zero whenever two rows or columns are equal or linearly depend on each other or when one or more row or column is zero. By manipulating the determinant's columns we can find the conditions that make the determinant zero. In summary, there are nine sets of wavenumber conditions, each of which specify a subset of wavenumbers k_1, k_2, k_3 that depend on the choice of integers m, m', m'', respectively. The choice of integer is constrained by the bandwidth of the probe beam. These condition sets are listed in

Table 4.1.

Table 4.1: Condition sets for the determinant's roots for non-zero arm mismatch case

Solution sets	Matrix compo-	k_1	k_2	k_3

	nents			
1.	Column1 $\equiv 0$	$\frac{(2m+1)\pi}{4\Delta_{rz_0}}$	$k_1 + \frac{m'\pi}{2\Delta_{rz_0}}$	$k_1 + \frac{m''\pi}{2\Delta_{rz_0}}$
2.	Column2 $\equiv 0$	$\frac{(2m+1)\pi}{4(\Delta_{rz_0} - \delta_1)}$	$k_1 + \frac{m'\pi}{2(\Delta_{rz_0} - \delta_1)}$	$k_1 + \frac{m''\pi}{2(\Delta_{rz_0} - \delta_1)}$
3.	Column3 $\equiv 0$	$\frac{(2m+1)\pi}{4(\Delta_{rz_0} - \delta_1 - \delta_2)}$	$k_1 + \frac{m'\pi}{2(\Delta_{rz_0} - \delta_1 - \delta_2)}$	$k_1 + \frac{m''\pi}{2(\Delta_{rz_0} - \delta_1 - \delta_2)}$
4.	Column 1 $\equiv$ column2 $(-\text{sign})$	$\frac{m\pi}{2\Delta_{rz_0} - \delta_1}$	$k_1 + \frac{m'\pi}{2\Delta_{rz_0} - \delta_1}$	$k_1 + \frac{m''\pi}{2\Delta_{rz_0} - \delta_1}$
5.	Column 1 $\equiv$ column3 $(-\text{sign})$	$\frac{m\pi}{2\Delta_{rz_0} - \delta_1 - \delta_2}$	$k_1 + \frac{m'\pi}{2\Delta_{rz_0} - \delta_1 - \delta_2}$	$k_1 + \frac{m''\pi}{2\Delta_{rz_0} - \delta_1 - \delta_2}$
6.	Column 2 $\equiv$ column3 $(-\text{sign})$	$\frac{m\pi}{2\Delta_{rz_0} - 2\delta_1 - \delta_2}$	$k_1 + \frac{m'\pi}{2\Delta_{rz_0} - 2\delta_1 - \delta_2}$	$k_1 + \frac{m''\pi}{2\Delta_{rz_0} - 2\delta_1 - \delta_2}$
7.	Column 1 $\equiv$ column2 $(+\text{sign})$	$\frac{m\pi}{\delta_1}$	$k_1 + \frac{m'\pi}{\delta_1}$	$k_1 + \frac{m''\pi}{\delta_1}$

8.	Column 1 ≡ column3 (+sign)	$\frac{m\pi}{\delta_1+\delta_2}$	$k_1+\frac{m'\pi}{\delta_1+\delta_2}$	$k_1+\frac{m''\pi}{\delta_1+\delta_2}$
9.	Column 2 ≡ column3 (+sign)	$\frac{m\pi}{\delta_2}$	$k_1+\frac{m'\pi}{\delta_2}$	$k_1+\frac{m''\pi}{\delta_2}$

For the zero mismatch case ($\Delta_{rz_0}=0$), the determinant simplifies to

$$|P|=\begin{vmatrix}1 & \cos 2k_1(\delta_1) & \cos 2k_1(\delta_1+\delta_2)\\ 1 & \cos 2k_2(\delta_1) & \cos 2k_2(\delta_1+\delta_2)\\ 1 & \cos 2k_3(\delta_1) & \cos 2k_3(\delta_1+\delta_2)\end{vmatrix}. \tag{4.17}$$

There are now four conditions that yield zero for the determinant which are shown in Table 4.2;

Table 4.2: Condition sets for the determinant's roots for zero mismatch case

Solution sets	k_1	k_2	k_3
1.	any value	$k_1+\frac{m'\pi}{2\delta_1}$	$k_1+\frac{m''\pi}{2\delta_1}$
2.	any value	$k_1+\frac{m'\pi}{2(\delta_1+\delta_2)}$	$k_1+\frac{m''\pi}{2(\delta_1+\delta_2)}$
3.	$\frac{m\pi}{\delta_2}$	$k_1+\frac{m'\pi}{\delta_2}$	$k_1+\frac{m''\pi}{\delta_2}$
4.	$\frac{m\pi}{2\delta_1+\delta_2}$	$k_1+\frac{m'\pi}{2\delta_1+\delta_2}$	$k_1+\frac{m''\pi}{2\delta_1+\delta_2}$

4.2.3. The Physical Interpretation of the Determinant Roots

The physical interpretation of the determinant roots can be understood by comparing

Table 4.1 and Eq(4.8). Condition set 1 corresponds to frequencies that make the first term on the right hand side of Eq(4.8) to be zero. In this situation there would be no contribution from the first interface to the spectral response and thus no information would available from the first interface at those particular frequencies. Similarly, condition set2 and set3 result in no information provided from the second and the third interfaces respectively.

Condition set4 and set7 correspond to the cases where the phases of the fields reflected from the first and second interfaces are exactly the same at the detector plane. In this case the two fields overlap each other and are not distinguishable. This can be seen in Eq(4.8) when the first two terms cosine functions have the same value and makes it impossible to distinguish between the information from the first and second interfaces. Similarly, condition set5 and set8 correspond to the situations in which the phases of the reflected fields from the first and third interfaces are the same and condition set6 and set9 for the second and third interfaces.

4.3. The General Matrix Formulation

The introduced method for measuring simultaneous index/thickness from spectral components can be generalized to any multi-layer systems. An N-layer system has $N+1$ interfaces, therefore we need $N+1$ spectral components to calculate $N+1$

Fresnel coefficients. In general the matrix for finding the Fresnel coefficients for an N-layers system can be written as

$$\begin{bmatrix} r_{(1)} \\ r_{(2)} \\ \vdots \\ r_{(N+1)} \end{bmatrix} = \boldsymbol{P}^{-1} \begin{bmatrix} I(k_1) \\ I(k_2) \\ \vdots \\ I(k_{N+1}) \end{bmatrix}, \tag{4.18}$$

where the matrix $\boldsymbol{P}$ is

$$\begin{bmatrix} \cos(2k_1\Delta_{rz_0}) & \cos[2k_1(\Delta_{rz_0}-\delta_1)] & \cdots & \cos\left[2k_1\left(\Delta_{rz_0}-\sum_{i=1}^{N}\delta_i\right)\right] \\ \cos(2k_2\Delta_{rz_0}) & \cos[2k_2(\Delta_{rz_0}-\delta_1)] & \cdots & \cos\left[2k_2\left(\Delta_{rz_0}-\sum_{i=1}^{N}\delta_i\right)\right] \\ \vdots & \vdots & \ddots & \vdots \\ \cos(2k_{N+1}\Delta_{rz_0}) & \cos[2k_{N+1}(\Delta_{rz_0}-\delta_1)] & \dots & \cos\left[2k_{N+1}\left(\Delta_{rz_0}-\sum_{i=1}^{N}\delta_i\right)\right] \end{bmatrix}. \tag{4.19}$$

The system can then be solved using *N+1* wavenumbers in the spectrum that do not yield a zero determinant.

4.4. Limitations Imposed by the Working Model

The introduced method in section 4.2.1 for measuring the index and thickness was based on the summation method which ignores multiple reflections. This imposes some limitations on the applicability of the method. In this section the theoretical and experimental limitations of this method are explained.

4.4.1. The Summation Method- Mathematical Limitations

In order to find the limitations of the proposed method, we first review its theoretical basis. In the proposed method the signal from the object is modeled using the summation method. This is a simplified signal in which multiple reflections between interfaces are neglected. To understand the limitation of the

summation method, we compare this signal to the one calculated by TMM, a is the more realistic representation of the real OCT signal. Working with a two layer system with optical thicknesses δ_1 and δ_2 and Fresnel coefficients r_1, r_2 and r_3, the reflected electric fields for each model are

$$U^{sum} = r_1 + r_2 e^{-i2k\delta_1} + r_3 e^{-i2k(\delta_1+\delta_2)},$$

$$U^{TMM} = \frac{r_1 + r_2 e^{-i2k\delta_1} + r_3 e^{-i2k(\delta_1+\delta_2)} + r_1 r_2 r_3 e^{-i2k\delta_2}}{r_1 r_2 e^{-i2k\delta_1} + r_2 r_3 e^{-i2k\delta_2} + r_1 r_2 e^{-i2k(\delta_1+\delta_2)} + 1}. \quad (4.20)$$

It is seen that the summation method is a first order approximation of TMM in which multiple reflections are neglected. Only the TMM terms to first order in *r* are kept, and $r_i r_j \ll 1$ then becomes the system constraint. The limits of this approximation will be explored in sections 6.1.1 and 7.4.3.

4.4.2. The Multiple Scattering Regime- Experimental Limitations

The analysis of the scattered light and its application in FD-OCT presented in previous sections was based on single scattering scheme. In this scheme, for an inhomogeneous medium, it is assumed that the number of scattering sites is sufficiently small and their separation sufficiently large so that the scattered wavelets by each particle is not affected by the neighbor sites. Multiple scattering regime is out of the scope of this thesis and here only a quick note on dealing with highly scattering media is given.

For highly scattering medium like many tissues, multiple scattering occurs especially for high penetration depths. The primary effect of the multiple scattering is a degraded spatial coherence of the resultant scattered field which in turns

reduces the image contrast and lateral resolution of the imaging system [119]. For highly scattering mediums or mediums that exhibit random variation in refractive index distribution, the approach to solve the scattered field is the extended Huygens-Fresnel principle. This approach was developed by Lutomirski and Yura and states that the Huygens- Fresnel principle can be extended to a medium that exhibits a spatial variation (but not temporal) in the index of refraction (weakly inhomogeneous random medium) [120]. This approach was adapted for the analysis of OCT images of tissue [17], [119], [121], [122]. Thrane in 2000 [122] showed that the lateral coherence length of the OCT signal, depends on the distance between the sample surface and the observation plane. The lateral coherence length is larger for larger distances due to the fact that the distorted spherical wavelets at large distance will approximately become plane waves. This is called "shower curtain effect" and was added to the OCT analysis by Thrane.

Chapter 5. Designing the Simulation Study and Link to Experimental Implementation

The solution describe above is investigated using simulations and the results of these investigations are presented in the next two chapters of this thesis. The study design is simple; a simulation system (comprising sample and OCT) is used to generate a realistic FD-OCT output. The new methodology described in Chapter 4 is then used to extract the wanted outputs using only the FD-OCT optical paths as input to the solution. Extracted outputs are then compared to model parameters to quantify the accuracy of the new methodology. In this Chapter we describe in detail the simulation system used for these investigations.

5.1. The Sample: the Planar Multilayer

We start with a planar multilayer system with a non-absorbing, isotropic and homogeneous index of refraction for each layer. We also assume that the boundaries of this system are solid and ideally flat (i.e. the surface roughness is much less than the incident wavelength). The model is schematically shown in Figure 5.1 for a simple two layer system

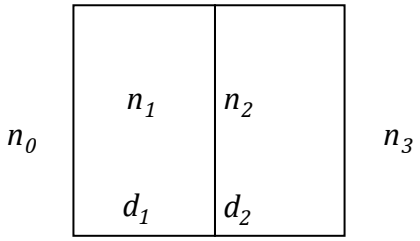

Figure 5.1: Schematic representation of a two layer system

5.2. Simulating the FD-OCT Optical Source and Detection System

The light source and detection system specifications used in all simulations, unless otherwise stated, are listed in Table 5.1. The light source spectrum, *s(k)*, is modeled as a Gaussian-shaped amplitude spectrum defined as per previous studies, for example [117]

$$s(k) = \frac{1}{\sqrt{\Delta k \sqrt{\pi}}} e^{-\frac{1}{2}\left[\frac{k-k0}{\Delta k}\right]^2}, \tag{5.1}$$

where $k0$ is the central wave number corresponding to the central wavelength (k0$= 2\pi/\lambda 0$) and Δk represents the spectral bandwidth. The source power spectral density is defined as $S(k) = |s(k)|^2$.

Using a spectrometer as the detection system, the simulation model is as a typical market-available system like the COBRA OCT spectrometer (C-650-950 (UHR)), with $N = 4096$ pixels, a wavelength range of 650-950 nm, and a Spectral Resolution of 0.075 nm. The specifications of the designed simulation system in this thesis are summarized in Table 5.1.

Table 5.1: The light source and detection system specifications

Parameter	Symbol	Relation to other parameters	The value
The Light Source			
Central wavelength	$\lambda 0$		800 nm
Central wavenumber	$k0$	$\frac{2\pi}{\lambda 0}$	7.85×10^6 m^{-1}
The source bandwidth	$\Delta\lambda_{FWHM}$		50 nm
The source bandwidth	Δk_{FWHM}	$\frac{\pi}{\sqrt{\ln(2)}}\frac{\Delta\lambda_{FWHM}}{\lambda 0^2}$	2.948 $\times 10^5$m^{-1}
The coherence length (round trip)		$\frac{2\,ln(2)}{\pi}\frac{\lambda 0^2}{\Delta\lambda}$	5.6 μm
The Detection System			
Number of data points	N		4096
The Spectrometer bandwidth	$\Lambda\lambda$		311 nm
The Spectrometer bandwidth	Λk	$k_{N-1} - k_0$	2.95×10^6m^{-1}
The Spectrometer resolution	$\delta\lambda$	$\frac{\Lambda\lambda}{N-1}$	0.075 nm
The Spectrometer resolution	δk	$\frac{\Lambda \mathrm{k}}{N-1}$	7.2×10^2m^{-1}
sampling frequency		$\frac{1}{\delta k}$	1.4 mm
detectable range	z_{max}	$\frac{\pi}{2\delta k}$	2.18 mm
Fourier transformed bin spacing (imaging resolution)	δz	$\frac{\pi}{N\delta k}$	1.06 μm

5.3. Simulating the FD-OCT Signal for Analysis: the TMM Approach

The reflected spectrum from the multi layer object is calculated using the Transfer Matrix Method (TMM). TMM is a standard tool to calculate the total electric field reflected and transmitted through multilayer systems like those described above [123].The method that is introduced here is based on Abeles's matrix method [123].

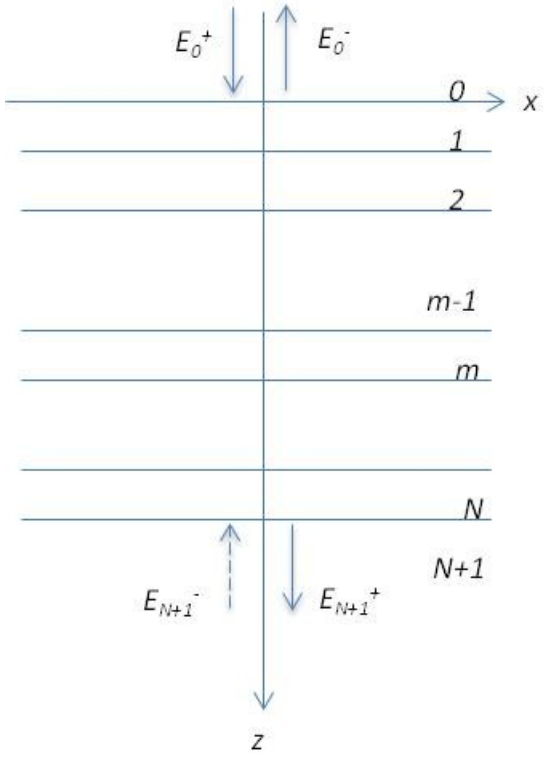

Figure 5.2: Stratified multilayered system sandwiched between media (0) and (N+1)

Considering a stratified multilayered system (Figure 5.2), for each interface separating two media, the relation between the electric fields on both sides is given by

$$\begin{pmatrix} E_{m-1}^{+} \\ E_{m-1}^{-} \end{pmatrix} = Q_{m-1,m} \begin{pmatrix} E_{m}^{+} \\ E_{m}^{-} \end{pmatrix}, \tag{5.2}$$

where

$$Q_{m-1,m} = \frac{1}{t_{m-1,m}} \begin{bmatrix} 1 & \mathrm{r}_{m-1,m} \\ \mathrm{r}_{m-1,m} & 1 \end{bmatrix}, \tag{5.3}$$

with $\mathrm{r}_{m-1,m}$ and $t_{m-1,m}$ the Fresnel coefficients for reflection and transmission, respectively. For normally incidence field, the Fresnel coefficients for reflection and transmission respectively are

$$\mathrm{r}_{m-1,m} = \frac{n_{m-1} - n_m}{n_{m-1} + n_m}, \tag{5.4}$$

and

$$t_{m-1,m} = \frac{2n_{m-1}}{n_{m-1} + n_m}. \tag{5.5}$$

Propagation of light through the m^{th} slab of material with index n_m and thickness d_m is accounted for by a phase matrix, P_m,

$$P_m = \begin{pmatrix} e^{i\delta_m} & 0 \\ 0 & e^{-i\delta_m} \end{pmatrix} \quad , \quad \delta_m = \frac{2\pi n_m d_m}{\lambda}, \tag{5.6}$$

where λ is the wavelength of light in vacuum. We may set $\delta_0 = 0$ [123] and the system transfer matrix, T, can be obtained by successive multiplication of $Q_{m-1,m}P_mQ_{m,m+1}$ which can be written for N layer system as

$$T = \begin{bmatrix} T_{11} & T_{12} \\ T_{21} & T_{22} \end{bmatrix} = Q_{01} \prod_{m=1}^{N} P_m Q_{m,m+1}. \tag{5.7}$$

Abeles showed that the relation among the amplitudes of the electric fields of incident wave E_0^+, reflected wave E_0^-, and transmitted wave after N layers E_{N+1}^+ is expressed by a matrix equation for stratified films with N layers

$$\begin{pmatrix} E_0^+ \\ E_0^- \end{pmatrix} = \begin{pmatrix} T_{11} & T_{12} \\ T_{21} & T_{22} \end{pmatrix} \begin{pmatrix} E_{N+1}^+ \\ E_{N+1}^- \end{pmatrix}. \tag{5.8}$$

For a semi-infinite substrate medium we can set $E_{N+1}^- = 0$. Abeles obtained a convenient formula for the system reflection and transmission coefficients, *r* and *t*, respectively:

$$r = \frac{E_0^-}{E_0^+} = \frac{T_{21}}{T_{11}}, \tag{5.9}$$

and

$$t = \frac{E_{N+1}^+}{E_0^+} = \frac{1}{T_{11}}. \tag{5.10}$$

In general, r and t are complex functions and contain information about the amplitude and phase of the reflected and transmitted light even when the refractive index is purely real. The transfer matrix method is an exact analytic description of the system optical response, since it has the ability to account for multiple reflections inside the stratified media. TMM is used in this thesis to provide a signal based on known parameters so that the viability of your new OCT analysis methodology, based on the simpler summation method, can be assessed.

5.4. Optimizing Source and Detection to the Sample

5.4.1. Axial Resolution

In an OCT system, the theoretical axial resolution is limited by the coherence length of the source (given in Table 5.1)[117]. Good depth image resolution can be achieved by using a light source with a wide spectral range (i.e., a short coherence length).

From the expression for the coherence length it can be seen that for the longer source central wavelengths (λ_0), a wider bandwidth ($\Delta\lambda$) is needed to achieve the same spatial resolution [124]. In order to resolve two reflector sites separated by distance l_c , pixel spacing in the spatial domain of $\delta z \leq l_c/2$ is needed according to the Rayleigh criterion [125].

5.4.2. Imaging Depth

The imaging depth of any OCT system is constrained by the properties of the object and the detection system [126]. The former affects the available signal strength since with increased depth into the object, the scattering of light will be higher. This will be discussed in the following section. Here we consider the fundamental relationship imposed by the detection system.

The sampling resolution of the spectral data is related to the optical path difference resolution δz, since the wavenumber (k) and the position (z) are a Fourier transform pair. According to the Nyquist–Shannon sampling theorem, for the highest frequency of the spectral signal, we must have $1/\delta k = 2 \times (2\mathcal{Z}_{max}/2\pi)$. The unambiguous maximum detectable range (the scan depth) is [62] [117]

$$\pm\mathcal{Z}_{max} = \pm\frac{\pi}{2\delta k}. \tag{5.11}$$

If the spectral bandwidth of the spectrometer is represented by Λk (in wavelength by $\Lambda\lambda$) and the number of spectrometer pixels is N, then the expression for the maximum detectable range can also be written as [9], [60], [127]

$$\mathcal{Z}_{max} = \frac{\pi N}{2\Lambda k} = \frac{{\lambda_0}^2}{4\delta\lambda}. \tag{5.12}$$

Any larger $\mathcal{Z}$ value exceeds the Nyquist limit and creates an under-sampling artifact aliased down to depths less than $\mathcal{Z}_{max}$ [61], [128] . The spectrometer resolution (the sampling resolution) is seen to be the key parameter to determine the scan depth from Eq(5.12). The sampling resolution can be increased either by decreasing the bandwidth of the spectrometer or increasing the number of pixels. The first option would result in a loss of axial resolution. In our simulation model system given in Table 5.1, if the number of sampling points were doubled for instance, the scan depth increase from 2.2 mm to 4.4 mm. For the fixed number of spectrometer pixels therefore, there are trade offs between axial resolution and the axial range [129]. In the z-domain, since the number of available data points is $N/2$, the channel spacing (imaging resolution) is [62]

$$\delta\mathcal{Z} = \frac{\mathcal{Z}_{max}}{N/2} = \frac{\pi}{\Lambda k} = \frac{{\lambda_0}^2}{2\Lambda\lambda}. \tag{5.13}$$

The spectrometer bandwidth is the key parameter to determine the axial pixel spacing. It can be seen from Eq(5.13) that for a higher source central wavelength, higher spectrometer bandwidth must be used to achieve the same imaging resolution. This in turn affects the maximum detectable range. If $\Lambda\lambda$ is too small, the available spectrum is not fully captured by the spectrometer and the axial pixel spacing will not support the theoretical axial resolution. On the other hand, if $\Lambda\lambda$ is too large, the pixel spacing and the axial measurement range are reduced without improving the axial resolution. Therefore, $\Lambda\lambda$ must be chosen so that the optimal

resolution given by the coherence length is achieved without reducing the axial measurement range [125]. The required spectrometer bandwidth can be obtain by setting $\delta\mathcal{Z}$ smaller than half the targeted theoretical axial resolution as[125], [130]

$$\Lambda\lambda \geq \frac{\pi}{2ln2}\Delta\lambda_{FWHM} = 2.26618\,\Delta\lambda_{FWHM}. \tag{5.14}$$

The comparison between the source and the spectrometer bandwidth used in the simulation is shown in Figure 5.3 where $\Delta\lambda_{FWHM} = 6.2245$ .The spectrometer bandwidth is wider than the source bandwidth as required by (5.14) but is not too wide to produce unrealistic, shallow scan depth. In summary, in order to achieve simultaneously good depth resolution and extended depth range, it is necessary to select a light source with wide spectral range (or short coherence length) and employ a spectrometer with fine frequency resolution (large number of sampling points, N). [131]

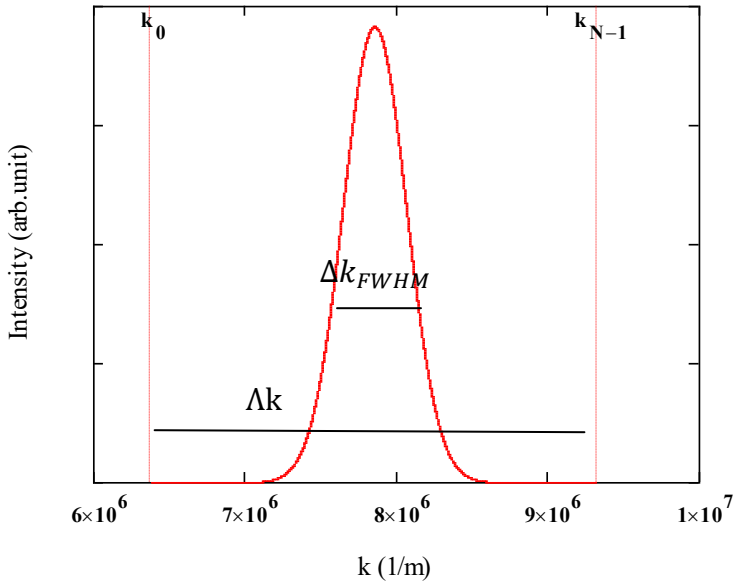

Figure 5.3: The comparison between the source bandwidth and the spectrometer bandwidth

5.4.3. Signal Detection

The issues related to the signal detection are only of concern for translating the theory into practice. This thesis a simulation study and a validation assessment of a novel methodology for FD-OCT image analysis and data extraction. Therefore in this section only a quick discussion of signal detection limitations is presented. A detailed discussion is out of the scope of this thesis and can be found in [61]–[63].

The important features of every OCT detection system, that characterize the measurement performance, are the detector's dynamic range and signal-to-noise ratio, usually expressed in dB. The dynamic range (DR) and the maximum signal-to-noise ratio $[(SNR)_{max}]$ are related by $DR = 10\log[(SNR)_{max}]$ [132], [133]. The signal to noise ratio is defined as the ratio of the minimum to the maximum measurable power P, $(SNR)_{max} = P_{max}/P_{min}$. The SNR of one scattering layer is the ratio of the interference signal to the overall intensity. For one single photodiode of the spectrometer SNR is [134]

$$SNR = \frac{2\sqrt{N_{R1}N_{O1}}}{\sqrt{N_{R1} + N_{o1} + 2\sqrt{N_{R1}N_{O1}}}} \approx 2\sqrt{N_{O1}}, \qquad (5.15)$$

N_{O1} and N_{R1} are the number of photons from the object and the reference arm respectively. A SNR of 80 or above is generally accepted as a minimum required for imaging biological samples [135]. In an FD-OCT system, since the signal in dispersed over the detectors array with N_D number of detectors, SNR will be

$$SNR_{FDOCT} = \sqrt{N_D}.SNR = 2\sqrt{N_{O1}}\sqrt{N_D}. \qquad (5.16)$$

This shows that SNR can be increased by employing larger number of detectors $\sqrt{N_D}$ This advantage does not exist in TD-OCT since single element detector is used there. Spectral Domain and Swept Source OCT have equivalent SNR expressions [62].

5.5. Optical Thickness Determination: Initial Input Data

In this section the optical thickness measurement by the simulation system is going to be described. As discussed earlier in section 4.1, the FD-OCT signal is obtained from the interference between the reflected signal from the sample and the reference signal. The spectral response signal, free from DC and AC terms is then Fourier transformed (using a Fast Fourier Transform) to generate the sample scattering function. The optical thicknesses are obtained from the separation between the peaks in the scatter function. The shape of each peak is characterized by the source coherence function, which widens that peak. The peak's approximate location is found using Mathcad's "localmax" function, the highest intensity point in a local area. A threshold value has been defined so only real peaks are identified. This value is approximate because of the limitations of discrete Fourier transforms (frequency leakage) and the limited coherence length of the light source.

Having found the peak neighborhoods, the sub-pixel position of each interface can be extracted by fitting the source coherence function to each detected peak. The program selects a region of data points in the neighborhood of each peak and fits the source coherence function (in this program, a Gaussian function) to these points. The apex positions of each Gaussian fitted curve are then used to calculate optical thicknesses. An example of this fit is shown in Figure 5.4

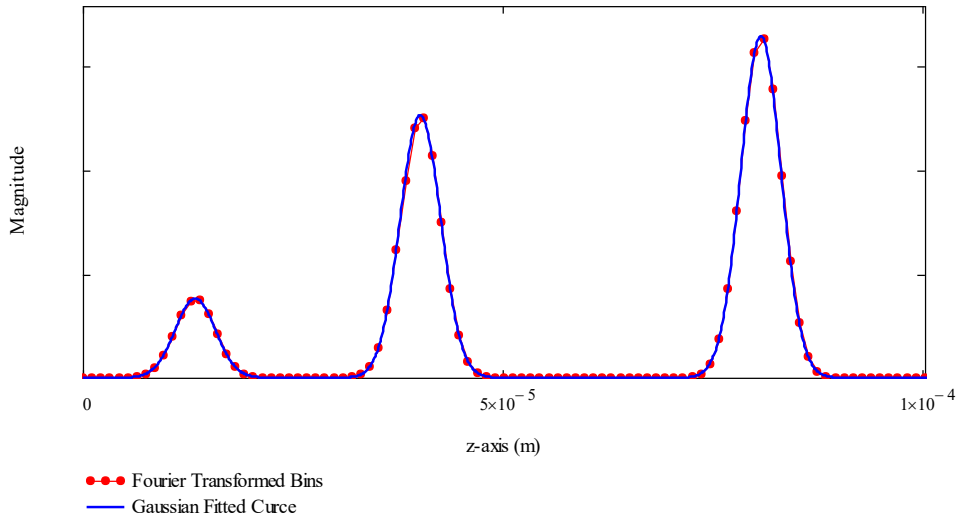

Figure 5.4: Gaussian function has been fitted to each peak in order to determine the peaks more accurately

A comparison between the optical thickness (OT) measurement from the peak of the Fourier transformed data and the peak of the Gaussian fitted curve is presented in Figure 5.5 for a one layer object. In this illustrating example the thickness of the slab is increased from 5 μm up to 15 μm with 0.1 μm increments. At small thicknesses the reported values is the same as the theoretical resolution of the simulation system given in Table 5.1, that is, the minimum detectable thickness. The measured values based on the Fourier data peaks (red color) give a step-like plot where the width of each step is around 1 μm, the size of the Fourier transformed bin spacing (δz) noted in Table 5.1. This shows that the measured values are the same for all optical thicknesses that fall within the range of one imaging cell. On the other hand, the fitted curve (blue color) results in a sub-pixel estimate for all thicknesses. The slope of the measured vs. the actual OT is 1.005982 which tells us that on average the OTs can be estimated within a few nanometers accuracy. However

excluding the unstable region will make a better precision within a fraction of one nanometer. For the curve fitted plot on Figure 5.5 , the region of OT less than 10 μm is wiggling abruptly. This region has been shown separately on Figure 5.6 and shows that the measurement error is stable for OT larger than ~13 μm.

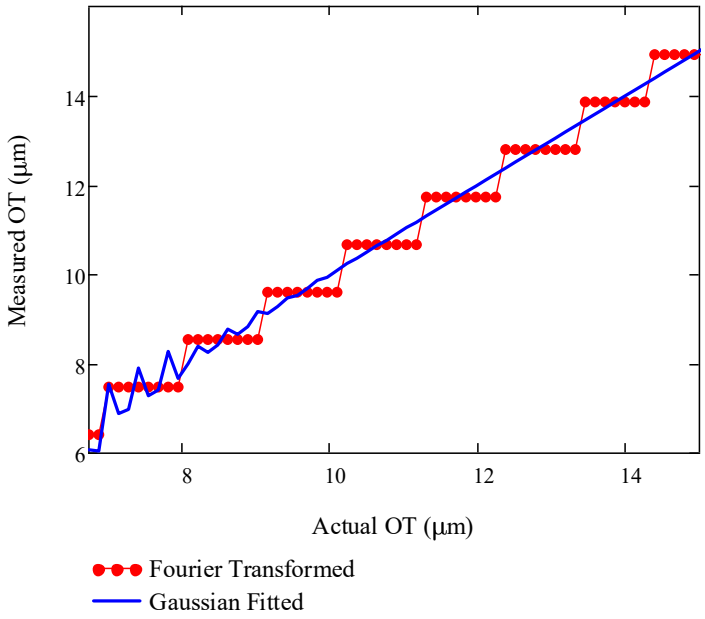

Figure 5.5: Measured versus actual OT of a one layer slab for a range of thickness. The plot shows the measured OT based on the peaks of the Fourier data (red color) and Gaussian fitted (blue color)

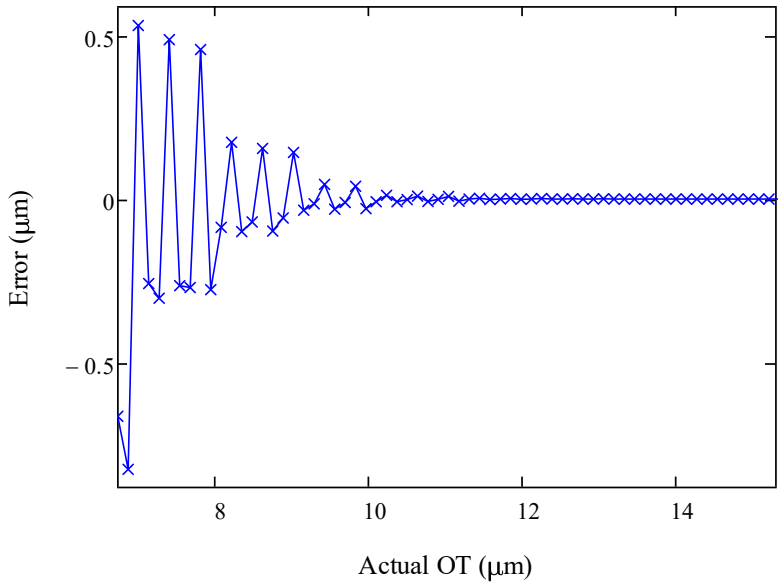

Figure 5.6: Error of measuring OT is shown to be less stable for OTs smaller than about 13 μm.

The instability in optical thickness measurement when the separation between two interfaces is less than about 13 μm can be explained as follow. It was explained earlier in this section that the program uses data points in the neighborhood of the peak to fits the source coherence function to these points. When two interfaces are too close to each other, there are fewer point around each peak that are unique to each peak so that the curve fitting cannot be performed accurately. This is illustrated in Figure 5.7 for a layer with 9 μm in optical thickness. It can be seen from Figure 5.7 that the blue curve is poorly fitted to the Fourier transformed bins and thus the apex positions cannot be determined accurately.

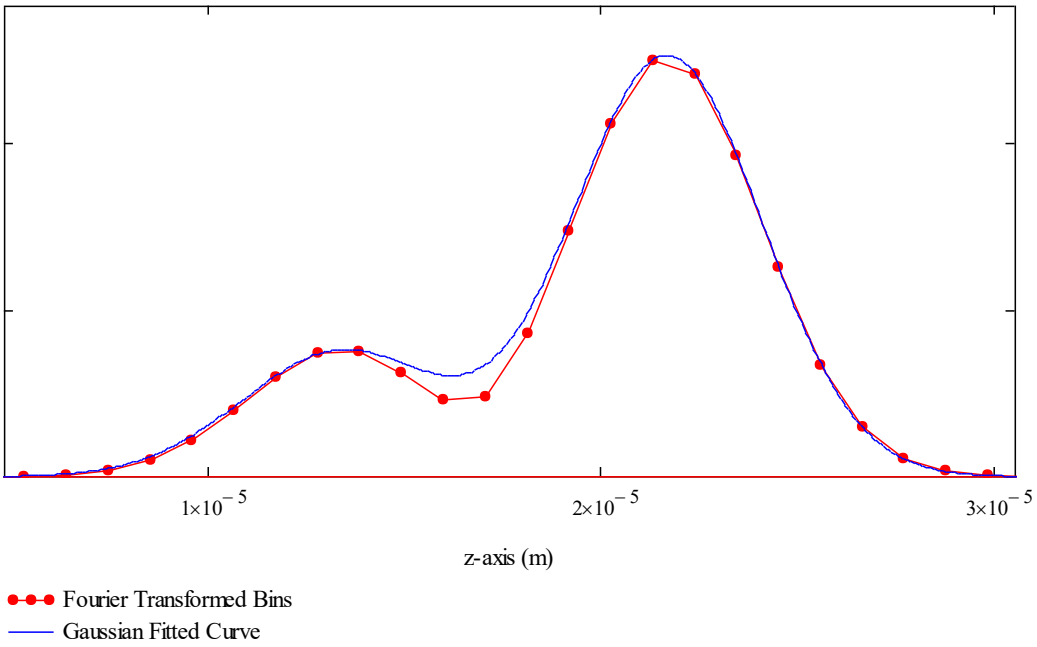

Figure 5.7: The fitted curve to the Fourier transformed bins corresponding to a layer with 9 μm in optical thickness.

5.5.1. Index Contrast

In this section the impact of index contrast between layers on optical thickness measurement is going to be described. It will be shown that strong scattering from one interface can overwhelm the weak scattering from the other and prevent us from finding the weakly scattering interface. The variation in the contrast that the system can tolerate will also be discussed. We use a single parameter assessment to provide an order-of-magnitude assessment of the difference in scattering strength that the system can tolerate.

As an illustrative example, we consider a two layer test model with the following specifications: $n_0 = 1.337, n_1 = 1.345, n_2 = 1.350, n_3 = 1.337$, $d_1 = 10$,and $d_2 = 30$ μm. The choice of thicknesses is not very important since we are looking at index contrast. We sweep one index at the time and keep all the other parameters

fixed and use the method described above to calculate the optical thicknesses. The test result is shown in Figure 5.8 where the measured optical thickness is plotted as a function of the swept index. It can be seen from the figure that for very high index contrast, the interfaces position cannot be determined correctly. When the contrast ratio between the layers is very large, the amplitude of the Fourier data corresponding to the high contrast layer is much larger than the amplitude of the other interfaces. It should be noted that minimum contrast of >0.0001 is required for the simulation system to detect an interface.

Figure 5.8 A, correspond to varying n_1, it is seen that for values higher than 1.905 the program does not find the last interface position correctly. In other words the amplitudes of the Fourier data corresponding to the first and the second interfaces are much higher than for the third interface so the latter is not seen and instead another side peak at distance equal to the first layer optical thickness is detected by the program. In this situation the program finds two layers with optical thicknesses the same as the first layer's optical thickness. The index contrast between the layers at the break point is $|n_1 - n_0| = 0.568$, $|n_1 - n_2| = 0.555$ and $|n_2 - n_3| = 0.013$ with the mean index contrast ratio of about 43. Figure 5.8 B corresponds to varying n_2 where for values higher than 1.941 the first interface cannot be seen and instead another side peak is chosen by the program. As the result the program finds two layers with optical thicknesses the same as the second layer's optical thickness. The index contrast between the layers at the break point is $|n_2 - n_1| = 0.596$ and $|n_2 - n_3| = 0.604$ where $|n_1 - n_0| = 0.008$. The mean index contrast ratio is about 75. Finally, Figure 5.8 C corresponds to varying n_3 where above 2.117, the middle

interface cannot be seen and the program finds two layers with optical thicknesses the same as the sum of the two layer's optical thicknesses. This happens when the index contrast between the layers is $|n_3 - n_2| = 0.767$ where $|n_2 - n_1| = 0.005$ and $|n_1 - n_0| = 0.008$. The mean index contrast ration in this case is about 118.

In summary the threshold value of the mean index contrast for varying n_1, n_2 and n_3 is 43, 75 and 118 respectively. The threshold contrast of the last interface is three times larger than that of the first interface and two times larger than that of the second interface. This shows that the simulation system for measuring the optical thicknesses is less sensitive to the contrast at the last interface than that of the other interfaces. In general this approach shows a high resilience to contrast ratio and should be applicable to a wide range of applications not just biological systems.

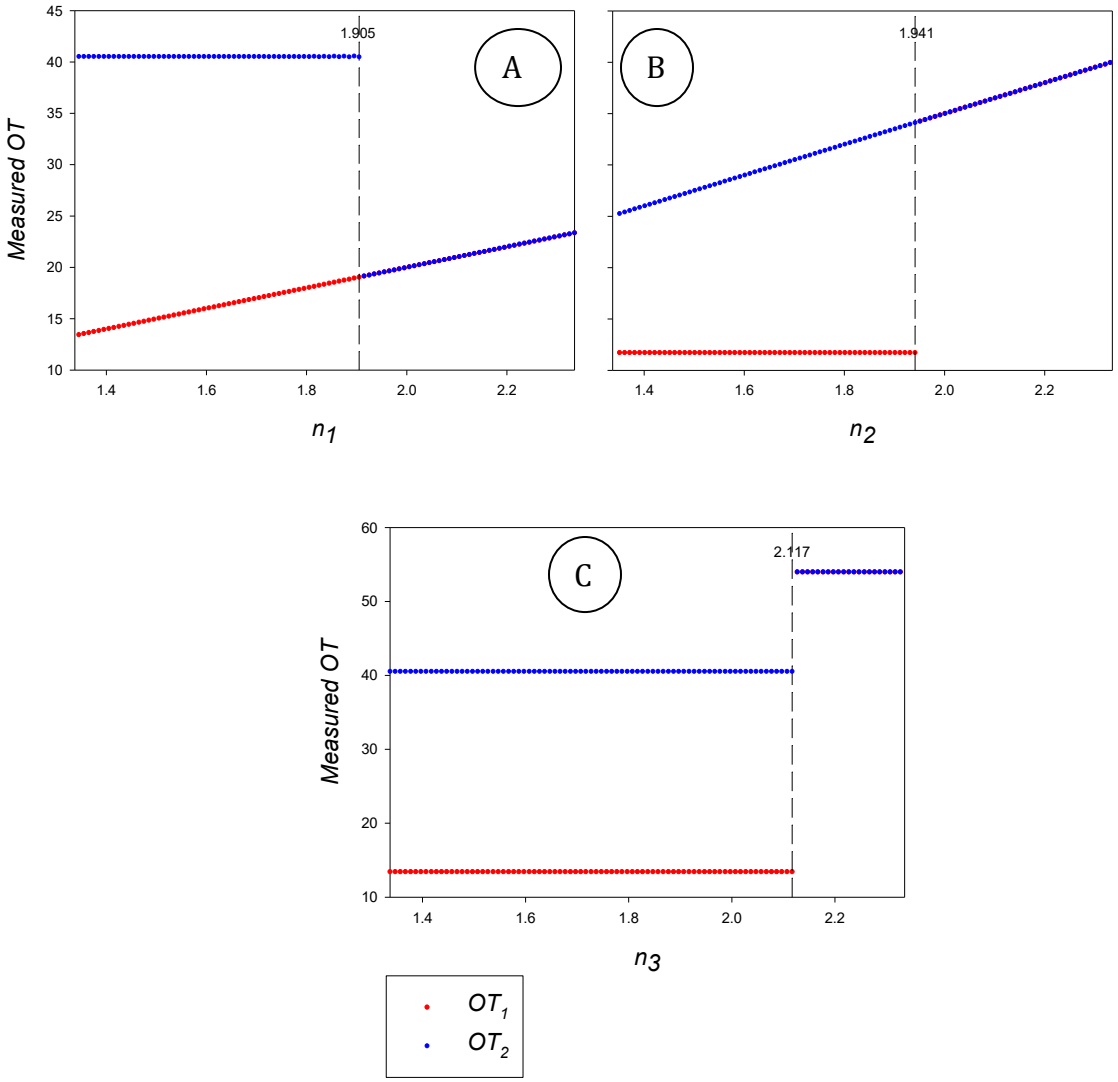

Figure 5.8: Optical thickness measurement of a two layer system with varying index contrast A) varying n_1 B) varying n_2 and C) varying n_3. The maximum index contrast is indicated on the graphs.

Chapter 6. Validation of the new methodology

In this chapter we test the applicability of the introduced index/thickness measurement method (section 4.2.1) for specific system realizations against digitally constructed TMM test data to determine if there is any systematic dependence of the "error" (difference between TMM parameters and extracted parameters) on sample index/thickness. For a two layer system, the parameters to be extracted are the index/thickness of each layer and the last medium index of refraction, i.e. n_1 , n_2, n_3, d_1, d_2 assuming that the front medium index of refraction is known. In section 6.1 the quality of the sample's extracted parameters is tested for a range of realistic two layer samples when the error in optical thickness measurement is assumed to be negligible ($\varepsilon = 0$) although the Gaussian fitting algorithm will result is a small (sub nm) error. The more realistic situation $\varepsilon \neq 0$ is discussed in section 6.2.

6.1. Perfect Optical Thickness Input Data- Two Layer System

In this section the quality of the sample's extracted parameters (n_1 , n_2, n_3, d_1, d_2) is tested for a range of realistic two layer systems when the error in optical thickness measurement is assumed to be negligible ($\varepsilon = 0$). The impact of the sample's index contrast is investigated in section 6.1.1 and the impact of the sample's thickness profile is investigated in section 6.1.2.

6.1.1. The impact of refractive index profile

As discussed previously in section 4.4.1, the main constraint on our index/thickness extraction is that the Fresnel coefficients be small, meaning that the indices

difference across an interface (index contrast) be small. As the contrast increases, multiple reflections are no longer negligible and hence the summation method is not sufficient to describe the reflected spectrum accurately. This induces error in sample's extracted parameters (index/thickness) using the matrix formulation Eq(4.12). It will be shown and investigated in this section that for higher contrast, larger error in extracting the sample's parameters is expected as predicted.

In this section we investigate the impact of the refractive index profile on the parameters extracted from two layer systems $(n_1, n_2, n_3, d_1, d_2)$ when $\varepsilon = 0$. Two illustrative models with fixed layer thicknesses and varying indices are tested. The first test model is optically thick (with respect to the source coherence length) with thicknesses $d_1 = 10$ μm, $d_2 = 30$ μm and the second model is optically very thick with thicknesses $d_1 = 500$ μm, $d_2 = 300$ μm. An example of optically thin sample (a fraction of a wavelength) will be given separately (in section 7.6) since it needs a different light source bandwidth (very shorter coherence length) and different spectrometer specifications. The refractive index range explored begins with the surrounding medium index of refraction, 1.337 for biological application as the index of aqueous medium. The upper ranges are limited by the simulation system and are given in section 5.5.1 as the point at which the system cannot determine the number of layers correctly.

The impact of the first layer index contrast on the accuracy of the extracted parameters is shown in Figure 6.1. The vertical axis in the figures corresponds to the error extracted parameters and the horizontal axis corresponds to n_1 which is varied between 1.337 and 1.9 in 0.005 increments, while the other indices are

constant at $n_2 = 1.351$ and $n_3 = 1.337$. The left panes show the error in the index of refraction calculations and the right panes show the error in the thickness calculations. The thick and very thick cases are shown on the top and bottom rows of the figure respectively.

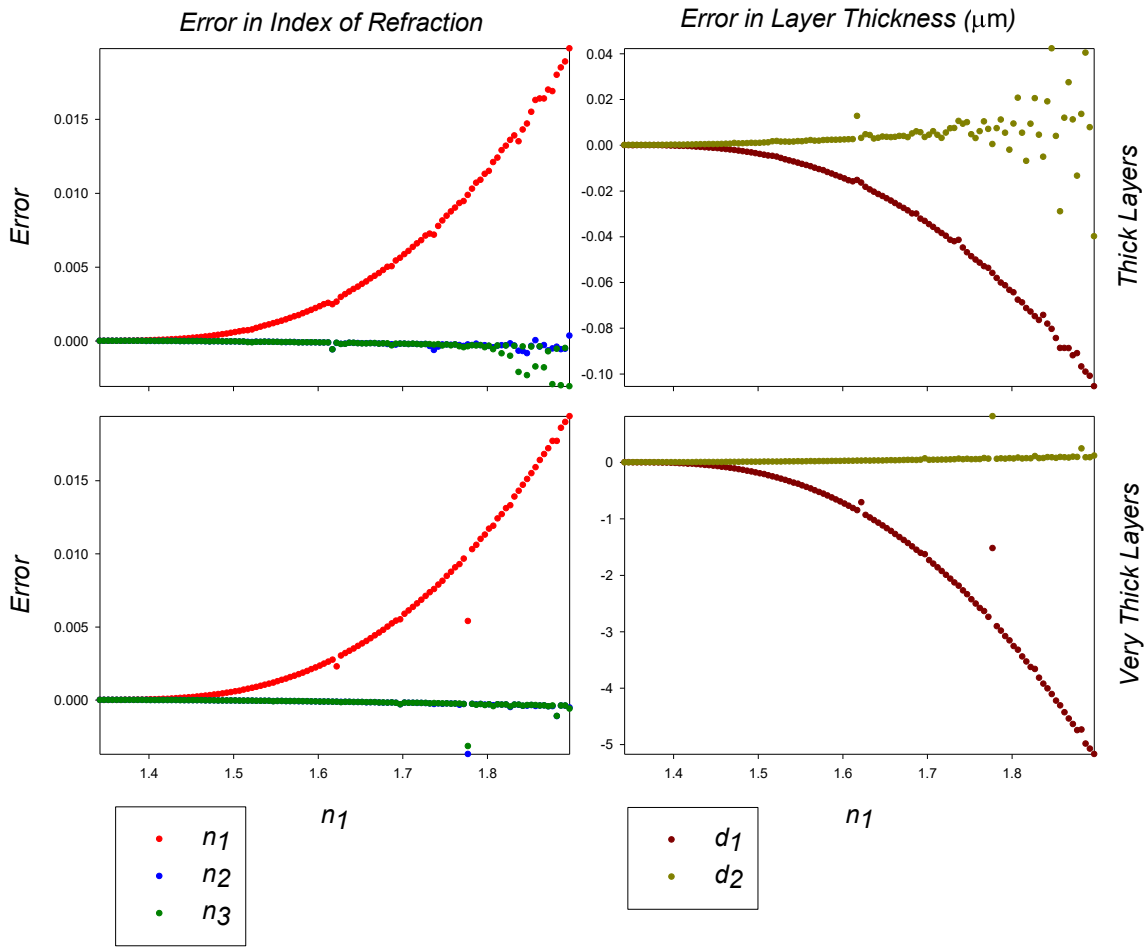

Figure 6.1: Impact of sample index contrast (varying n_1) on the accuracy of the sample's extracted parameters. On the left are shown the errors associated with the refractive indices and on the right are shown the errors associated with thicknesses. Both thick (top) and very thick (bottom) cases are shown. In this figure $n_2 = 1.351$ and $n_3 = 1.337$.

The first data point for both the thick and very thick cases on Figure 6.1 was out of the trend because the index of the first layer and the front medium were the same

and hence the simulation system could only detect the second layer. This point has been omitted from the figure. From the left pane of Figure 6.1 it can be seen that the error of n_1 increases with increasing n_1 due to the fact that multiple reflections are no longer negligible as predicted in section 4.4.1. It is also seen that as n_1 increases, the error for extracting n_1 grows more quickly than the error of extracting of the other indices. In other words the contrast at the interfaces for n_1 mostly affects the extraction of n_1. It can also be seen that the error of n_1 is the same for both the thick and very thick cases meaning that the thickness profile does not have much impact on the error in the extraction of indices. The difference in the error of n_1 between the thick and very thick cases is on average 1.56×10^{-5}. It can also be seen that the error of all indices show more stable behavior with very thick case compare to the thick case.

Since the thickness calculation is dependent on extracted index ($d_{1,2} = \delta_{1,2}/n_{1,2}$), the error of the extracted thicknesses has been determined from the quadrature uncertainty formula as

$$\Delta(d)/d \ = \pm\sqrt{(\Delta\delta/\delta\ )^2 + (\Delta n/n)^2}. \tag{6.1}$$

Therefore the relative error in thickness is directly proportional to the error of the measured optical thickness and the error of index. This can be seen from the right pane of Figure 6.1, where the relative errors in d_1 and d_2 depend on the errors in n_1 and n_2 respectively. The relative error of d_1 for both the thick and very thick case on average is 2.9×10^{-3} as expected since the error of n_1 is the same for both cases. The relative error of d_2 for both the thick and very thick case on average is 1.2×10^{-4}.

The impact of the second layer index contrast on the accuracy of the extracted parameters is shown in Figure 6.2. The vertical axis in this figure corresponds to the extracted parameter errors and the horizontal axis corresponds to n_2 which is scanned between 1.337 and 1.9 in 0.005 increments while the other indices are $n_1 = 1.345$ and $n_3 = 1.337$. On the left pane is shown the error of the index of refraction and on the right is shown the error in the thickness. The thick and very thick cases are shown on the top and bottom rows respectively.

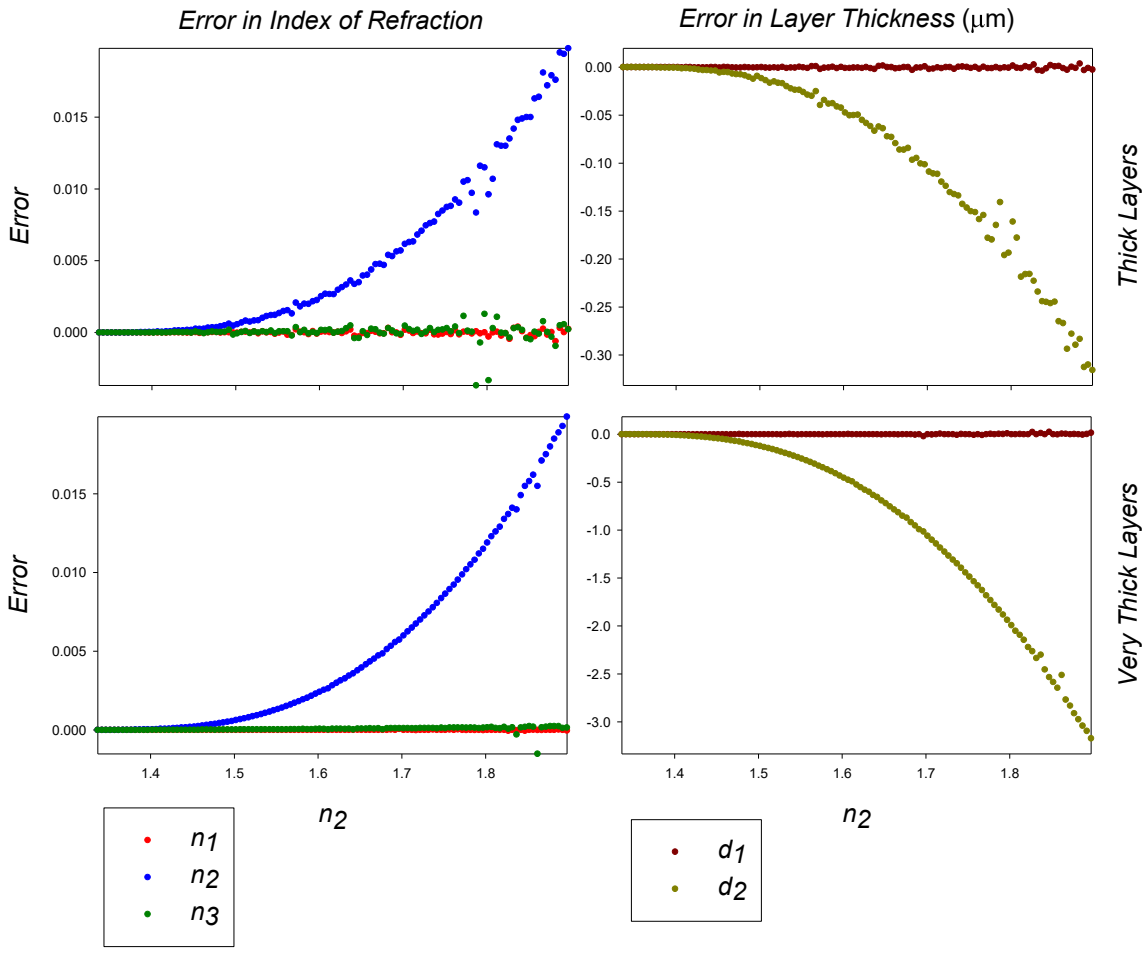

Figure 6.2: Impact of sample index contrast (varying n_2) on the accuracy of the sample's extracted parameters. On the left panes are shown the errors associated with the refractive indices and on the right are shown the errors associated with the thicknesses. Both a thick (top) and very thick (bottom) case are shown. In this figure $n_1 = 1.345$ and $n_3 = 1.337$.

From the left pane of Figure 6.2 it can be seen that the error of n_2 increases with increasing n_2 due to increasing the multiple reflections. It is also seen that as n_2 increases, the error of extracting n_2 grows more than the error of extracting of the other indices. In other words the contrast of n_2 mostly affects the extraction of n_2. Furthermore it can also be seen that the error in n_2 is the same for both the thick and very thick cases meaning that the thickness profile does not have much impact

on error of indices extraction. The difference in the error of n_2 between the thick and very thick cases is on average 3.68×10^{-5}. It can also be seen that the error of all indices show more stable behavior with very thick case compare to the thick case, the same we saw in Figure 6.1.

The relative error of the thickness, the right pane of Figure 6.2 is described by Eq(6.1) where the relative error of d_1 and d_2 depend on the error of n_1 and n_2 respectively. The relative error of $d_1$for the thick case is on average is 3.3×10^{-5} and for the very thick case is on average is 6.5×10^{-7} , which indicates that error in n_1 for the very thick case is on average less than the thick case. The relative error of d_2 for both the thick and very thick case on average is 2.9×10^{-3} which indicates that error of n_2 for both cases is on average the same.

The impact of the third layer index contrast on the accuracy of the extracted parameters is shown on Figure 6.3. The vertical axis in this figure corresponds to the extracted parameters error and the horizontal axis corresponds to n_3 which is scanned between 1.337 and 2.12 in 0.005 increments while the other indices are $n_1 = 1.345$ and $n_2 = 1.351$. On the left is shown the errors in the index of refraction and on the right the errors in thickness. The thick and very thick cases are shown on the top and bottom rows respectively.

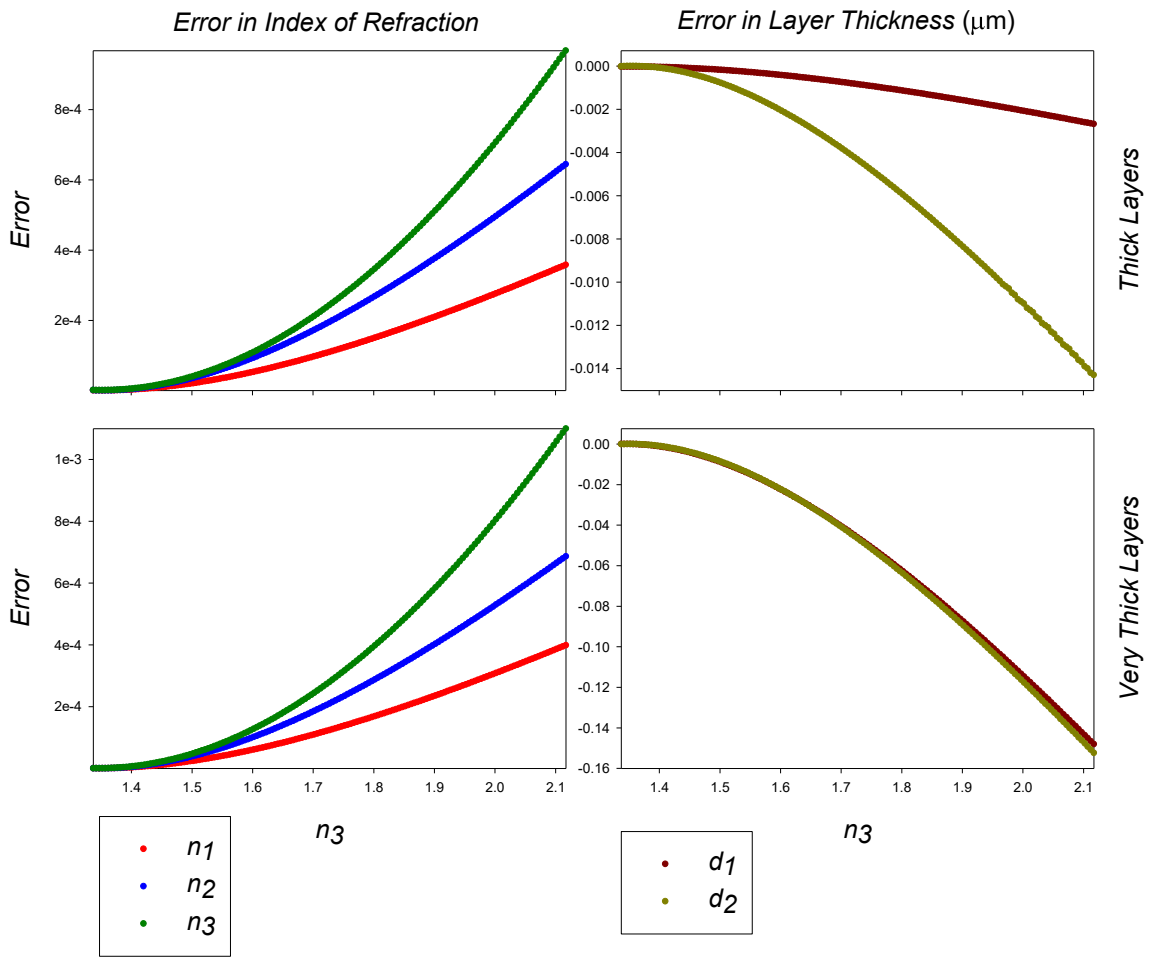

Figure 6.3: Impact of sample index contrast (varying n_3) on the accuracy of the sample's extracted parameters. On the left panes are shown the errors associated with the refractive indices and on the right are shown the errors associated with the thicknesses. Both a thick (top) and very thick (bottom) case are shown. In this figure $n_1 = 1.345$ and $n_2 = 1.351$.

From the left pane of Figure 6.3 it can be seen that the error of all indices increase with increasing n_3 due to the increase in the amplitude of the multiple reflections. It can also be seen that the error of n_1, n_2 and n_3 are the same for both the thick and very thick cases. The differences in errors in n_1, n_2 and n_3 between the thick and very thick cases are on average 1.6×10^{-5}, 1.6×10^{-5} and 4.6×10^{-5} respectively which shows that the errors in indices are almost independent of the thickness

profile. The relative error of thickness, the right pane of Figure 6.3 , is described by Eq(6.1) where the relative error of d_1 and d_2 depend on the error of n_1 and n_2 respectively. The relative error in d_1 for the thick case is on average 1.01×10^{-4} and for the very thick case 1.11×10^{-4}. The relative error in d_2 for the thick case is on average 1.75×10^{-4} and for very thick case 1.88×10^{-4} . These indicate that error of n_1 and n_2 for both cases are on average the same.

From the results illustrated in Figure 6.1, Figure 6.2 and Figure 6.3, we can have a rough estimate of the range of the parameters error with respect to each index value when other indices are constant. In order to have a better understanding the algorithm's behavior with respect to index contrast, a broader more complete set of models with varying n_1 and n_2 need to be explored. From Figure 6.3 it is seen that increasing n_3 does not have much impact on other parameters error. Therefore the parameters error distribution map is provided for a range of n_1 and n_2 from 1.337 to 1.9 in 0.011 increments while $n_3 = 1.337$ but must be estimated by the program. Both thicknesses are set to 30 μm. A total of 2600 test models were thus tested. In Figure 6.4 to Figure 6.7, the horizontal axis corresponds to the actual n_1 value and the vertical axis corresponds to the actual n_2 value in the model tested, the color map is the parameters error.

The error distribution corresponding to the extracted n_1 is shown in Figure 6.4 . The figure shows that n_1 can be extracted to better than ± 0.01 in most of the $n_1 : n_2$ space investigated. In particular for $n_1 < 1.55$, the error is consistently less than ± 0.001 an area of interest as it is the more desirable for biological applications. The irregularities appear on the top right and the narrow band on the bottom of the

figure correspond to the models that their optical thicknesses could not be determined correctly as described previously in section 5.5.1. For the narrow band on the bottom, the last interface could not be seen by the program so the second layer's optical thickness has not been determined correctly.

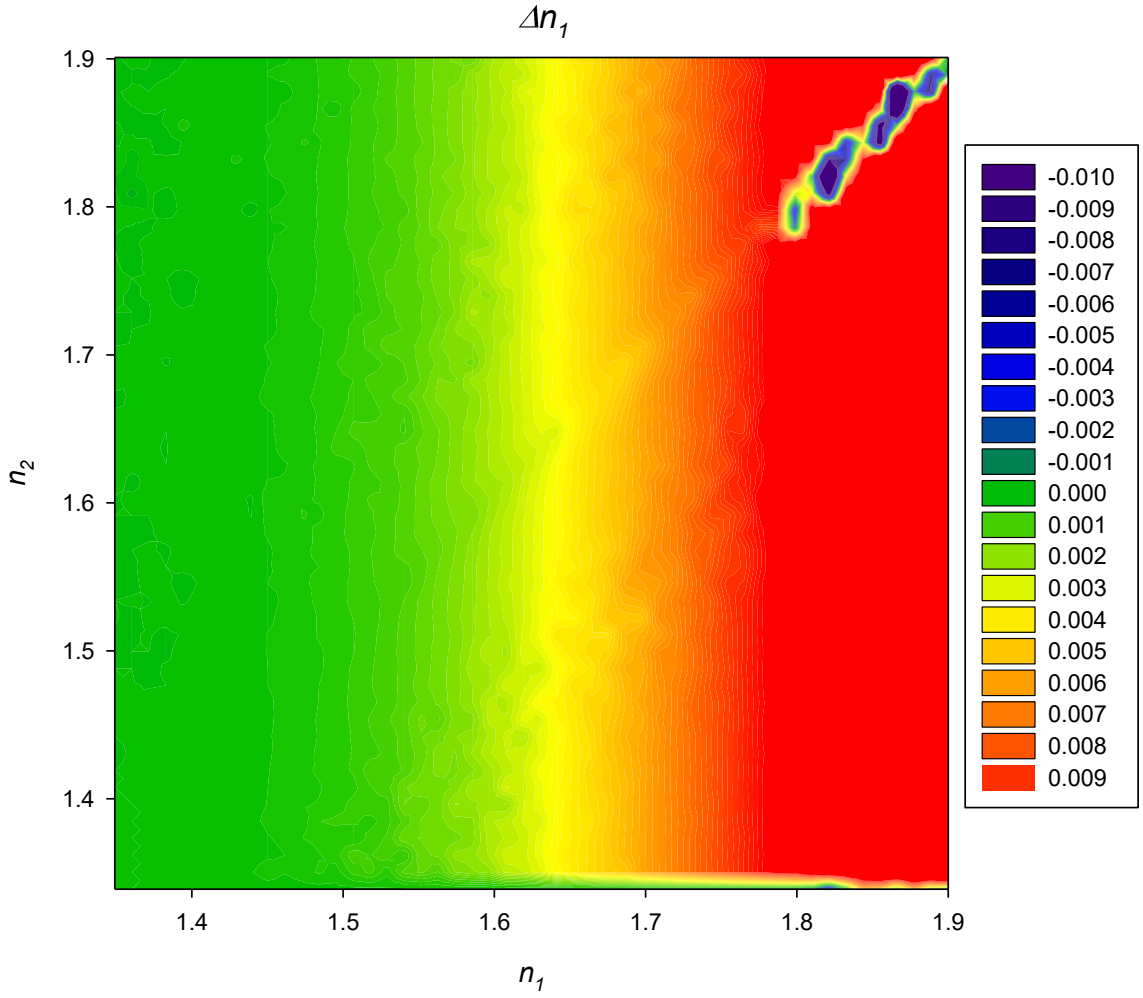

Figure 6.4: The contour map corresponding to error distribution of the extracted n_1. The horizontal axis corresponds to varying n_1 and the vertical axis corresponds to varying n_2.

The error distribution corresponding to the extracted n_2 is shown in Figure 6.5 . The figure shows that the accuracy of the extracted n_2 is degraded in comparison to

n_1. The region with error in n_2 of ± 0.01 or less is now restricted to roughly $n_2 < 1.75$. Particularly the region for having the error less than ± 0.001 is roughly restricted to $n_1 < 1.70$ and $n_2 < 1.55$.

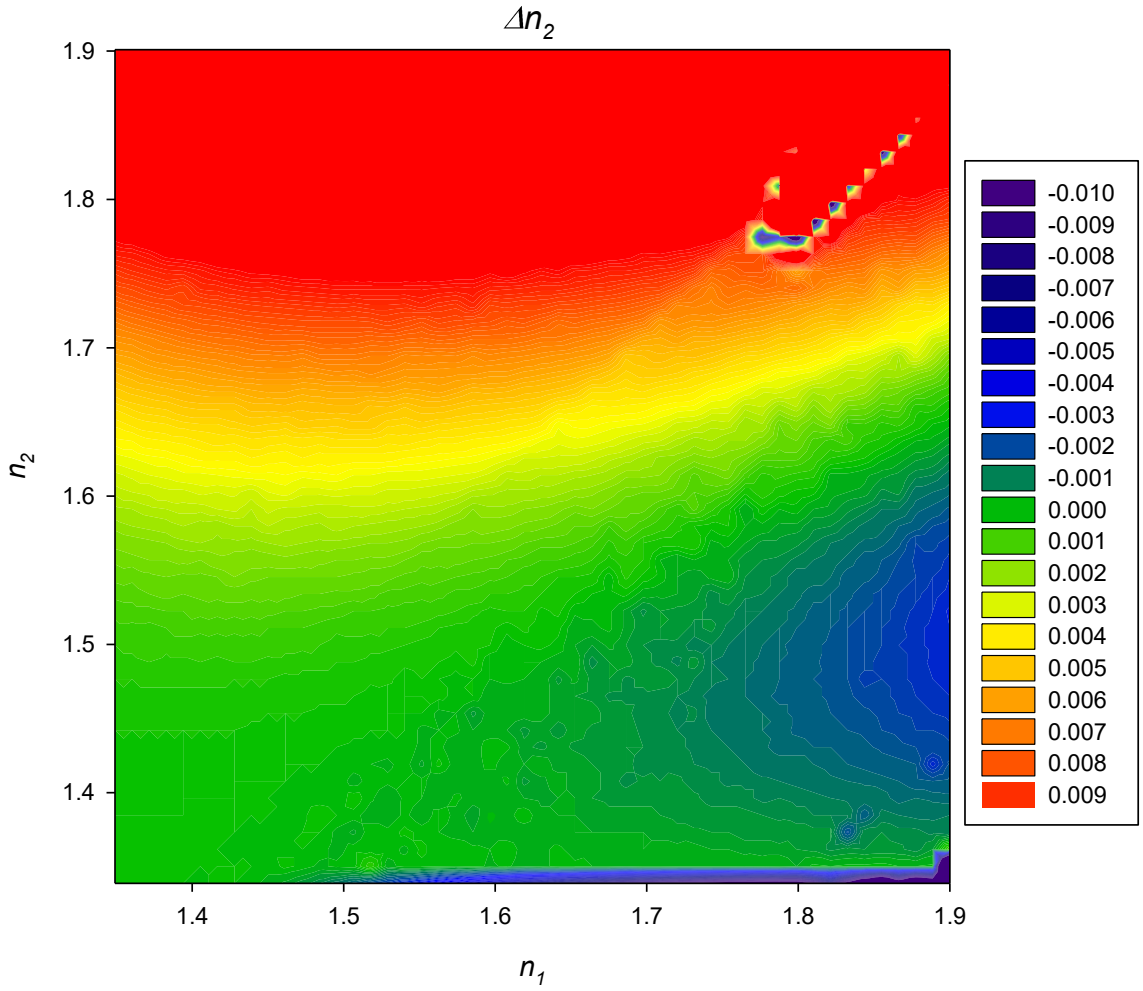

Figure 6.5: The contour map corresponding to the error distribution of the extracted n_2. The horizontal axis corresponds to varying n_1 and the vertical axis corresponds to varying n_2.

The error distribution corresponding to the extracted n_3 is shown in Figure 6.6. This figure shows that n_3 can be extracted with an error of ± 0.01 or less for majority of cases excluding the regions with irregularities. Particularly the region

for having the error less than ± 0.001 is restricted to the region with $n_1 < 1.60$ and $n_2 < 1.70$.

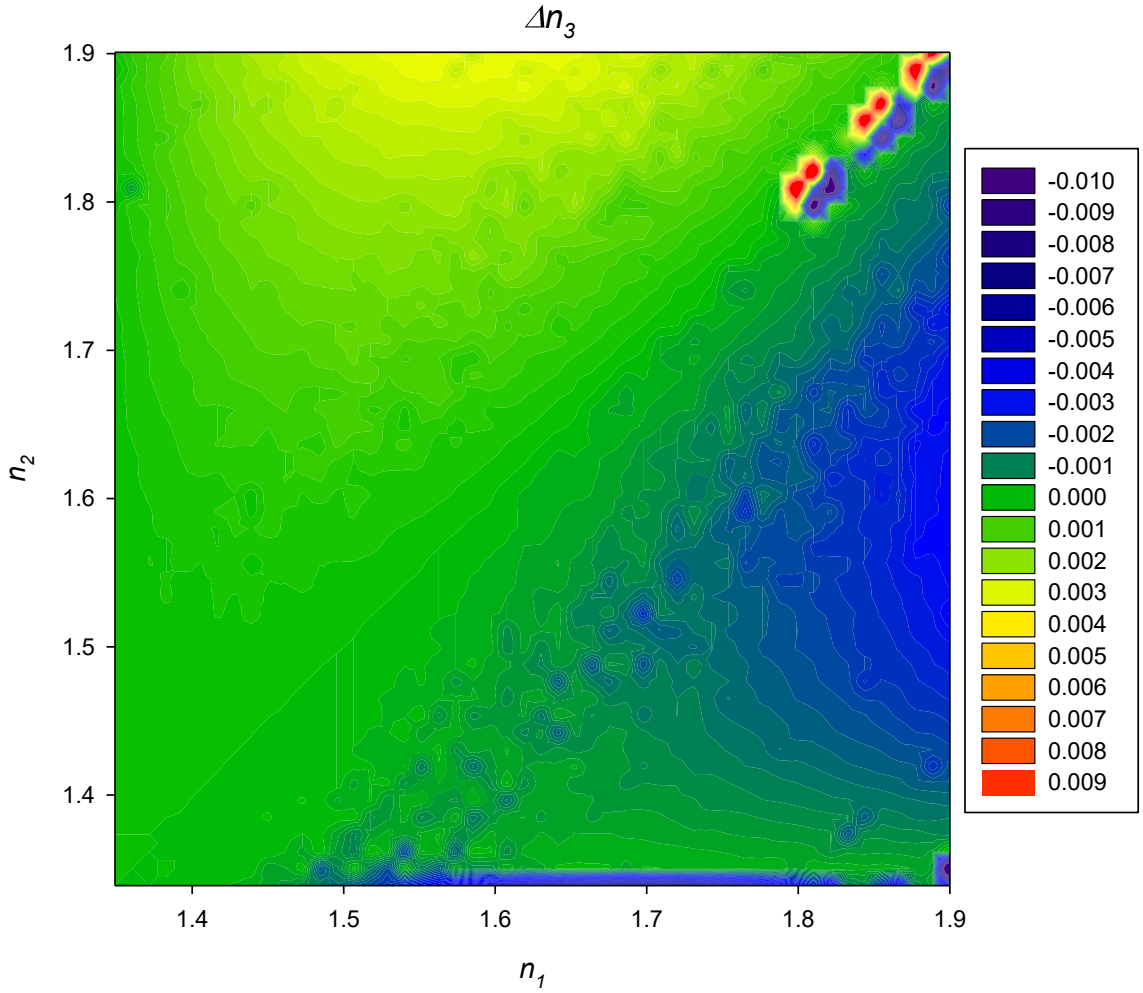

Figure 6.6: The contour map corresponding to the error distribution of the extracted n_3. The horizontal axis corresponds to varying n_1 and the vertical axis corresponds to varying n_2.

The relative error distribution corresponding to the extracted thicknesses ($\Delta d_{1,2}/d_{1,2}$) is shown in Figure 6.7. On the left pane is shown the relative error in d_1 and on the right pane is shown the relative error in d_2. The relative error in $d_{1,2}$ follows the pattern of corresponding indices $n_{1,2}$ and their relationship is described

in Eq(6.1). Like the previous figures, the irregularities on the top right corresponds to models with incorrectly determined optical thicknesses and the narrow band on the bottom of the right pane corresponds to cases where the second layer optical thickness has been poorly determined.

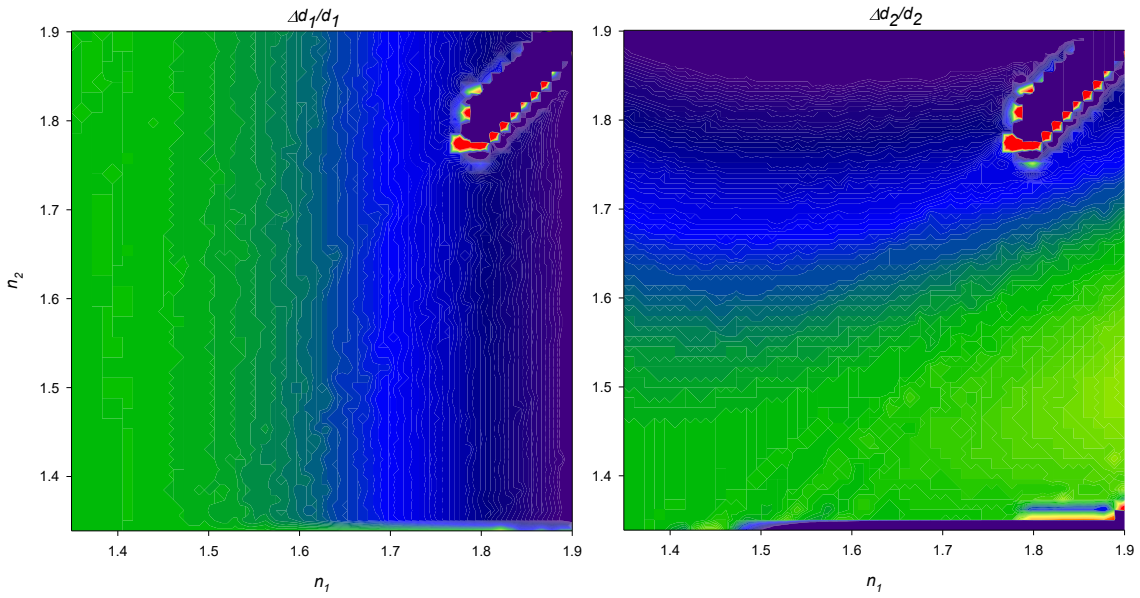

Figure 6.7: The contour map corresponding to the relative error distribution of the extracted thicknesses. The horizontal axis corresponds to varying n_1 and the vertical axis corresponds to varying n_2. The left pane corresponds to the relative error in d_1 and the right pane corresponds to the relative error in d_2.

In conclusion, the accuracy of the extracted parameters using the method of index/thickness measurement introduced in section 4.2.1 depends on the index contrast. For biological applications one may look for extracting parameters within the error range of ± 0.001. This range of error can be achieved for all indices (n_1, n_2, n_3) when the sample layer's indices are roughly limited to $n_1 < 1.55$ and $n_2 < 1.55$. This limitation is not a factor for biological system where n rarely exceeds 1.45.

6.1.2. The impact of sample thickness

The impact of thickness on extracting the parameters is evaluated in this section. The test models are again two layer systems and the parameters to be extracted are the index/thickness of each layer and the last medium index of refraction, i.e. n_1 , n_2, n_3, d_1, d_2 assuming that the front medium index of refraction is known. This time, the indices are fixed but layer thicknesses are varied. Two illustrative sample models are considered for this test, one with a low index contrast and one with high index contrast (equivalent to the common biological applications). The samples indices are listed in Table 6.1. Two test results are illustrated in this section corresponding to varying d_2 and varying d_1 respectively.

Table 6.1: Two example cases with low and high contrast in refractive indices

	Low Contrast Index	High Contrast Index
n_0	1.337	1.337
n_1	1.345	1.422
n_2	1.351	1.442
n_3	1.337	1.337

In Figure 6.8 the thickness of the first layer is fixed at 30 μm and the thickness of the second layer varies from 10 μm up to the maximum detectable range of the simulation system (2.18 mm in total optical thickness noted in Table 5.1) in 20 μm increments. For the low contrast case this range is up to 1580 μm and for the high contrast case 1480 μm. The situation is reversed in Figure 6.9 where the thickness

of the second layer is fixed at 30 μm and the thickness of the first layer varies from 10 μm up to the maximum detectable range of the simulation system (1570 μm for the low contrast and 1490 μm for the high contrast case) in 20 μm increments. The lower limit of the varying thickness is chosen to correspond to be close to the stable region of optical thickness measurement in Figure 5.6. The vertical axis in Figure 6.8 and Figure 6.9 is the error in the extracted parameters and the horizontal axis is the varying thickness. In these figures, the left panes show the errors in the index of refraction and the right panes show the errors in the thicknesses. Both the low contrast (top) and high contract (bottom) case are shown.

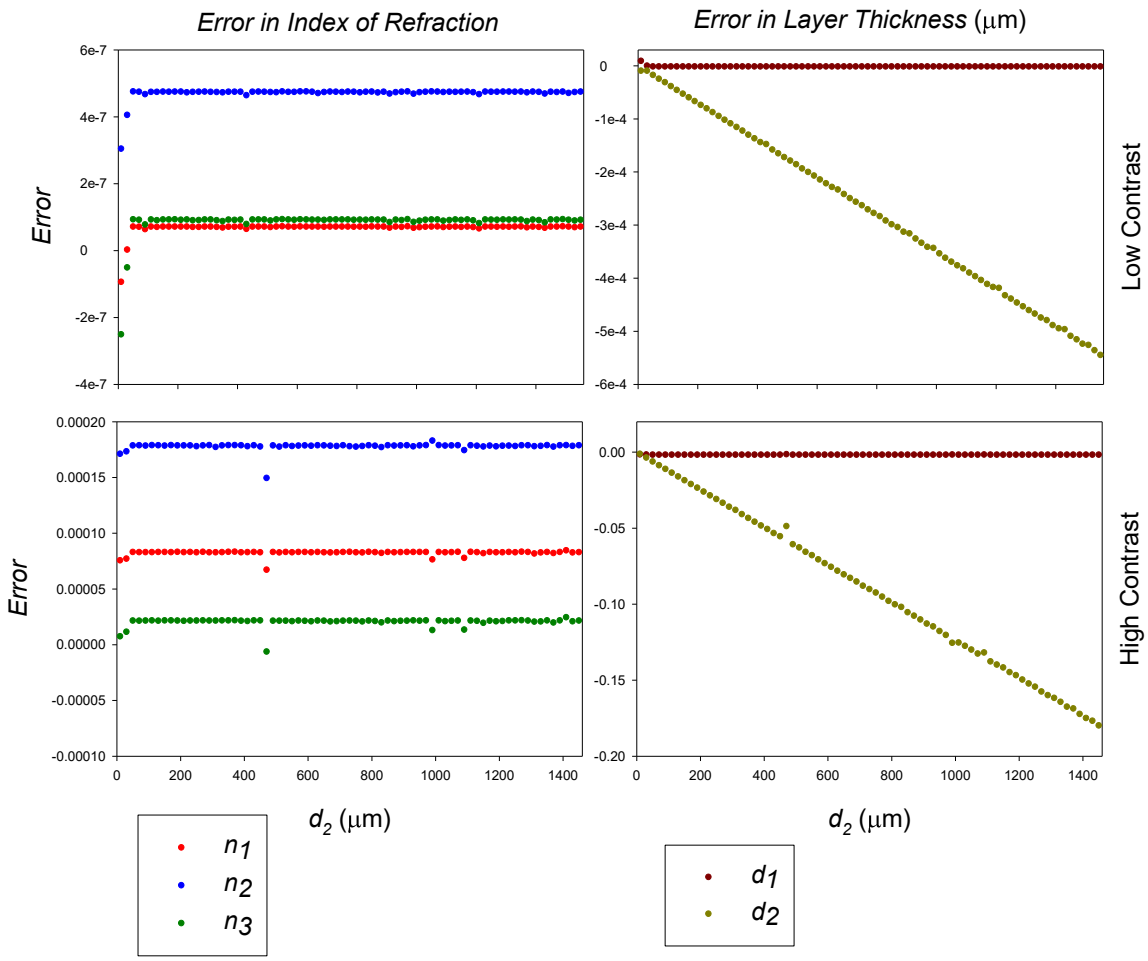

Figure 6.8: Impact of sample thickness (varying d_2) on the accuracy of the sample's extracted parameters. On the left panes are shown the errors associated with the refractive indices and on the right are shown the errors associated with the thicknesses. Both a low contrast (top) and high contrast (bottom) case are shown.

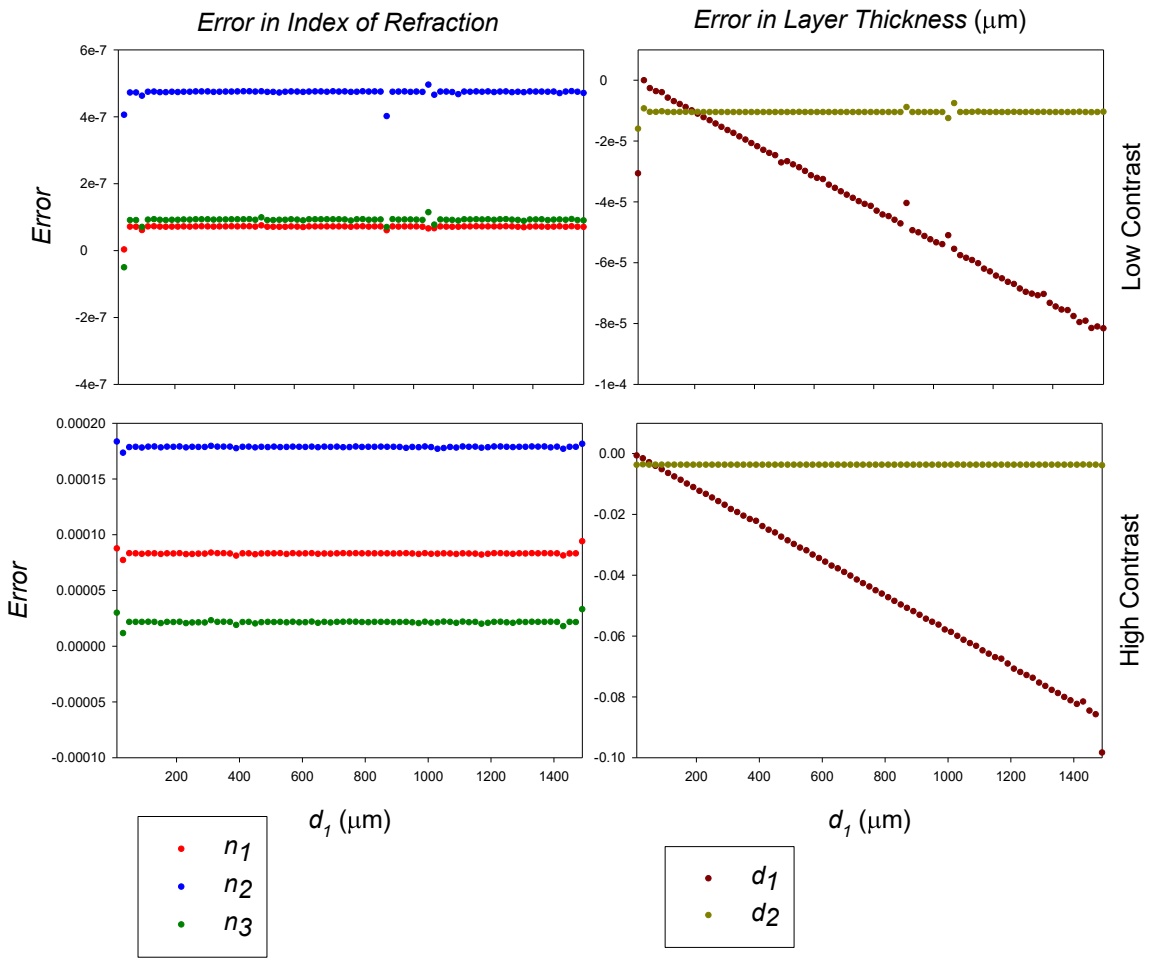

Figure 6.9: Impact of sample thickness (varying d_1) on the accuracy of the sample's extracted parameters. On the left panes are shown the errors associated with the refractive indices and on the right are shown the errors associated with the thicknesses. Both a low contrast (top) and high contrast (bottom) case are shown.

From the left panes of Figure 6.8 and Figure 6.9, it can be seen that the error of index extraction is insensitive to the sample's thickness profile. For the low contrast case in both figures, the errors in n_1 , n_2, n_3 are of the order of $\sim 10^{-8}$, $\sim 10^{-7}$, $\sim 10^{-8}$ respectively. For the high contrast case in both figures, the indices are of the order of $\sim 10^{-5}$, $\sim 10^{-4}$, $\sim 10^{-5}$ which is consistent with the expectation that errors in the index of refractions calculations will be larger for higher contrast due to the

increasing amplitudes of the multiple reflections. It also shows that n_1 can be extracted with better accuracy than n_2. This is because in Eq(4.14) for extracting n_1 from r_1, the first medium index in assumed to be known exactly so only one parameter needs to be estimated. Some data points on left panes of Figure 6.8 and Figure 6.9 appear to be out of the trend. The first few data points correspond to the optical thickness region producing unstable measurement in Figure 5.6. For the other points, the difference with the rest of the points is too small and negligible.

Since the thicknesses are extracted from the refractive indices via $d_{1,2} = \delta_{1,2}/n_{1,2}$, their error is directly proportional to the error in the refractive indices which is determined by Eq(6.1). On the right pane of Figure 6.8 and Figure 6.9, the relative error in d_1 for the low contrast cases are 5.20×10^{-8} and 5.19×10^{-8} respectively. They are consistent with the order of error in n_1 and show no difference between varying d_2 or varying d_1. For the high contrast cases, the relative errors in d_1 are 5.64×10^{-5} and 5.85×10^{-5} . They are consistent with the order of error in n_1 and again show no difference between varying d_2 and varying d_1. The same argument is true about the relative error of d_2 on the right pane of Figure 6.8 and Figure 6.9. For the low contrast cases, the relative error in d_2 are 3.59×10^{-7} and 3.52×10^{-7}. For the high contrast cases they are 1.25×10^{-4} and 1.24×10^{-4}. The order of errors are again consistent with the order of error in n_2 and show no difference between varying d_2 and varying d_1.

6.2. Measurement – Constrained Optical Thickness Data

In this section the method introduced in chapter 5 for the simultaneous measurement of index/thickness is going to be tested for the more realistic situation where the optical thicknesses are not known exactly. In an ideal situation where the actual optical thickness (OT) is known exactly, the introduced matrix equation, Eq(4.12), can be solved for any wavenumber components as long as the determinant is not zero. However, in practice there is always uncertainty (ε) associated with the measured OT (δ') so the value input into the parameter extraction algorithm

$$\delta' = \delta \pm \varepsilon, \tag{6.2}$$

may deviate from the actual OT (δ). Since the matrix in Eq(4.12) is constructed from the measured OTs, there is a non-linear frequency shift between the matrix and the signal on the right hand side of Eq(4.12). Therefore the extracted parameters are wavenumber dependent and inappropriate selection of the wavenumber components leads to erroneous results. Given that this matrix equation presents a coupled set of transcendental equations containing index terms on both sides of the equal signs, the impact of ε on index determination is not transparent so the behavior of the extracted parameters is best investigated by simulation. In this section a framework for selecting the best possible spectral components for these cases is developed. The impact of a range of ε on the extracted parameters will be investigated in the next chapter.

The impact of measurement uncertainty on the efficacy of parameter extraction is now demonstrated for specific measurement errors. A two layer system generated

with $n_0 = 1.337, n_1 = 1.345, n_2 = 1.351, n_3 = 1.337$, and $d1 = 10$ μm and $d2 = 30$ μm is considered and errors of $\varepsilon_1 = +3$ nm for the first layer and $\varepsilon_2 = +10$ nm for the second layer are arbitrarily introduced, to mimic measurement uncertainty. Although the variation of the errors with $\varepsilon > 0$ and $\varepsilon < 0$ are not symmetric, our tests have shown that the whole discussion with $\varepsilon > 0$ is also valid for $\varepsilon < 0$. In order to solve Eq(4.12), three spectral components are needed (k_1, k_2, k_3). We fix two k values at arbitrary values and sweep the third to investigate the behavior of the behavior of the extraction algorithm. We set $k_1 = 6.80$ (μm^{-1}), $k_2 = 6.85$ (μm^{-1}) and sweep k_3 from 6.85 to 7.00 (μm^{-1}) in 7.2×10^{-4} (μm^{-1}) increment (the spectrometer resolution given in Table 5.1). The errors in extracted indices are shown in Figure 6.10 and of the errors in extracted thicknesses are shown in Figure 6.11. In these figures, the vertical axis is the error in the extracted parameters and the horizontal axis is k_3. The determinant of the matrix is also plotted on the figures (the right axis),its importance is discussed in the next few paragraphs.

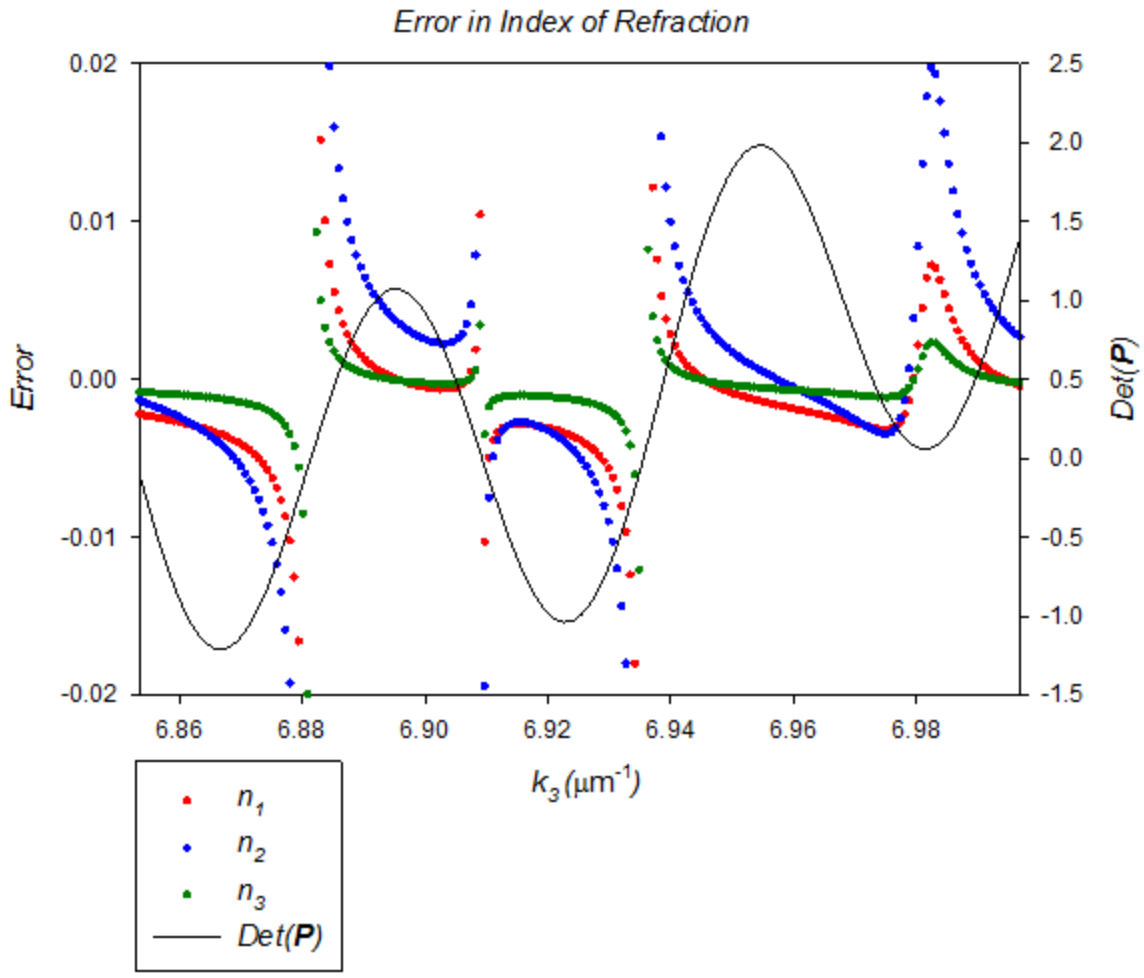

Figure 6.10: The dependence of the extracted indices error as a function of wavenumber selection for a two layer system. The left axis is for error, and the right axis show the determinant value. Two of the wavenumbers are chosen at arbitrary values and the third k3 is scanned. In this illustrative example $n_0 = 1.337$, $n_1 = 1.345, n_2 = 1.351, n_3 = 1.337, d_1 = 10$ µm, $d_2 = 30$ µm. The introduced error in OT is $\varepsilon_1 = +3$ nm for the first layer and $\varepsilon_2 = +10$ nm for the second layer. The chosen wavenumbers are $k_1 = 6.80$ µm^{-1}, $k_2 = 6.85$ µm^{-1} and k_3 swept from 6.85 µm^{-1} to 7.00 µm^{-1} in 7.2×10^{-4} µm^{-1} increments.

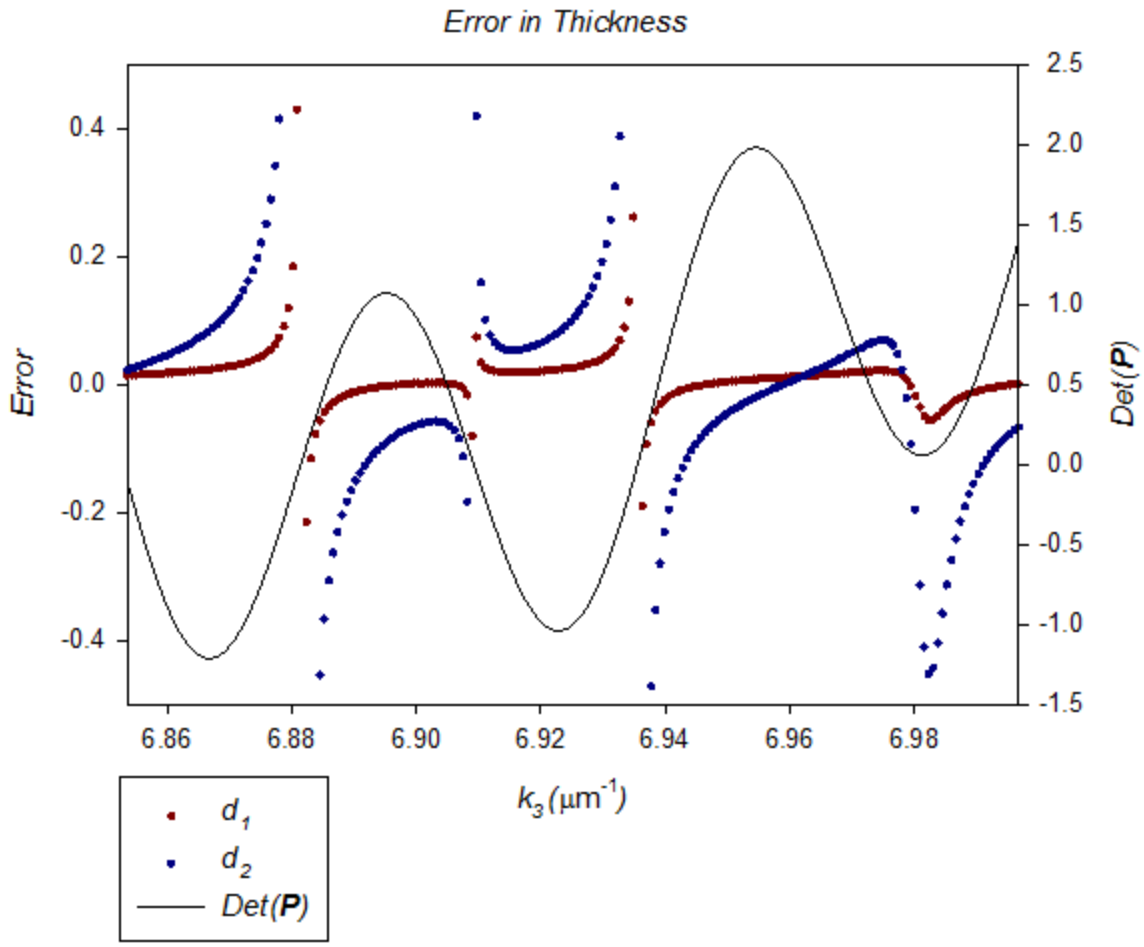

Figure 6.11: The dependence of the extracted thicknesses error as a function of wavenumber selection for a two layer system. The left axis is for error, and the right axis show the determinant value. Two of the wavenumbers are chosen at arbitrary values and the third k3 is scanned. In this illustrative example $n_0 = 1.337$, $n_1 = 1.345, n_2 = 1.351, n_3 = 1.337, d_1 = 10$ µm, $d_2 = 30$ µm. The introduced error in OT is $\varepsilon_1 = +3$ nm for the first layer and $\varepsilon_2 = +10$ nm for the second layer. The chosen wavenumbers are $k_1 = 6.80$ µm^{-1}, $k_2 = 6.85$ µm^{-1} and k_3 swept from 6.85 µm^{-1} to 7.00 µm^{-1} in 7.2×10^{-4} µm^{-1} increments.

From Figure 6.10 and Figure 6.11 it is seen that the errors in extracted parameters varies with wavenumber. The errors grow rapidly wherever the determinant is close to zero as we expected from the discussion in section 4.2.2. One important aspect that can be seen from the figures is that the errors of the extracted

parameters are minimized around the regions where the determinant has its maximum amplitude. Particularly around the largest value of the determinant, all indices errors are reduced simultaneously. Since the determinant value solely depends on the chosen set of the spectral component, we may conclude from the observation on Figure 6.10 and Figure 6.11, that in order to reduce (if not minimize) the error of all the extracted parameters, we may look for a set of wavenumbers (k_1, k_2, k_3) that provide large magnitudes (if not maximizes) of the determinant.

It must be emphasized that since the relation between the error of the extracted parameters and the wavenumbers is very complex we use a heuristic search to find a suitable set. Thereby it may not be the best selection and the extracted parameters may not be the perfect result but good enough for our present purpose and generalizing the approach is needed. Since we know that the wavenumber components that make zero determinant must be avoided, this provides us a reliable method to disregard some of the wavenumbers within our heuristic approach. The algorithm for finding such combinations is given in the next section.

6.2.1. Finding the suitable wavenumber components

As observed in the previous section, in order to reduce the error in the extracted parameters in the presence of OT measurement errors, the wavenumber components should be chosen so the determinant is maximized. The algorithm to find such components is described below.

According to Hadamard's maximum determinant problem [136], for any $n \times n$ matrix $\boldsymbol{A}$ with entries in the closed unit disk $|a_{ij}| \leq 1$, the determinant satisfies

$$|\det \boldsymbol{A}| \leq n^{n/2} \tag{6.3}$$

The matrix given in Eq(4.13) for a two layer system is a 3×3 matrix where all the elements are cosine functions. Therefore the matrix satisfies the above condition and its determinant using Eq(6.3) satisfies

$$|det\, \boldsymbol{P}| \leq 3^{3/2} = 5.196 \tag{6.4}$$

The formal approach to maximize the determinant of this matrix may be too complicated and out of the scope of this thesis. Hereby we do not take the formal approach to maximize the determinant and only look for a special arrangement good enough for our problem. One possible way to make the determinant given in Eq(4.13) close to its formal maximum given by Eq(6.4), since all of the elements are cosine functions, vary between [-1,+1], is to find a set of wavenumber components (k_1, k_2, k_3) for which all the cosine elements are ± 1. To start the discussion of how we find a suitable set of wavenumbers, suppose we find k_1 for which all elements in the first row of the determinant(4.13) i.e. $\cos\left(2k_1\Delta_{rz_0}\right)$, $\cos[2k_1(\Delta_{rz_0} - \delta'_1)]$ and $\cos[2k_1(\Delta_{rz_0} - \delta'_1 - \delta'_2)]$ are simultaneously $+1$. If we define a new function as

$$A(k) = \cos\left(2k\Delta_{rz_0}\right) + \cos\left[2k(\Delta_{rz_0} - \delta'_1)\right] + \cos\left[2k(\Delta_{rz_0} - \delta'_1 - \delta'_2)\right], \tag{6.5}$$

then the mentioned set (+1,+1,+1), corresponds to the maximum of $A(k)$, i.e. $A^{max} = 3$. If we find k_2 for which all elements in the second row of the determinant are simultaneously (-1,-1,-1), this set corresponds to minimum of $A(k)$, i.e. $A^{min} = -3$. Now if we use both sets corresponding to A^{max} and A^{min} to construct

the matrix, regardless of what we set for k_3, the determinant will be zero because two of the rows only differ by a minus sign. Therefore we are only allowed to use either A^{max} or A^{min}.

For the second wavenumber component k_2 we must look for another combination else than (+1,+1,+1) and (-1,-1,-1). This means that the new set must be a combination of +1 and -1. We define a new function as

$$B(k) = \cos\left(2k\Delta_{rz_0}\right) - \cos\left[2k(\Delta_{rz_0} - \delta'_1)\right] - \cos\left[2k\left(\Delta_{rz_0} - \delta'_1 - \delta'_2\right)\right]. \tag{6.6}$$

If we find k_2 for which the elements of the second row of the determinant are (+1,-1,-1) or (-1,+1,+1) , these sets correspond to maximum/minimum of $B(k)$ respectively and only one of the sets corresponding to $B^{max} = 3$ or $B^{min} = -3$ is allowed to be used to construct the matrix since they differ only by a minus sign.

For the third wavenumber component k_3 we must look for a combination of ± 1 other than (+1,-1,-1) or (-1,+1,+1). Therefore we define a new function as

$$C(k) = \cos\left(2k\Delta_{rz_0}\right) + \cos\left[2k(\Delta_{rz_0} - \delta'_1)\right] - \cos\left[2k(\Delta_{rz_0} - \delta'_1 - \delta'_2)\right]. \tag{6.7}$$

If we find k_3 for which the elements of the third row of the determinant are (+1,+1,-1) or (-1,-1,+1) , these sets correspond to maximum/minimum of $C(k)$ respectively and only one of the sets corresponding to $C^{max} = 3$ or $C^{min} = -3$ is allowed to be used to construct the matrix since they differ only by a minus sign. In this thesis we

choose the suitable wavenumber components k_1, k_2, k_3 from A^{max}, B^{max} and C^{max} conditions respectively and the determinant in this situation looks like

$$\begin{vmatrix} 1 & 1 & 1 \\ 1 & -1 & -1 \\ 1 & 1 & -1 \end{vmatrix} = 4. \tag{6.8}$$

In this thesis the approach we take to choose a suitable set of wavenumbers k_1, k_2, k_3 is to define the functions $A(k)$, $B(k)$ and $C(k)$ given above for the simulation program. The program finds the wavenumber (k_1) corresponding to A^{max}, k_2 corresponding to B^{max} and k_3 corresponding to C^{max}. Of course there are other combinations for the wavenumbers producing the same (or larger) magnitude of the determinant, in this thesis we restrict ourselves to the mentioned combinations suitable enough for our problem.

This method can be generalized to any multi-layer systems. As described in section 4.3, for a N-layer system we need $N+1$ spectral components. These components can be obtained, after rearranging the functions introduced above, from the following set of equations

$$A_1(k) = \cos\left(2k\Delta_{rz_0}\right) + \sum_{j=1}^{N} \cos\left[2k\left(\Delta_{rz_0} - \sum_{i=1}^{j} \delta'_i\right)\right],$$

$$A_2(k) =$$

$$\cos\left(2k\Delta_{rz_0}\right) + \sum_{j=1}^{N-1} \cos\left[2k\left(\Delta_{rz_0} - \sum_{i=1}^{j} \delta'_i\right)\right] - \cos\left[2k\left(\Delta_{rz_0} - \sum_{i=1}^{N} \delta'_i\right)\right], \tag{6.9}$$

$$A_3(k) =$$

$$\cos\left(2k\Delta_{rz_0}\right) + \sum_{j=1}^{N-2} \cos\left[2k\left(\Delta_{rz_0} - \sum_{i=1}^{j} \delta'_i\right)\right] - \sum_{j=N-1}^{N} \cos\left[2k\left(\Delta_{rz_0} -\right.\right.$$

$$\sum_{i=1}^{j} \delta'_i)\Big],$$

$$\vdots$$

$$A_{N+1}(k) = \cos\big(2k\Delta_{rz_0}\big) - \sum_{j=1}^{N} \cos\Big[2k\big(\Delta_{rz_0} - \sum_{i=1}^{j} \delta'_i\big)\Big].$$

The wavenumber components k_1, k_2,... k_{N+1} can be obtained from the conditions: ${A_1}^{max}(k)$, ${A_2}^{max}(k)$,... ${A_{N+1}}^{max}(k)$ respectively.

6.2.2. Example results for a suitable wavenumber selection

We use the algorithm introduced in section 6.2.1 to investigate the error behavior of the extracted parameters of the two layer system given earlier in section 6.2 with $n_0 = 1.337, n_1 = 1.345, n_2 = 1.351, n_3 = 1.337$, $d1 = 10$ μm, $d2 = 30$ μm and with error $\varepsilon_1 = +3$ nm for the first layer and $\varepsilon_2 = +10$ nm for the second layer. The suitable wavenumber components are found by the method described in the previous section yielding $k_1 = 6.5182$ (μm^{-1}) corresponding to $A^{max} = 2.840$, $k_2 = 8.5240$ (μm^{-1}) corresponding to $B^{max} = 2.999$ and $k_3 = 8.6406$ (μm^{-1}) corresponding to $C^{max} = 2.999$. The determinant using this set of wavenumbers is

$$\begin{vmatrix} 1 & 0.852 & 0.988 \\ 1 & -0.999 & -0.999 \\ 1 & 0.999 & -0.999 \end{vmatrix} = 3.977, \qquad (6.10)$$

very close to the value given in Eq(6.8). In order to show the behavior of the errors, we fix k_1 and k_2 at the given values by the algorithm and sweep k_3 from 8.5240 to 8.67 (μm^{-1}) in 7.2×10^{-4} (μm^{-1}) increment (as the spectrometer resolution given in Table 5.1). The resulting extracted indices error are shown on Figure 6.12 and that of thicknesses are shown on Figure 6.13. The determinant of the matrix is also

plotted as a reference in the figures (the right axis). The reason for plotting the determinant is now clear. It can be observed from Figure 6.12 that the error of all extracted indices is reduced simultaneously around the maximum of the determinant. The errors diverge rapidly where the determinant is zero. For the error of thicknesses in Figure 6.13, the best k3 is not at the determinant's apex. This is not unexpected since the errors in thicknesses from Eq(6.1) must compensate for the error in OT since we are optimizing the n values. The relation between the error of the extracted parameters and the determinant that is observed in Figure 6.12 and Figure 6.13 needs to be generalized, but we do not do so in this thesis. The errors of the extracted parameters at the specified point on Figure 6.12 and Figure 6.13 for the particular given example are $n_1^{actual} - n_1^{extracted} = 3.23 \times 10^{-4}$, $n_2^{actual} - n_2^{extracted} = 2.98 \times 10^{-4}$, $n_3^{actual} - n_3^{extracted} = 2.79 \times 10^{-4}$, $d_1^{actual} - d_1^{extracted} = -4.62 \times 10^{-3}$ μm and $d_2^{actual} - d_2^{extracted} = -1.39 \times 10^{-2}$ μm.

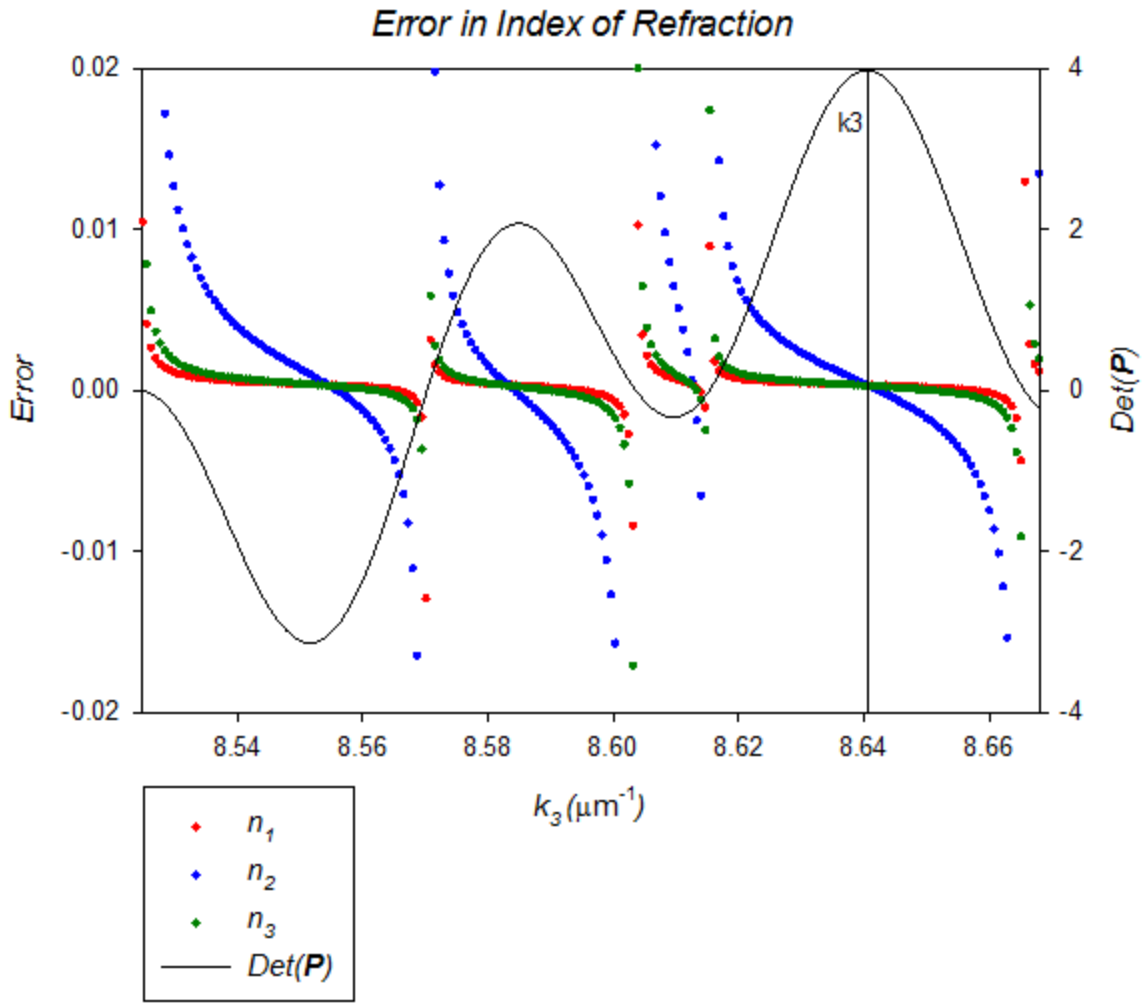

Figure 6.12: The variation in the extracted refractive index errors as a function of wavenumber for a two layer system. The left axis is for error, and the right axis is for the determinant matrix. The wavenumbers are obtained from the algorithm that maximizes the determinant. The value that is labeled by $k_3 = 8.6406$ (μm^{-1}), is obtained from the algorithm. In this illustrative example $n_0 = 1.337$, $n_1 = 1.345$, $n_2 = 1.351$, $n_3 = 1.337$, $d1 = 10$ μm and $d2 = 30$ μm. The introduced error for the first layer is $\varepsilon_1 = +3$ nm and for the second layer is $\varepsilon_2 = +10$ nm. The chosen wavenumbers are $k_1 = 6.5182$ (μm^{-1}), $k_2 = 8.5240$ (μm^{-1}) and k_3 is swept from 8.5240 to 8.67 (μm^{-1}) with 7.2×10^{-4} (μm^{-1}) increment.

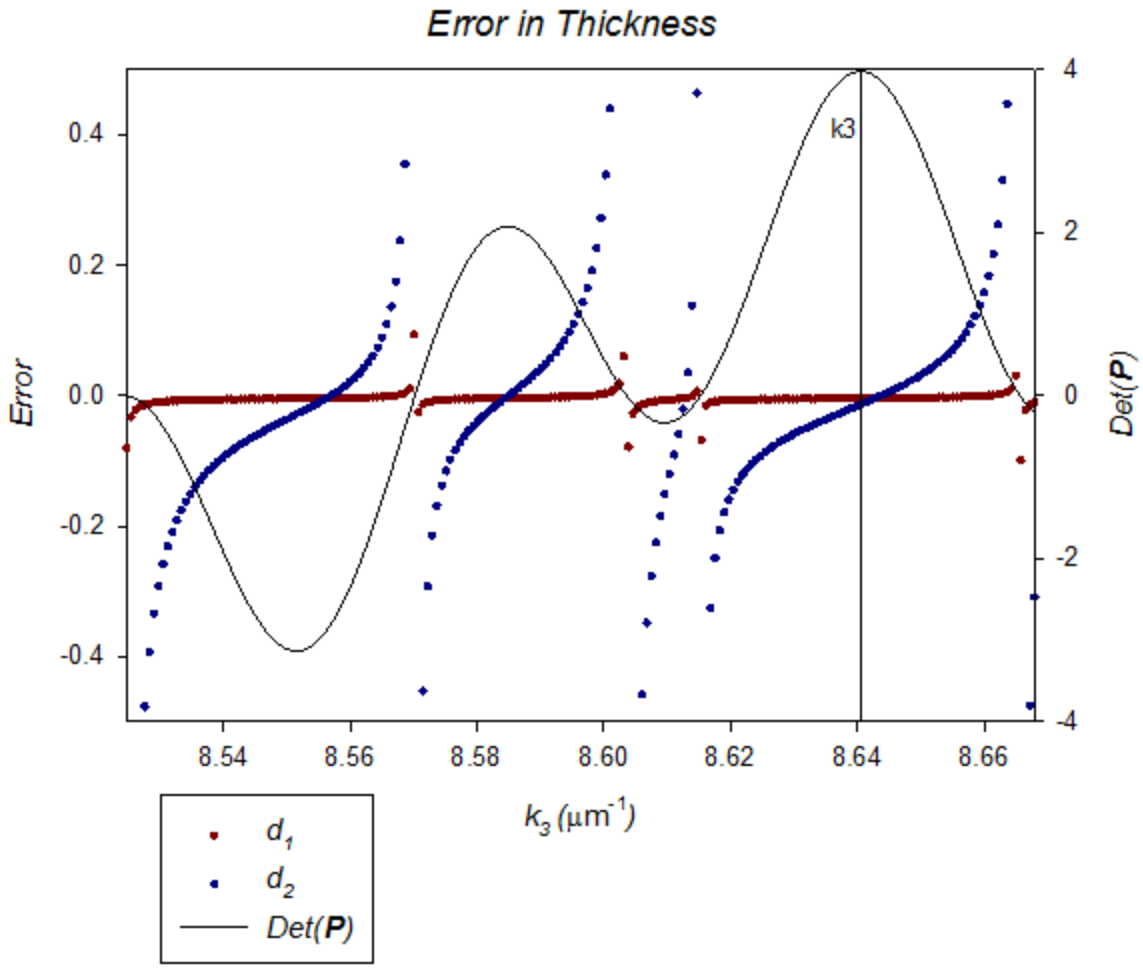

Figure 6.13: The variation in the extracted thickness errors as a function of wavenumber for a two layer system. The left axis is for error, and the right axis is for the determinant matrix. The wavenumbers are obtained from the algorithm that maximizes the determinant. The value that is labeled $k_3 = 8.6406$ (µm^{-1}) is the k maximizing the determinant as per the algorithm. In this illustrative example $n_0 = 1.337$, $n_1 = 1.345$, $n_2 = 1.351$, $n_3 = 1.337$, $d1 = 10$ µm and $d2 = 30$ µm. The introduced error for the first layer is $\varepsilon_1 = +3$ nm and for the second layer is $\varepsilon_2 = +10$ nm . The chosen wavenumbers are $k_1 = 6.5182$ (µm^{-1}), $k_2 = 8.5240$ (µm^{-1}) and k_3 is swept from 8.5240 to 8.67 (µm^{-1}) with 7.2×10^{-4} (µm^{-1}) increment.

It is useful to see where in the FD-OCT spectral response function where the selected wavenumbers reside. For this purpose the normalized signal (Eq.(4.8)) is plotted on Figure 6.14 and the wavenumber components obtained above are shown. It is seen that the wavenumbers almost correspond to the global/local extrema of the signal. If ε was zero, they would exactly reside on the global/local extrema of the signal. The deviation of the suitable wavenumbers from the signal's peaks increases with increasing ε. One may decide to stay with the signal's peaks but there is a risk of having a zero determinant. In other words, with selecting the wavenumbers based on the determinant, we know for sure which set of wavenumbers must be avoided but we can't get this knowledge from the signal's peaks. Some wavenumber combinations corresponding to the signal's peaks may produce zero determinants.

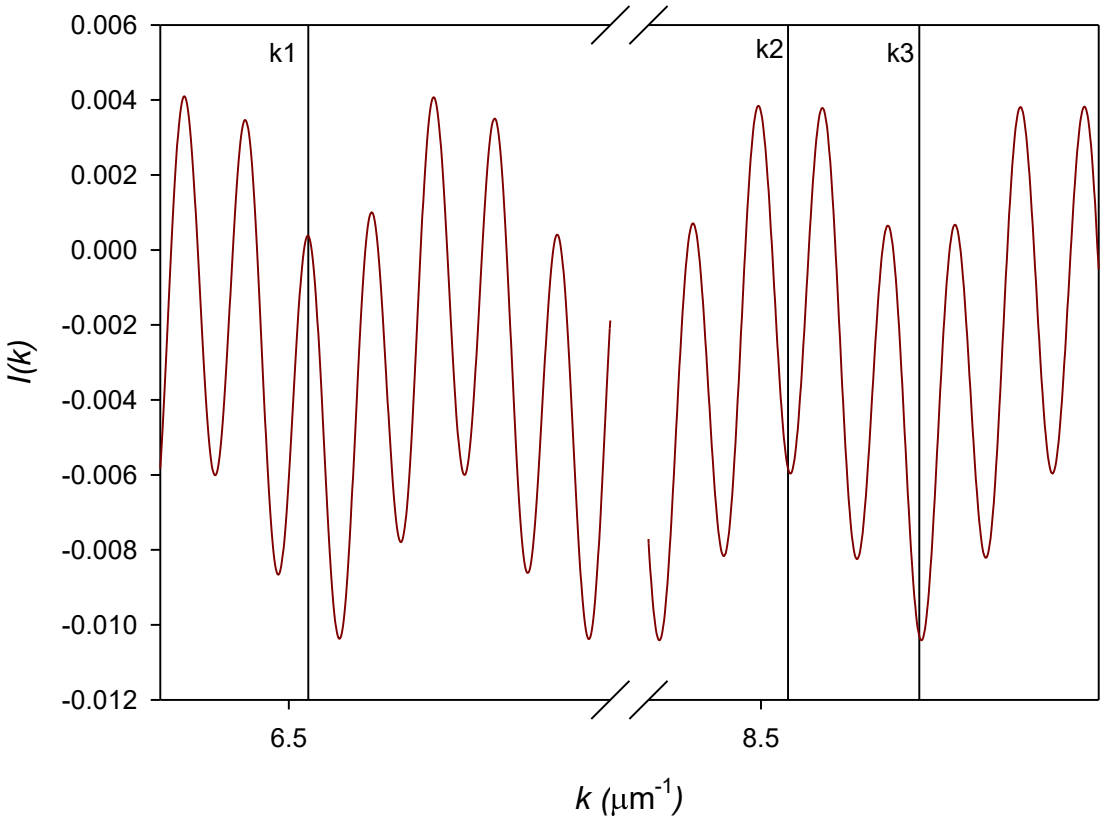

Figure 6.14: The normalized signal and the proper wavenumber components corresponding to Figure 6.12 and Figure 6.13. The indicated wavenumbers are $k_1 = 6.52\ (\mu m^{-1})$, $k_2 = 8.52\ (\mu m^{-1})$, $k_3 = 8.64\ (\mu m^{-1})$.

As ε increases, non-linear frequency shifts between the matrix and the normalized signal on the right hand side of Eq(4.12) increase, this introduces more error to the extracted parameters. There are some factors in FD-OCT imaging system, affecting the sharpness of layer boundaries and reducing the image contrast near the layer boundaries. The result would be that the peaks of the Fourier transformed data would be blurry and the exact position would be difficult to be determined which results in increased ε. For instance the shape of the peak may not be perfectly Gaussian, therefore the effective axial resolution is less than this

optimum value [125] or superimposed speckle noise on structural image reduces the image contrast near the layer boundaries [137] [138]. The effect of increasing ε on the parameters extraction will be described in the next chapter.

Chapter 7. Optimization

It was shown in Chapter 6 that in the presence of even small errors in the optical thickness estimates (ε) significant errors are introduced to the calculated refractive indices and layer thicknesses. The effect of increasing ε on the parameters extraction will be investigated in the first part of this chapter. The goal is to answer two main questions:

1) What is the maximum ε that still allows the extraction of the parameters from the new index/thickness measurement method?

2) What is the accuracy loss in each parameter as ε increases?

To answer these question we test a wide range of models with varying index contrast and thickness for a range of ε and investigate the extracted parameters error. In the second part of this chapter we develop, test and validate two optimization methods that help expand the range of applicability of the new method for extraction of the layered system's parameters.

7.1. Sample Parameters Extraction for a Range of ε

In order to investigate the impact of measured optical thickness error, ε, on the extracted parameters of two layer systems $(n_1, n_2, n_3, d_1, d_2)$, we recall the illustrative test models in Table 6.1, one with low and one with high contrast in indices and with $d_1 = 10$ μm and $d_2 = 30$ μm. We extract parameter in these two models for ε between $\varepsilon_{1,2} = 0$ to $\varepsilon_{1,2} = +10$ μm in 0.1 μm increment for each layer and compare the extracted indices and thickness as per the methodology developed

in chapter 6. The test result is shown on Figure 7.1 where the error in the extracted parameters (vertical axis) is plotted versus ε on the horizontal axis. The index error is shown on the left pane of Figure 7.1 and the thickness error is shown on the right pane. Both low contrast (top) and high contrast (bottom) cases are shown. The figure shows that even a small value of ε result in large errors in the extracted parameters as compared to $\varepsilon = 0$ case (section 6.1). It is seen from the right pane of Figure 7.1 that the error of extracted indices varies from -0.024 to +0.01 for the low contrast case and from -0.2 to +0.1 for the high contrast case. It shows that the extracted parameters error generally increases as the index contrast gets larger ($\sim$10-fold on the right pane of Figure 7.1), due to increasing multiple reflections as discussed in section 4.4.1. Since physical thickness is extracted from the optical thickness and corresponding index of refraction, the error of thickness on the right pane of Figure 7.1 is related to ε and error of index via Eq(6.1).

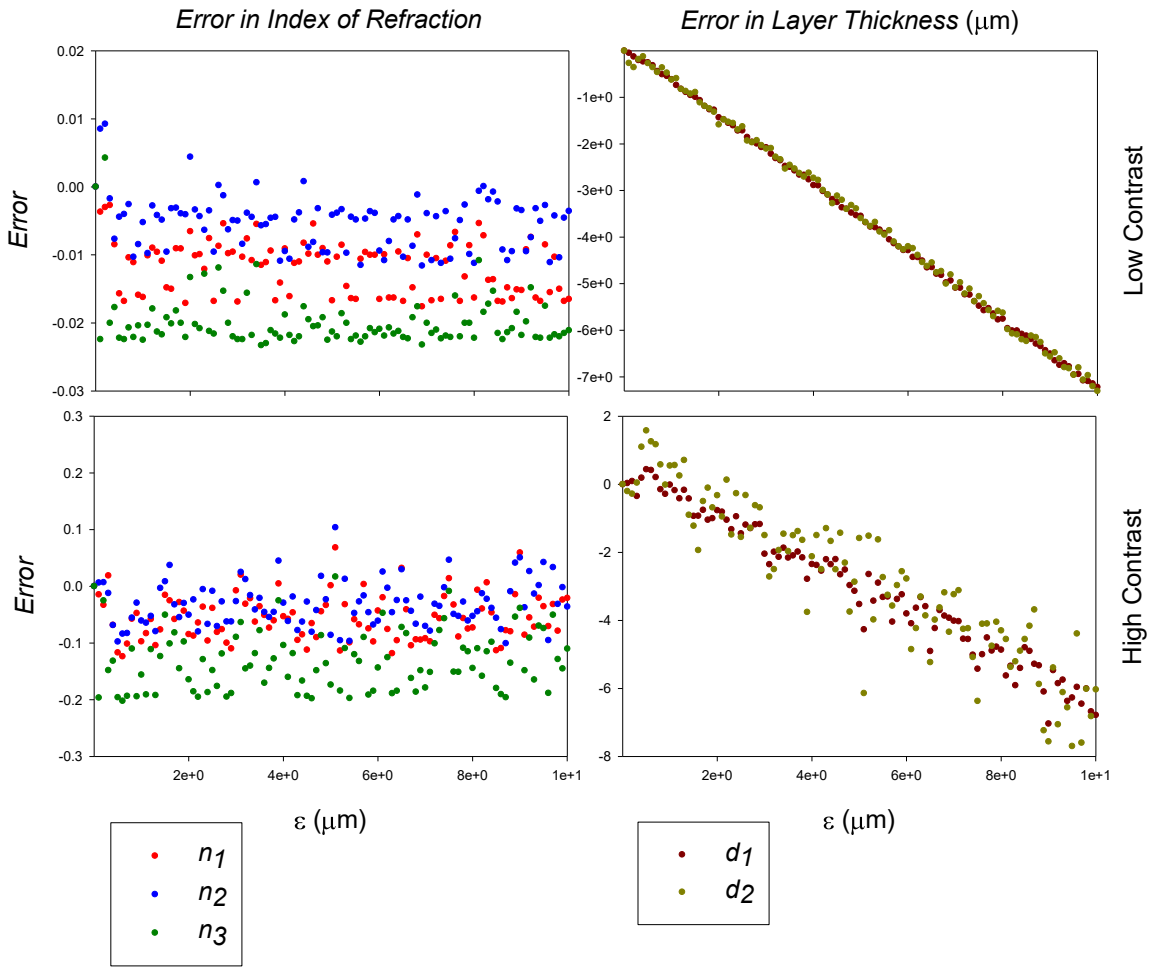

Figure 7.1: Impact of the optical thickness measurement error, ε, on the accuracy of the extracted parameters. On the left panes are shown the error of the extracted index of refraction and on the right are shown the error in the extracted thicknesses. Both the low contrast (top) and the high contract (bottom) cases are shown.

7.2. Approach to Parameter Improvements

It was shown in section 7.1 and in the previous chapter that in the realistic case of having a non zero ε the methodology introduce in chapter 6 can quickly result in significant errors. In order to enhance the parameters extraction, an additional process is needed. In the next two sections, we introduce two optimization methods and compare their outcomes. In the first optimization method (section 7.3), we

construct a model FD-OCT normalized signal similar to Eq(4.8) and Eq(4.9) and fit the model signal to the actual data obtained from digitally constructed TMM. In other words we try to fit a summation (single scattering) spectrum to the TMM (multiple scattering) spectrum. The floating parameters to be found are n_1 , n_2, n_3, d_1, d_2, where the extracted parameters obtained using the method of chapter 6 are used as initial guess values. In the second optimization method (section 7.4), The floating parameters to be found are n_1 , n_2, n_3, δ_1, δ_2. The extracted indices obtained in previous section together with the measured optical thicknesses are used as initial guess values.

The difference between two optimization methods is in the parameter searching and the algorithm used for this search. In the first method, the fitting algorithm searches for all indices and thicknesses simultaneously whereas in the second approach it searches for indices and optical thicknesses. In the second approach the thicknesses are extracted from the optimized optical thicknesses. It will be shown that the first optimization approach is limited only to a very narrow range of ε whereas the second approach works with wider range of ε.

7.3. The First Optimization Method

The first optimization method is based on fitting the spectral data to a modeled signal using the extracted parameters (n_1 , n_2, n_3, d_1, d_2) as initial guess values. In the first optimization method, for a two layer system, the modeled signal is similar to Eq(4.8) and Eq(4.9). We introduce the fitting parameters (floating parameters), b_1, b_2, b_3, b_4, b_5 representing for n_1, n_2, n_3, d_1, d_2 respectively in the modeled signal of the form,

$$f(b,k) =$$

$$\frac{n_0 - b_1}{n_0 + b_1} cos\left(2k\Delta_{rz_0}\right) + \frac{b_1 - b_2}{b_1 + b_2} cos\left[2k\left(\Delta_{rz_0} - b_1 b_4\right)\right] + \frac{b_2 - b_3}{b_2 + b_3} cos\left[2k\left(\Delta_{rz_0} - b_1 b_4 - b_b b_5\right)\right] \quad (7.1)$$

The initial guess values, extracted from Eq(4.12) based on the optimally selected wavenumbers algorithmically derived from the measured optical thickness are fed to this modeled signal and the fitting routine searches for optimized values of $\{b_i\}$ to fit the function $f(b,k)$ to the spectral data. In our simulation this is done by the "genfit" function in MathCad which employs an optimized version of the Levenberg-Marquardt method for minimization of the root mean square difference between the model and the data.

7.3.1. First Optimization Method for a Range of ε

In this section we test the first optimization method for a range of ε and to see if this method can provide correct values of indices and thicknesses given some specified accuracy for the measured OTs (compare to Figure 7.1). To illustrate the implementation of this approach, we recall the previous low and high contrast test models given in Table 6.1 with the thicknesses of $d_1 = 10$ μm and $d_2 = 30$ μm. We search for the parameters for ε between $\varepsilon_{1,2} = 0$ to $\varepsilon_{1,2} = +1$ μm with 0.01 μm increment for both layers. The upper bound of ε is set to 1 μm, which is almost the same size of one imaging cell (noted in Table 5.1). The test results are shown on Figure 7.2. In this figure, the deviation of the fitting parameters $\{b_i\}$ from their true values $\{n_i, d_i\}$ on the vertical axis is plotted versus ε on the horizontal axis. On the

left panes are shown the errors in the index of refraction parameters and on the right are shown the errors in the thickness parameters. Both the low contrast (top) and the high contract (bottom) cases are shown.

For biological application we may look for error in indices of less than 0.001. Figure 7.2 show that the first optimization method can extract parameters within the mentioned acceptable range for ε up to $\sim$50 nm for the low contrast case and decreases to $\sim$45 nm for the high contrast case as compared to only a few nanometers in Figure 7.1. This is mostly because the initial guess values within this range are close to the actual values so that the Marquart-Levenberg algorithm can converge to the real minimum. Also it shows that the range of acceptable ε depends on the contrast. A closer look at the region $\varepsilon \leq 40$ nm is shown on Figure 7.3. The quality of the results in this region is even better than the results obtained in Figure 6.9 for the low and high contrast cases with $\varepsilon = 0$. In the region $\varepsilon \leq 40$ nm, the error of n_1, n_2 and n_3 from the right pane of Figure 7.3, for the low contrast case are steady and on average they are of the order of $\sim 10^{-9}$, $\sim 10^{-8}$ and $\sim 10^{-7}$ respectively and of the order of $\sim 10^{-7}$, $\sim 10^{-5}$ and $\sim 10^{-5}$ for the high contrast case. The error of d_1 and d_2 from the left pane of Figure 7.3, for the low contrast case are on average of the order of $\sim 10^{-9}$ and $\sim 10^{-6}$ and for the high contrast of the order of $\sim 10^{-6}$ and $\sim 10^{-4}$ respectively. The results show that the error in the extracted parameters generally grows with contrast due to increase in the amplitude of multiple reflections (multiple scattering regime) while the model signal is based on single scattering regime.

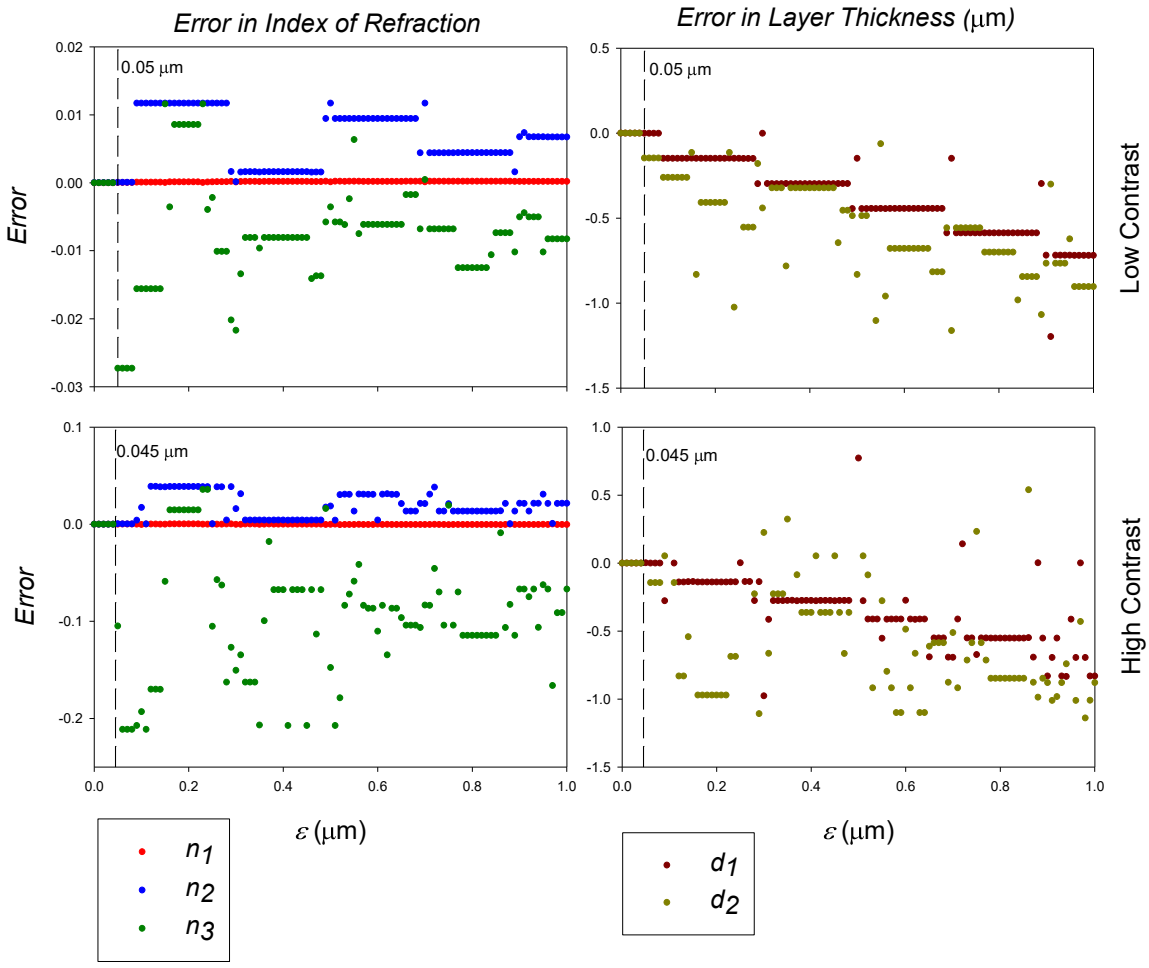

Figure 7.2: Impact of the optical thickness measurement errors, ε, on the accuracy of the first optimization method. On the left panes are shown the errors in the index of refraction and on the right are shown the errors in the thicknesses. Both a low contrast (top) and high contract (bottom) case are shown. The dashed lines indicate the maximum limit that the first optimization method can support for all parameters.

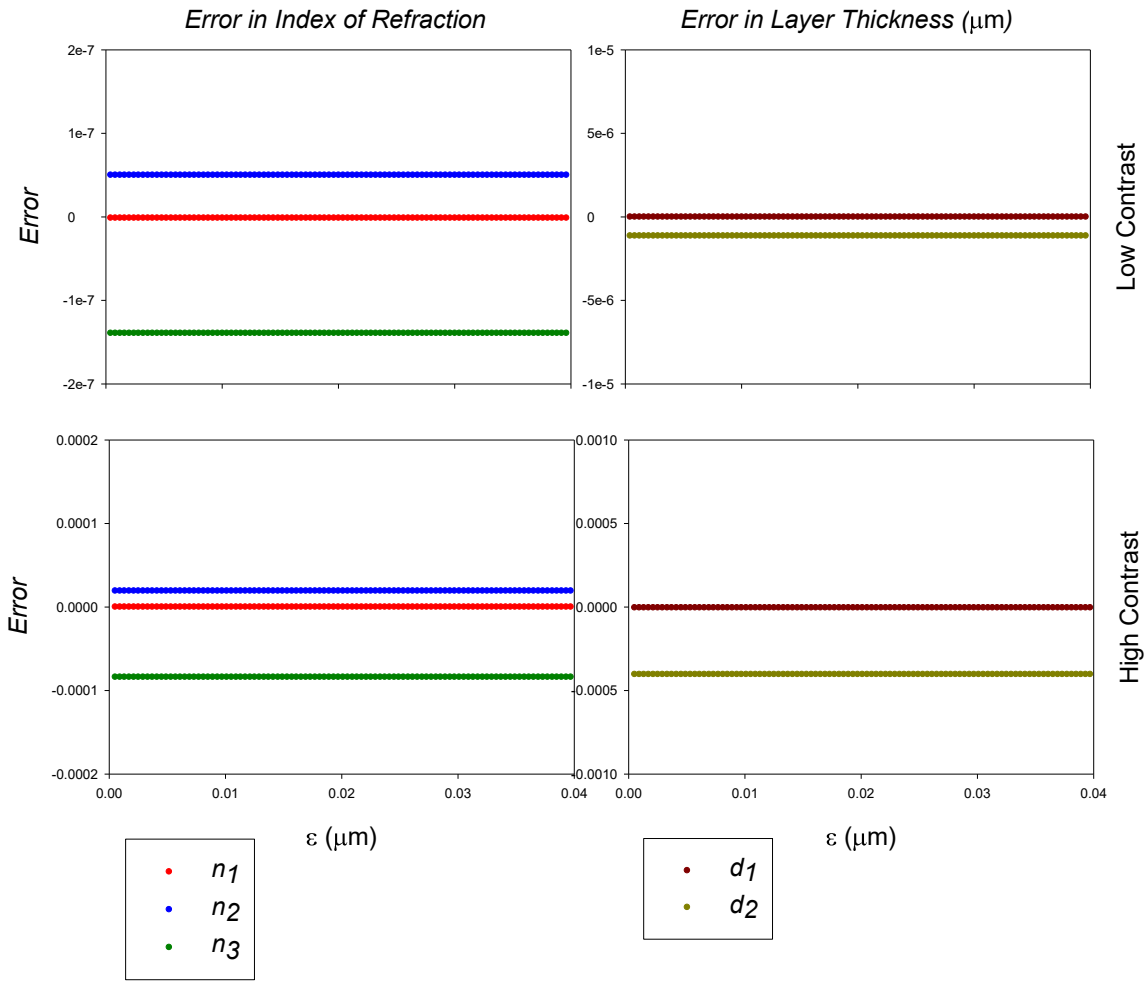

Figure 7.3: A zoom on the region with $\varepsilon \leq 0.04$ μm corresponding to Figure 7.2. On the left panes are shown the error of the index of refraction and on the right are shown the errors in the thicknesses. Both a low contrast (top) and high contract (bottom) case are shown. The dashed lines indicate the maximum limit that the first optimization method can support for all parameters.

7.3.2. First Optimization Method for a Range of Thickness

The quality of the first optimization method to extract parameters for a range of thickness is tested and results are shown in Figure 7.4. In this test $\varepsilon_{1,2}$ is fixed at $\varepsilon_{1,2} = 0.01$ μm. This value of ε is within the working range of the first optimization method (section 7.3.1). Both the low and the high contrast cases given in Table 6.1 are shown in Figure 7.4. The thickness of the first layer varies from 10 μm up to the

maximum detectable range of the simulation system (2.18 mm in total optical thickness noted in Table 5.1) in 20 μm increments. For the low contrast case the maximum physical thickness is 1570 μm and for the high contrast case is 1490 μm. The lower limit of the thickness is chosen according to Figure 5.6 to be close to the stable region of optical thickness measurement. The thickness of the second layer is fixed at 30 μm. It would describe the same physical situation if the first layer thickness is fixed and varying the second layer thickness. The test results are shown in Figure 7.4. In this figure the parameter errors on the vertical axis are plotted versus d_1 on the horizontal axis. On the left panes are shown the errors in the index of refraction and on the right are shown the errors in the thicknesses. Both the low contrast (top) and the high contract (bottom) case are shown.

It is seen from Figure 7.4 that the error in indices (the left pane) in the first optimization method is almost insensitive to the layer thicknesses. Also it can be seen that the errors are generally higher in magnitude for high contrast case as expected due to the increase in multiple reflections amplitudes (section 4.4.1) which affect the spectral response significantly and cannot be fitted properly with the summation model. If we compare Figure 7.4 with Figure 6.9 where $\varepsilon = 0$, it can be seen that the accuracy of extracting indices have been improved by about 10-fold by using the fitting to the spectrum.

On the right pane Figure 7.4, the error of thicknesses shows little sensitivity to the layer thicknesses except for the region near the maximum detectable range. This is not unexpected as at high thicknesses the spectral response has high frequency oscillations that the spectrometer resolution is unable to capture.. The improvement

achieved is more profound for thicknesses as compared to Figure 6.9 where the error increased with thickness but in Figure 7.4 it is almost constant. This is because in the first optimization method, the thickness is extracted from the fitting process unlike in Figure 6.9 that the thickness extracted from $\delta_{1,2}/n_{1,2}$. Therefore the error of thickness does not follow the same pattern as the error of index of refraction and merely depends on the fitting algorithm. The error of d_2 does not change significantly since this parameter is the same for each time that d_1 changes and the searching algorithm extracts this parameter within a certain limit of error. Also it can be seen that the errors are higher in magnitude for high contrast case as expected due to the increase in multiple reflections amplitudes (section 4.4.1). On average, the error's order of magnitude in Figure 7.4 is consistent with that of Figure 7.3. Therefore we may conclude that the indices contrast and ε are two main factors affecting the error of extracting the parameters.

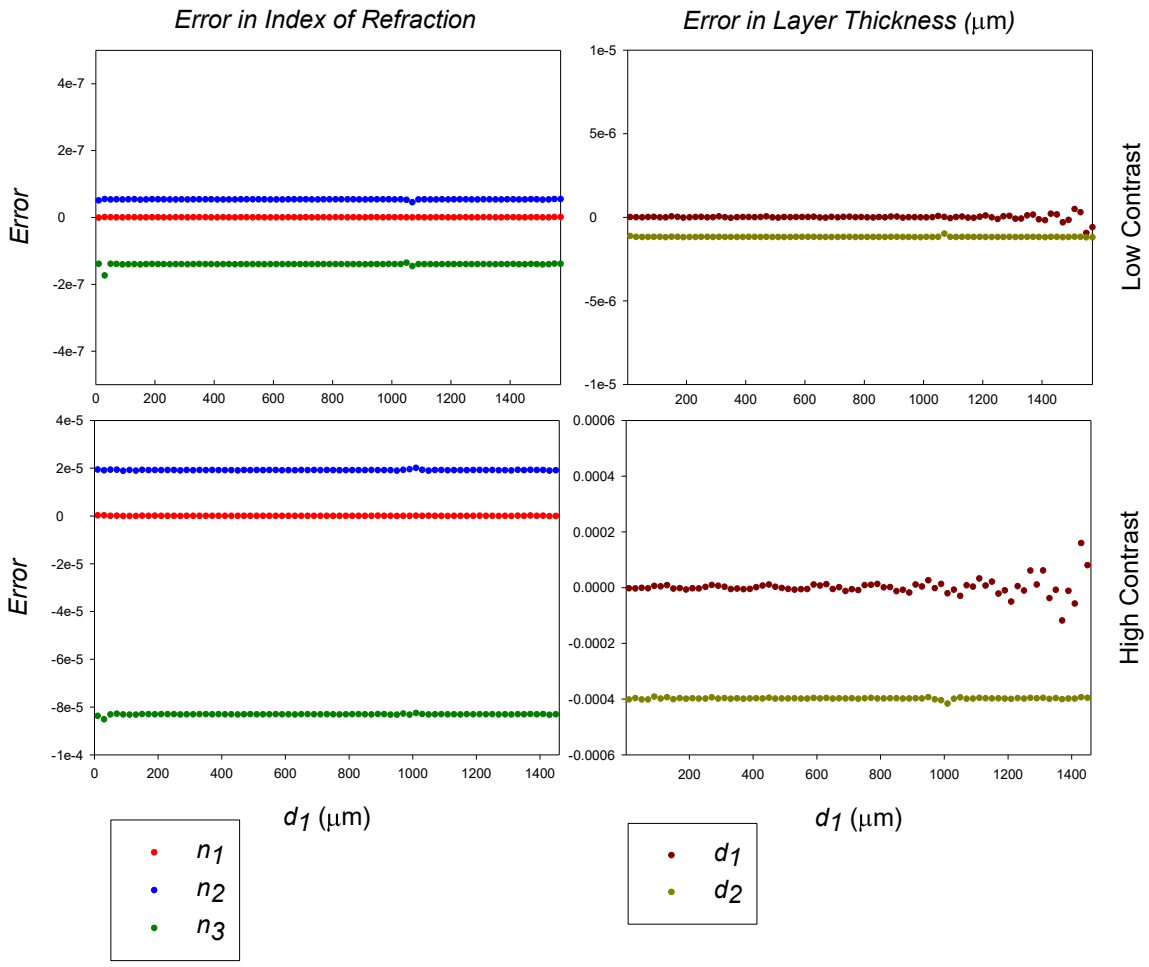

Figure 7.4: Impact of sample thickness on the accuracy of the first optimization method for a fixed $\varepsilon = 0.01$ μm. On the left panes are shown the errors associated with the refractive indices and on the right are shown the errors associated with the thicknesses. Both a low contrast (top) and high contrast (bottom) case are shown.

7.4. The Second Optimization Method

It was shown in section 7.3.1 that when $\varepsilon > 0.045$ μm, the first optimization method produces higher than acceptable error in the parameter extraction. This was mainly due to poor guess values used for the model spectrum and led to improper results. In order to deal with larger values of ε which may occur in practice, we developed the second optimization method. Like the first optimization method, we construct a

model FD-OCT normalized signal similar to Eq(4.8) and Eq(4.9) and fit the model signal to the actual data obtained from digitally constructed TMM. This time the floating parameters to be found are n_1 , $n_2, n_3, \delta_1, \delta_2$. In this method we create an additional step to help refine the measured optical thickness. The fitting process is composed of three steps

Step 1. Search for the optical thickness and index instead of individual index and physical thicknesses since we know that for perfect optical thickness values the matrix equation solution, Eq(4.12) , works well

Step 2. Refine step 1 by searching the optical thickness space around the values obtained in step 1 to locate the true global minimum.

Step 3. Performing the previously described search routine to fit the modeled signal to the actual spectrum and find the optimized parameters.

The modeled signal in the second optimization method is slightly different from the first optimization method given by Eq.(7.1). Since the optical thicknesses are only present in the cosine argument, we can narrow our search for the optical thicknesses by optimizing the frequency components of the spectrum thus reducing the number of parameters to search. In other words, this process first searches for optimized values of the measured optical thickness through the fitting process that gives the correct frequency response in the spectrum. The modeled signal for a two layer system is again similar to Eq(4.8) and Eq(4.9). We introduce the fitting parameters (floating parameters), b_1, b_2, b_3, b_4, b_5 representing for $n_1, n_2, n_3, OT_1, OT_1 + OT_2$ respectively in the modeled signal of the form,

$$g(b,k) =$$

$$\frac{n_0 - b_1}{n_0 + b_1} cos\left(2k\Delta_{rz_0}\right) + \frac{b_1 - b_2}{b_1 + b_2} cos\left[2k\left(\Delta_{rz_0} - b_4\right)\right] + \frac{b_2 - b_3}{b_2 + b_3} cos\left[2k\left(\Delta_{rz_0} - b_5\right)\right]. \quad (7.2)$$

The initial guess values b_1, b_2 , b_3 are used from the extracted parameters n_1, n_2 , n_3 (section 7.1) and b_4 and b_5 from the measured optical thicknesses δ'_1, $\delta'_1 + \delta'_2$. In order to measure OT_1 and $OT_1 + OT_2$ more accurately, and also to prevent the fitting algorithm from stopping at a local minima, the program randomly sweeps δ'_1 and $\delta'_1 + \delta'_2$ within a range around the initial guess values and calculates the root sum of the square differences (RSS) between the model and the TMM spectral responses for each set of OT's to search for the lowest RSS.

Since the algorithm must search for all possible combinations of OT_1 and OT_1+OT_2 within the given interval, step 2 of the algorithm given above, randomly changes b_4 and b_5 and checks the RSS until the minimum RSS is found. The algorithm in this sense is a simple implementation of a Monte Carlo search. The additional step provided in the searching algorithm forces the algorithm to jump over local minima and check for more suitable values; therefore it is more likely to find the best estimate available. This is the advantage of the second optimization method over the first method introduced in section 7.3.

In this optimization method, the step 3 mentioned above, provides the final extracted indices (n_1, n_2, n_3) and optimized optical thicknesses $(OT_1, OT_1 + OT_2)$. The thicknesses then obtained from OT_1/n_1 and $[(OT_1 + OT_2) - OT_1]/n_2$. Therefore the error in d_1 and d_2 can be determined from

$$\frac{\Delta(d_1)}{d_1} = \pm\sqrt{\left[\frac{\Delta(OT_1)}{(OT_1)}\right]^2 + \left(\frac{\Delta n_1}{n_1}\right)^2},$$

$$\frac{\Delta(d_2)}{d_2} = \pm\sqrt{\left[\frac{\Delta(OT_1 + OT_2)}{(OT_1 + OT_2)}\right]^2 + \left[\frac{\Delta(OT_1)}{(OT_1)}\right]^2 + \left(\frac{\Delta n_2}{n_2}\right)^2}. \quad (7.3)$$

As with any Monte Carlo algorithm, the search density (the number of points searched divided by range) is important to ensure finding the global minimum of the RSS. This can be seen in Figure 7.5 where two different search densities were performed on the same 2 layer system, it shows that higher density search provides a better minimum of the RSS and thus a better fit. In this figure the high contrast case given in Table 6.1 with the thicknesses of $d_1 = 10$ μm and $d_2 = 30$ μm with $\varepsilon_{1,2} = +1$ μm for both layers is tested. The top row corresponds to 200 searches for randomly sweeping b_4 and b_5 within 2 μm and 4 μm range of increasing OTs respectively and the bottom row corresponds to 800 searches as for the step 2 mentioned above. From the figure, the minimum RSS achieved by 200 searches is 0.0016 whereas by 800 searches the minimum RSS is 3.3926×10^{-5}. The latter case indicates a better fit between the spectral signal and the modeled signal and thus better extracted parameters. For the majority tests in this chapter 800 searches has been used. For testing the optically thin models (section 7.6) only 100 searches were required for good parameter extraction, for testing the noisy systems (sections 7.5) 1000 searches and for three layer system (section 7.7) 1500 searches was used.

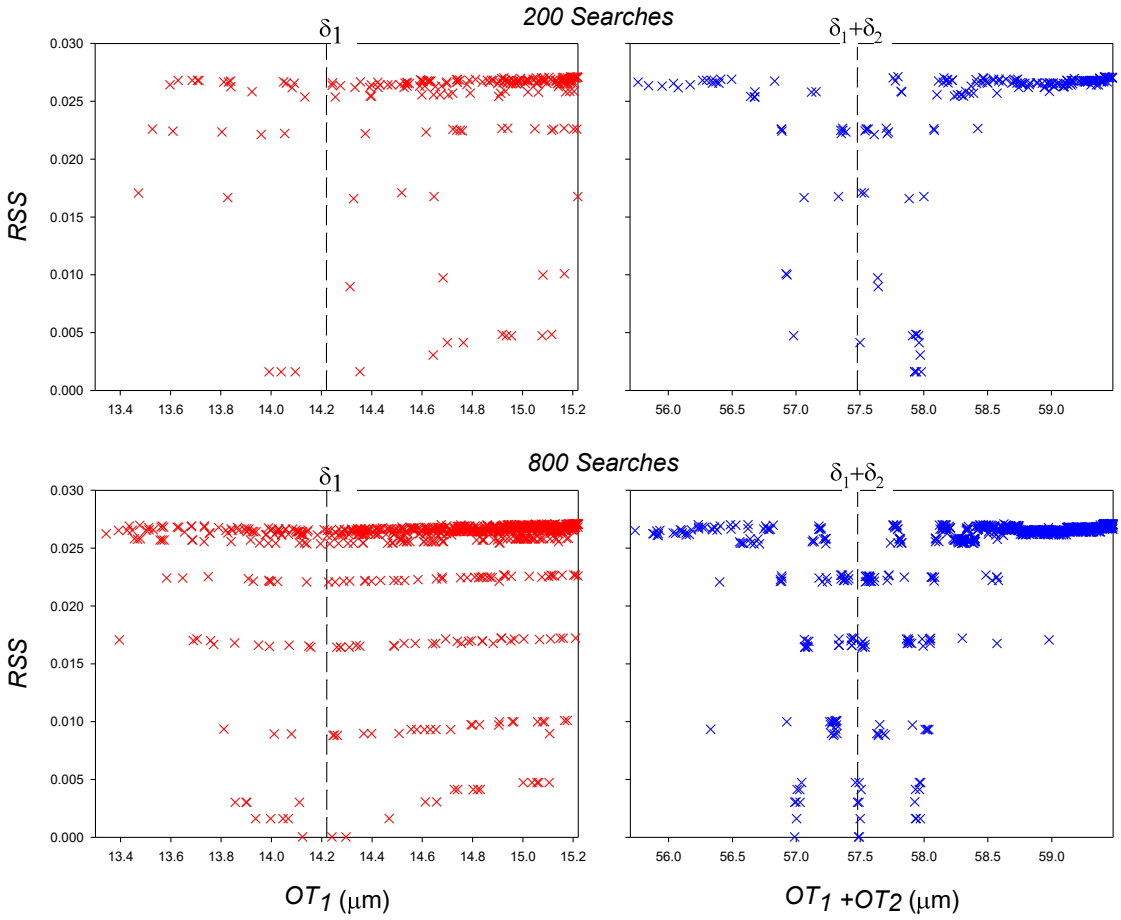

Figure 7.5: The effect of the number of searches on finding the minimum of the RSS for a high contrast case. The top row corresponds to 200 searches and the bottom row corresponds to 800 searches. The dashed lines indicate true optical thicknesses.

The last thing to be discussed about the second optimization method is the testing of the correctness of the result when we force the modeled signal based on summation method (ignores multiple reflections), to be fitted with TMM signal (accounts for multiple reflections). One possible way to check the correctness of the result is to generate a digitalized signal based on the summation method, ignoring multiple reflections, and fit the modeled signal to it. Since both signals ignore multiple reflections, they must perfectly fit to each other and thus the parameters

should be extracted with zero error. In order to do this test, we generated an FD-OCT signal using summation the method instead of TMM and tested the low contrast case given in Table 6.1 when the thicknesses are $d_1 = 10$ μm and $d_2 = 30$ μm for range of ε between $\varepsilon_{1,2} = 0$ to $\varepsilon_{1,2} = +1$ μm with 0.05 μm increment and 100 number of searches. The test result is shown in Figure 7.6 where the deviation of the fitting parameters $\{b_i\}$ from their true values $\{n_i, d_i\}$ (vertical axis) versus ε (horizontal axis) is plotted. On the left panes are shown the errors in the index of refraction and on the right are shown the errors in the thicknesses. It can be seen that all the parameters have been extracted with zero error showing that the second optimization works correctly and that behavior we see later on are not the result of computational issues.

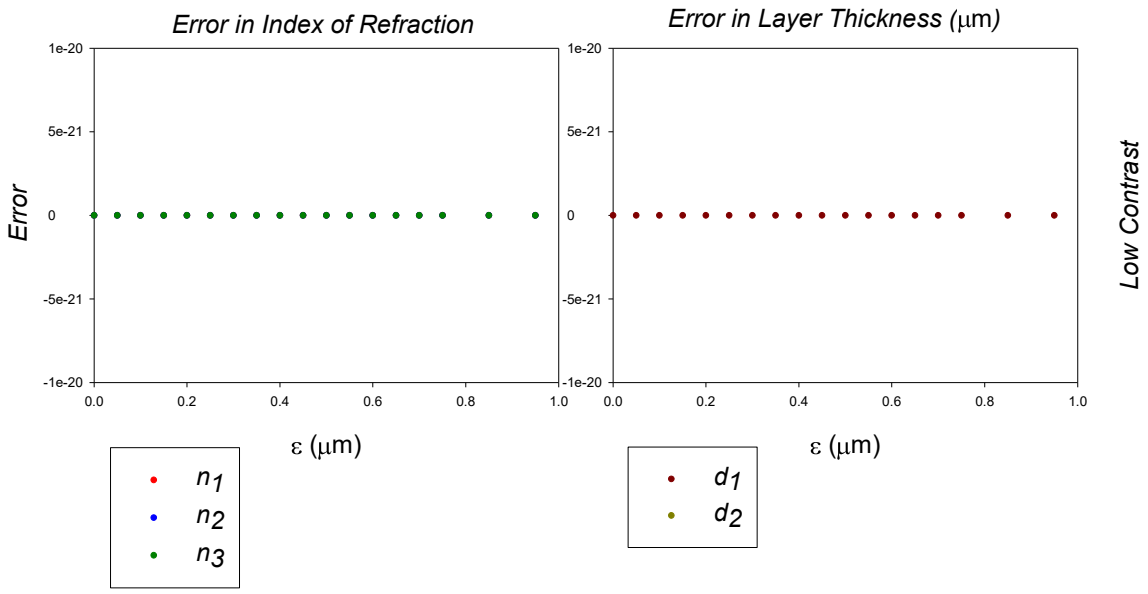

Figure 7.7: the test for the second optimization method when the FD-OCT signal is generated using summation method (ignoring multiple reflections). On the left panes are shown the error of the index of refraction and on the right are shown the errors in the thicknesses.

7.4.1. The Second Optimization Method for a Range of ε

We are now going to investigate the second optimization method for a range of ε and see if this method can help us to extract parameters correctly with larger values of ε compared to the limited range in the first optimization method. It was described in the previous section that the number of searches plays an important role to extract the parameters correctly. To illustrate the behavior of the extracted parameters error of the second optimization method with respect to the number of searches and estimate the required number of searches, we recall the test models with low and high contrast given in Table 6.1 with thicknesses $d_1 = 10$ μm and $d_2 = 30$ μm. For both layers, ε is swept between $\varepsilon_{1,2} = 0$ to $\varepsilon_{1,2} = +10$ μm in 0.4 μm increment. The simulation program was asked to increase the number of searches until all indices n_1, n_2, n_3 are found with error less than 0.001, a reasonable error for biological applications. The results are shown in Figure 7.8. In the left pane of this figure is shown the extracted parameters errors and on the right pane is shown the estimated number of searches required versus ε on the horizontal axis. The error in this figure is the deviation of the fitting parameters $\{b_1, b_2, b_3\}$ from their true values $\{n_1, n_2, n_3\}$.

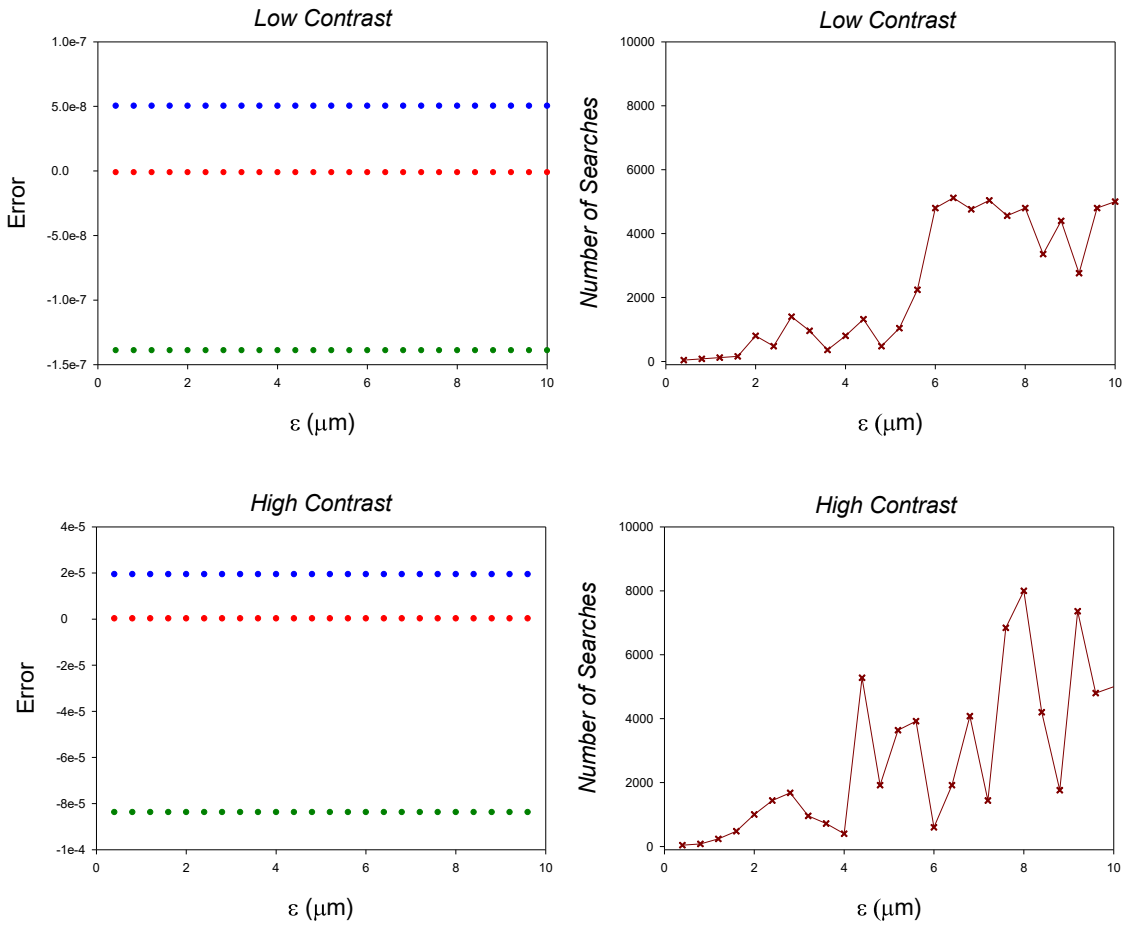

Figure 7.8: Impact of the number of searches on the accuracy of the extracted indices by the second optimization method. On the left panes are shown the error of the extracted index of refraction and on the right are shown the required number of searches. Both the low contrast (top) and high contract (bottom) case are shown.

It can be seen from Figure 7.8 that once we have enough number of searches, the system can find all indices for very large amount of ε, there is convergence to highly accurate refractive index values. For a limited number of searches the range of ε for which we can extract parameters with acceptable error, is limited. To illustrate the behaviour of the extracted parameters error of the second optimization method with limited number of searches, we recall the above test models with low and high contrast given in Table 6.1 when the thicknesses are $d_1 = 10$ μm and $d_2 = 30$ μm.

For both layers, ε is swept between $\varepsilon_{1,2} = 0$ to $\varepsilon_{1,2} = +3$ μm with 0.06 μm increment with fixed number of searches to 800 searches. The test results are shown on Figure 7.9. In this figure, the deviation of the fitting parameters $\{b_i\}$ from their true values $\{n_i, d_i\}$ on the vertical axis is plotted versus ε on the horizontal axis. On the left panes are shown the errors in the index of refraction and on the right are shown the errors in the thicknesses. Both the low contrast (top) and high contract (bottom) case are shown. The figure shows that the second optimization method extends the acceptable range of ε to ~1.00 μm or more as compared to a few nanometers in Figure 7.1 and 0.04 μm in Figure 7.2 for the first optimization method. Also the quality of the results in region $\varepsilon < 1.00$ m are comparable to the results obtained in Figure 6.4 for the low and high contrast cases with $\varepsilon = 0$.

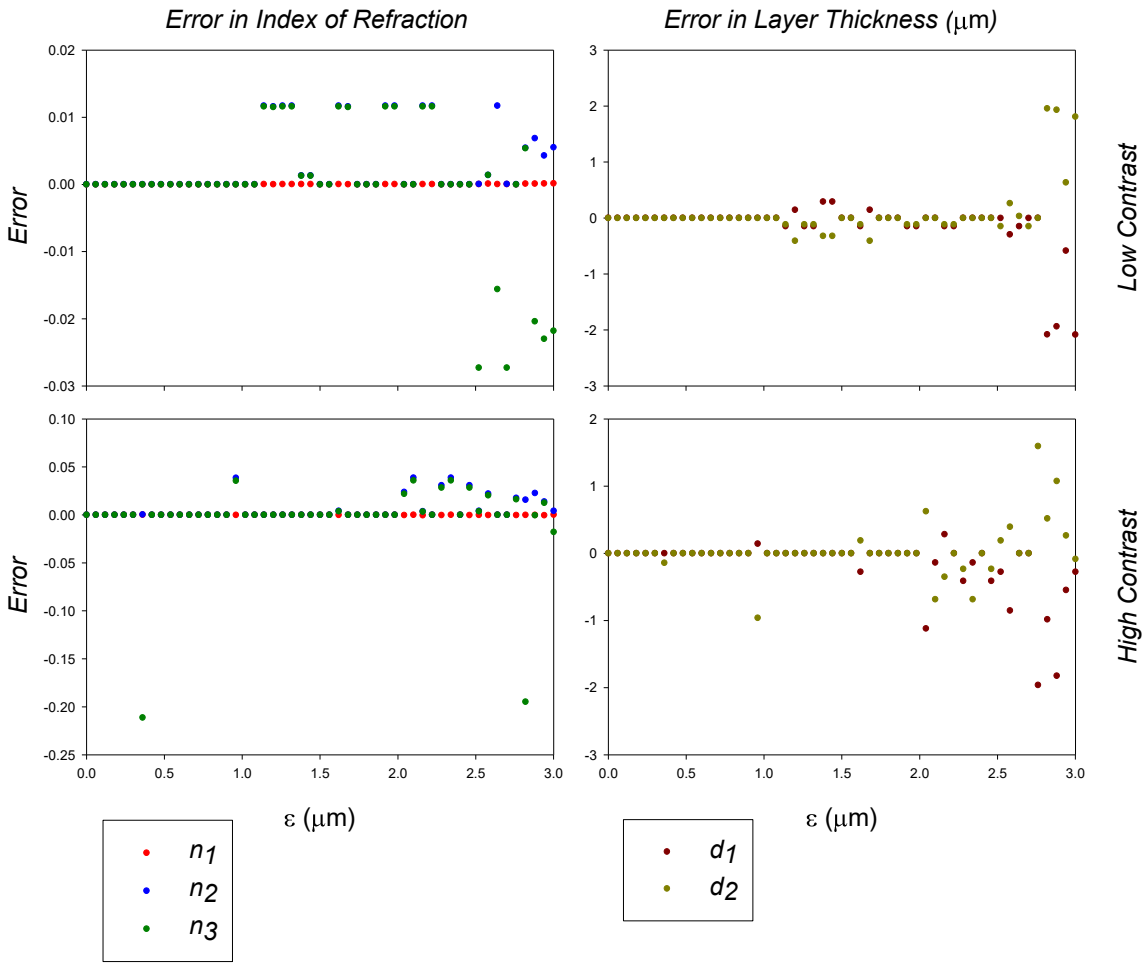

Figure 7.9: Impact of the optical thickness measurement errors, ε, on the accuracy of the second optimization method with fixed number of searches. On the left panes are shown the error of the index of refraction and on the right are shown the errors in the thicknesses. Both the low contrast (top) and high contract (bottom) case are shown.

The error in n_1, n_2, n_3 on the left pane of Figure 7.9 for the range of $\varepsilon \leq 1$ μm, is on average within the order of $\sim 10^{-9}$, $\sim 10^{-8}$ and $\sim 10^{-7}$ respectively for the low contrast case and $\sim 10^{-7}$, $\sim 10^{-5}$ and 10^{-5} respectively for the high contrast case. The error of d_1 and d_2 are also almost constant within $\sim 10^{-9}$ and $\sim 10^{-6}$ respectively for the low contrast case and $\sim 10^{-6}$ and $\sim 10^{-4}$ for the high contrast

case for the range of $\varepsilon \leq 1$ μm. The increase in error for high contrast cases was expected due to the increasing multiple reflections described in section 4.4.1. Also the result for high contrast case is 10-fold better than the stable region of the first optimization method (Figure 7.3) for both index and thickness.

It is worth noting that since the second optimized method randomly change OT_1 and $OT_1 + OT_2$ and check the RSS at each search, sometimes the global minimum of RSS is missed. This is due to the stochastic nature of the second optimization approach, a simple implementation of a Monte Carlo search. An example of this situation can be seen on the bottom row of Figure 7.9 for the high contrast case where there is one outlier pints in region ≤ 1 μm. The odd point corresponds to situation where the global minimum of RSS was not found by the search algorithm. For the outliers, if we re-run the program and increase the number of searches, the program does converge to the correct solution that represents a global minimum. This implies that there is no physical restriction for the outlier. We may conclude that the algorithm is typically well behaved, but that there exists situations where convergence may not be found due to the stochastic nature of the search.

7.4.2. The Second Optimization Method for a Range of Thickness

The ability of the second optimization to extract parameters across a range of thickness is investigated and is shown in Figure 7.11. In this test, ε is fixed at the relatively large value of $\varepsilon_{1,2} = 1.00$ μm for the both layers. This value of ε is almost the same size as one imaging cell. Both the low and the high contrast cases noted in Table 6.1 are shown in Figure 7.10 and Figure 7.11, corresponding to varying d_2 and varying d_1, respectively. In Figure 7.10 the thickness of the first layer is fixed at 30

μm and the thickness of the second layer varies from 10 μm up to the maximum detectable range of the simulation system (2.18 mm in total optical thickness noted in Table 5.1) in 30 μm increments. For the low contrast case this range is up to 1580 μm and for the high contrast case 1480 μm. The situation is reversed in Figure 7.11 where the thickness of the second layer is fixed at 30 μm and the thickness of the first layer varies from 10 μm up to the maximum detectable range of the simulation system (1570 μm for the low contrast and 1490 μm for the high contrast case). The lower limit of the varying thickness is chosen according to Figure 5.6 to be close to the stable region of optical thickness measurement. The vertical axis in Figure 7.10 and Figure 7.11 is the error of the extracted parameters and the horizontal axis is the varying thickness. In these figures, on the left panes are shown the errors in the index of refraction and on the right are shown the relative errors in the thicknesses ($\Delta d_{1,2}/d_{1,2}$). Both the low contrast (top) and high contract (bottom) case are shown.

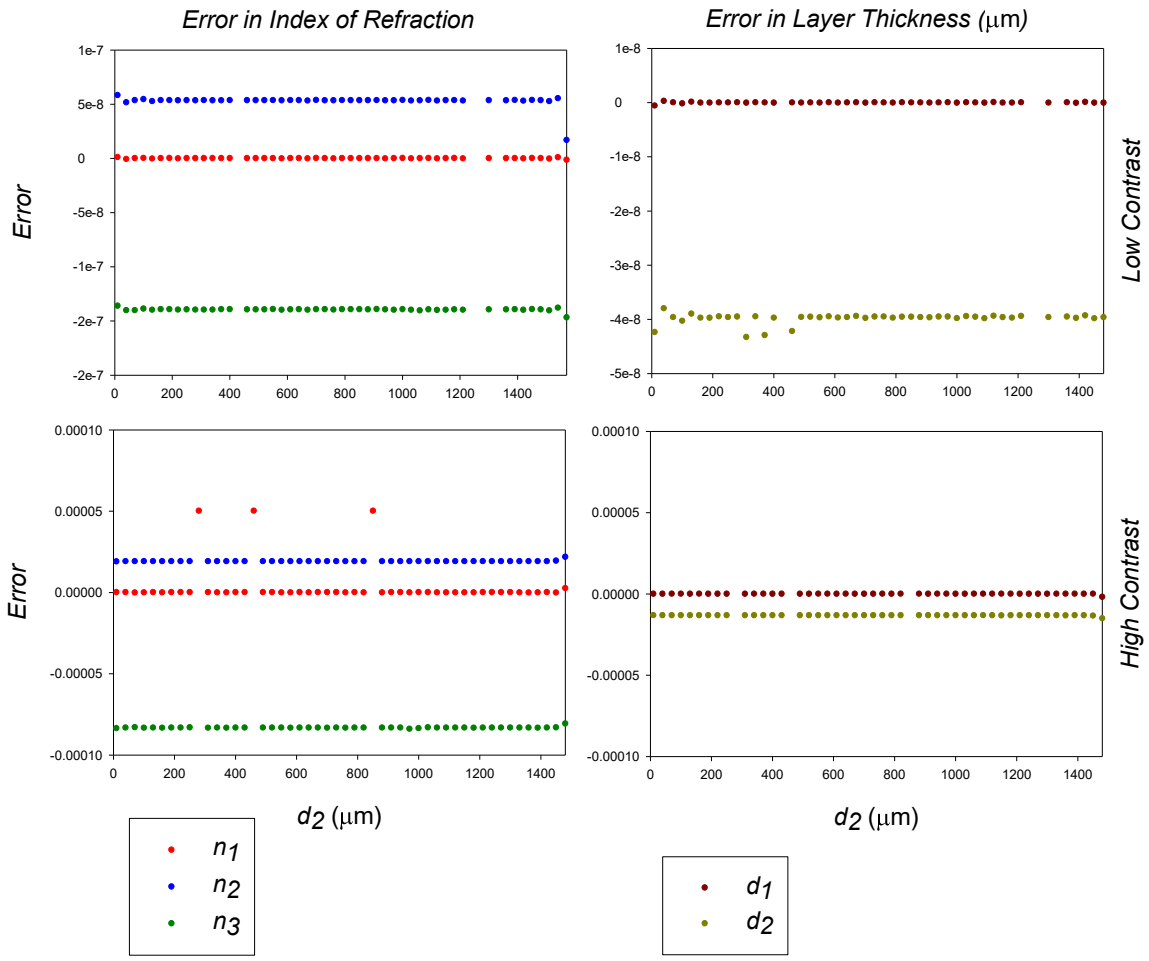

Figure 7.10: Impact of sample thickness (varying d_2) on the accuracy of the second optimization method for a fixed $\varepsilon = 1.00$ μm. On the left panes are shown the errors associated with the refractive indices and on the right are shown the relative errors associated with the thicknesses. Both a low contrast (top) and high contrast (bottom) case are shown. The errors are almost insensitive to the layer's thickness.

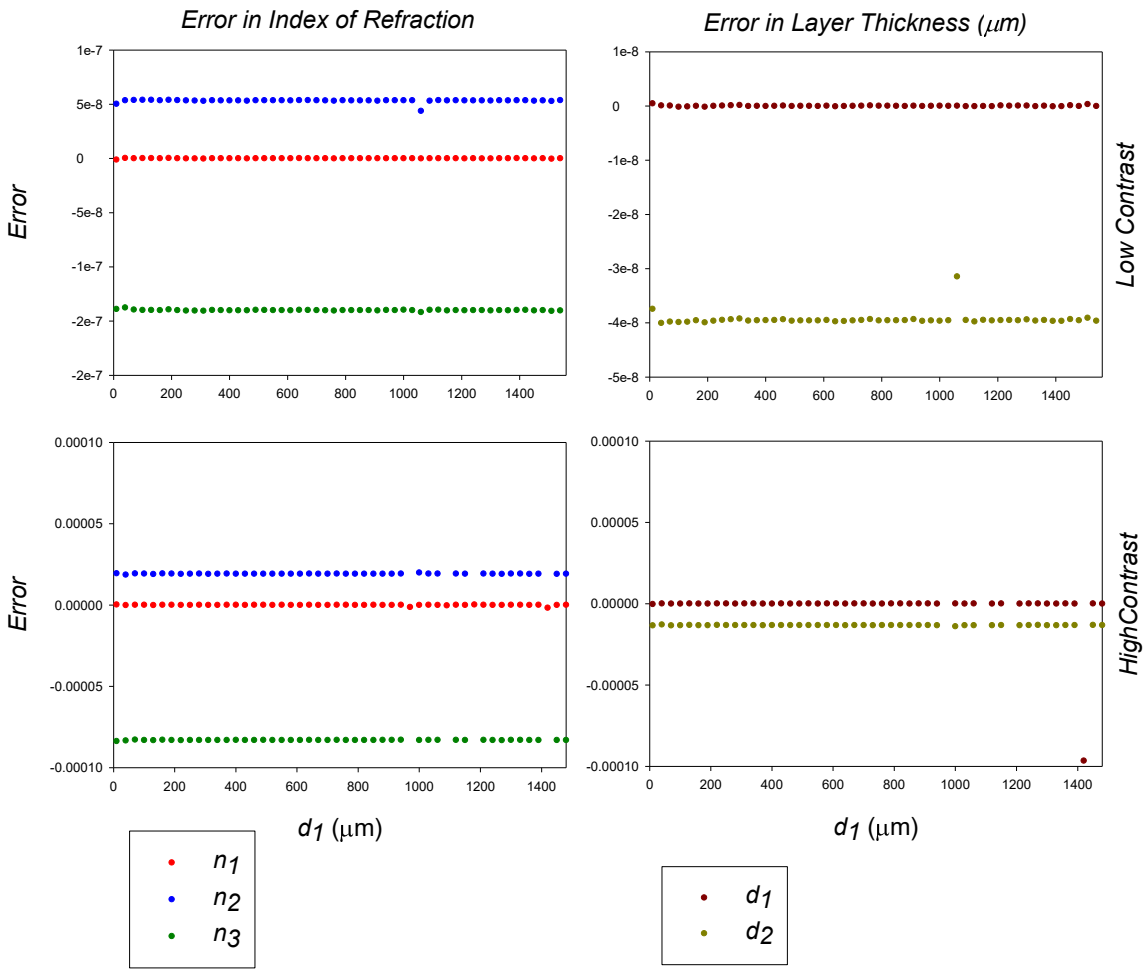

Figure 7.11: Impact of sample thickness (varying d_1) on the accuracy of the second optimization method for a fixed $\varepsilon = 1.00$ μm. On the left panes are shown the errors associated with the refractive indices and on the right are shown the relative errors associated with the thicknesses. Both a low contrast (top) and high contrast (bottom) case are shown. The errors are almost insensitive to the layer's thickness.

It is seen from the left panes of Figure 7.10 and Figure 7.11 that error in the extracted index from the second optimization method is almost insensitive to the layer thicknesses. The indices error are the same for varying d_2 or d_1 showing that for indices extraction, there is no difference if $d_2 > d_1$ or $d_2 < d_1$. It is also seen that errors are generally higher in magnitude for the high contrast case as expected due

to the increased amplitude in multiple reflections (section 4.4.1). The error of indices in Figure 7.10 and Figure 7.11, for n_1, n_2 and n_3 on the left pane are on average of the order of $\sim 10^{-11}$, $\sim 10^{-8}$ and $\sim 10^{-7}$ respectively for the low contrast case and of the order of $\sim 10^{-8}$, $\sim 10^{-5}$ and $\sim 10^{-5}$ respectively for the high contrast case. Also the thickness errors are the same when varying d_2 or d_1 showing that for there is no difference if $d_2 > d_1$ or $d_2 < d_1$.

From Figure 7.10 and Figure 7.11, the relative error of d_1 for the low and high contrast cases, excluding the outliers points, is on average $\sim 10^{-11}$ and $\sim 10^{-8}$. The magnitude of the errors is the same as the order of errors in n_1 mentioned above which indicates that OT_1 has been extracted with almost zero error. The relative error of d_2 for the low and high contrast cases is $\sim 10^{-8}$ and $\sim 10^{-5}$. The order of errors is the same as the order of errors in n_2 mentioned above which indicates that OT_2 has been extracted with almost zero error. The investigation reported in this section shows that the extracted parameter errors are independent of the thickness profile of the object.

7.4.3. Index Contrasts

In this section we investigate the impact of refractive index profile on errors in the parameters extracted by the second optimization method in the presence of optical measurement error of $\varepsilon_{1,2} = +1.00$ μm for both layers. Two models with fixed layer thicknesses and varying indices are tested. The first test model is optically thick (with respect to the source coherence length) with thicknesses $d_1 = 10$ μm, $d_2 = 30$ μm and the second model is optically very thick with thicknesses $d_1 = 500$ μm, $d_2 = 300$ μm. The indices range begins with the surrounding medium index

of refraction, 1.337 for biological application, the index of an aqueous medium. The upper ranges are limited by the simulation system, as the point in Figure 5.8 above which the system cannot determine the number of layers correctly. The tests with varying n_1, n_2 and n_3 are presented in Figure 7.12, Figure 7.14 and Figure 7.16 respectively. Both the thick and very thick cases are shown on the top and bottom rows of the figures. On the left panes are shown the error of the index of refraction and on the right are shown the errors in the thicknesses.

The impact of the first layer index contrast on the error of the extracted parameters is shown on Figure 7.12. The vertical axis in this figure corresponds to the parameter errors and the horizontal axis corresponds to n_1 which is ranged between 1.337 and 1.9 in 0.015 increments while the other indices are $n_2 = 1.351$ and $n_3 = 1.337$. The first data point for both the thick and very thick cases on Figure 7.12 was out of the range since at this point the index of the first layer is the same as the front medium and so this layer has not been detected by the simulation system. This point has been omitted from the figure. The figure shows that the second optimization method extracts n_1 and d_1 for the whole range of n_1 with very small amount of error. The variation of error of n_1 is difficult to be seen from Figure 7.12, so it is plotted separately on Figure 7.13 for both the thick and very thick cases.

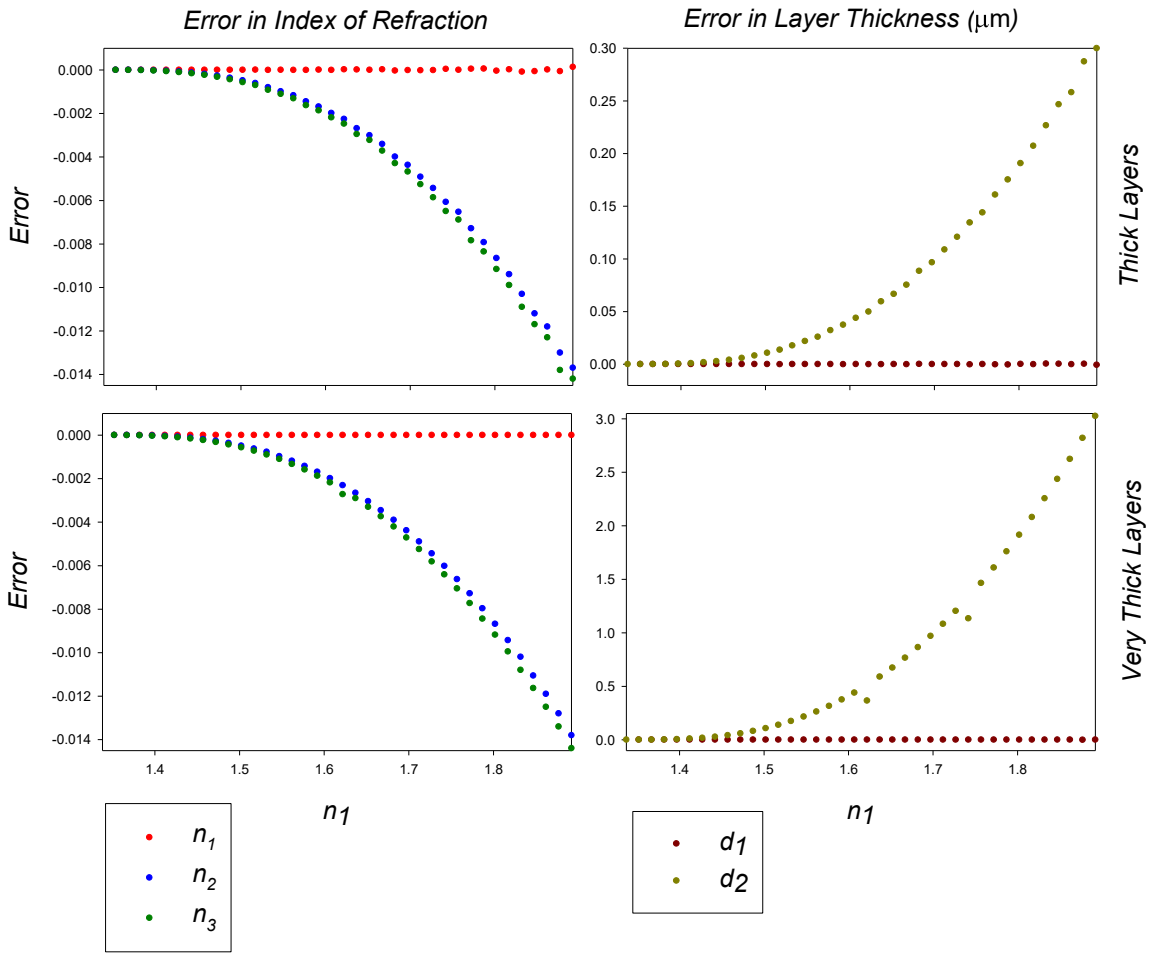

Figure 7.12: Impact of sample index contrast (varying n_1) on the accuracy of the second optimization method when ε=1.00 μm. On the left panes are shown the errors in the index of refraction and on the right are shown the error in the thickness. Both the thick (top) and very thick (bottom) cases are shown. In this figure $n_2 = 1.351$ and $n_3 = 1.337$.

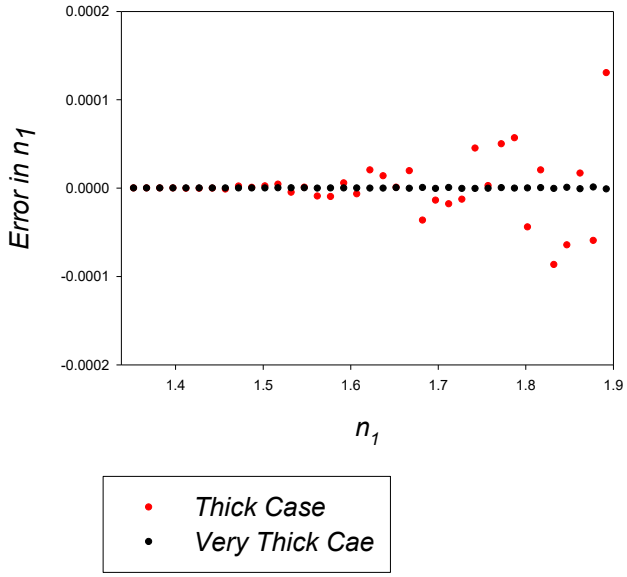

Figure 7.13: Variation in error for n_1 corresponding to Figure 7.12 for both the thick and very thick cases. The error behaves more stable for the very thick case than the thick case.

As it can be seen from Figure 7.13, the variation of error for the very thick case is more stable than the thick case. The error corresponding to n_1 increases from $\sim 10^{-10}$ to $\sim 10^{-4}$ as n_1 increases for the thick case and from $\sim 10^{-12}$ to $\sim 10^{-6}$ for the very thick case. So generally the error increases with the contrast as we expected but it is rather insignificant for n_1. The reason for extracting n_1 highly accurate can be explain from the modeled signal Eq(7.2) where on the first term on the right hand side, n_0 is assumed to be known and thus it facilitates the searching program for finding n_1 and thence d_1 with better accuracy than the other parameters. This advantage does not exist for the n_2 and n_3 and thus d_2 so the error propagates to them.

It is also seen from Figure 7.12 that the error of n_2 and n_3 increases with increasing n_1. In other words the error of n_2 and n_3 depend on their contrast with respect to n_1. This behavior is independent from the thickness since the error in n_2 and n_3 are the same for both the thick and very thick cases Figure 7.12. For any given value of n_1, we cannot extract n_2 and n_3 with better accuracy than what is shown on Figure 7.12[6].

Since d_1 and d_2 are extracted from $OT_{1,2}/n_{1,2}$, their error are directly related to the error in n_1 and n_2 and $\varepsilon_{1,2}$ respectively from Eq(6.1) while their relative error ($\Delta d_{1,2}/d_{1,2}$) remain unchanged for the thick and very thick cases on the right pane of Figure 7.12. The error corresponding to d_1 cannot be seen clearly from the figure, increases from $\sim 10^{-8}$ to $\sim 10^{-4}$ as n_1 increases for the thick case and from $\sim 10^{-12}$ to $\sim 10^{-6}$ for the very thick case.

The impact of the second layer index contrast on the accuracy of the extracted parameters is illustrated in Figure 7.14. The vertical axis corresponds to errors in parameters and the horizontal axis corresponds to n_2 which is ranged between 1.337 and 1.9 in 0.015 increments while the other indices are $n_1 = 1.345$ and $n_3 = 1.337$. From Figure 7.14 the difference in errors corresponding to n_1 and n_2 is difficult to see, so they are plotted separately in Figure 7.15. The error corresponding to n_1 varies between the order of $\sim 10^{-11}$ to $\sim 10^{-5}$ for the thick case and from $\sim 10^{-12}$ to $\sim 10^{-5}$ for the very thick case as n_2 increases. It can be seen from Figure 7.15 A, that error for the very thick case is more stable than for the thick case.

[6] It will be also shown later on Figure 7.14 that the error of n_3 remains the same for varying n_2 as it is for varying n_1.

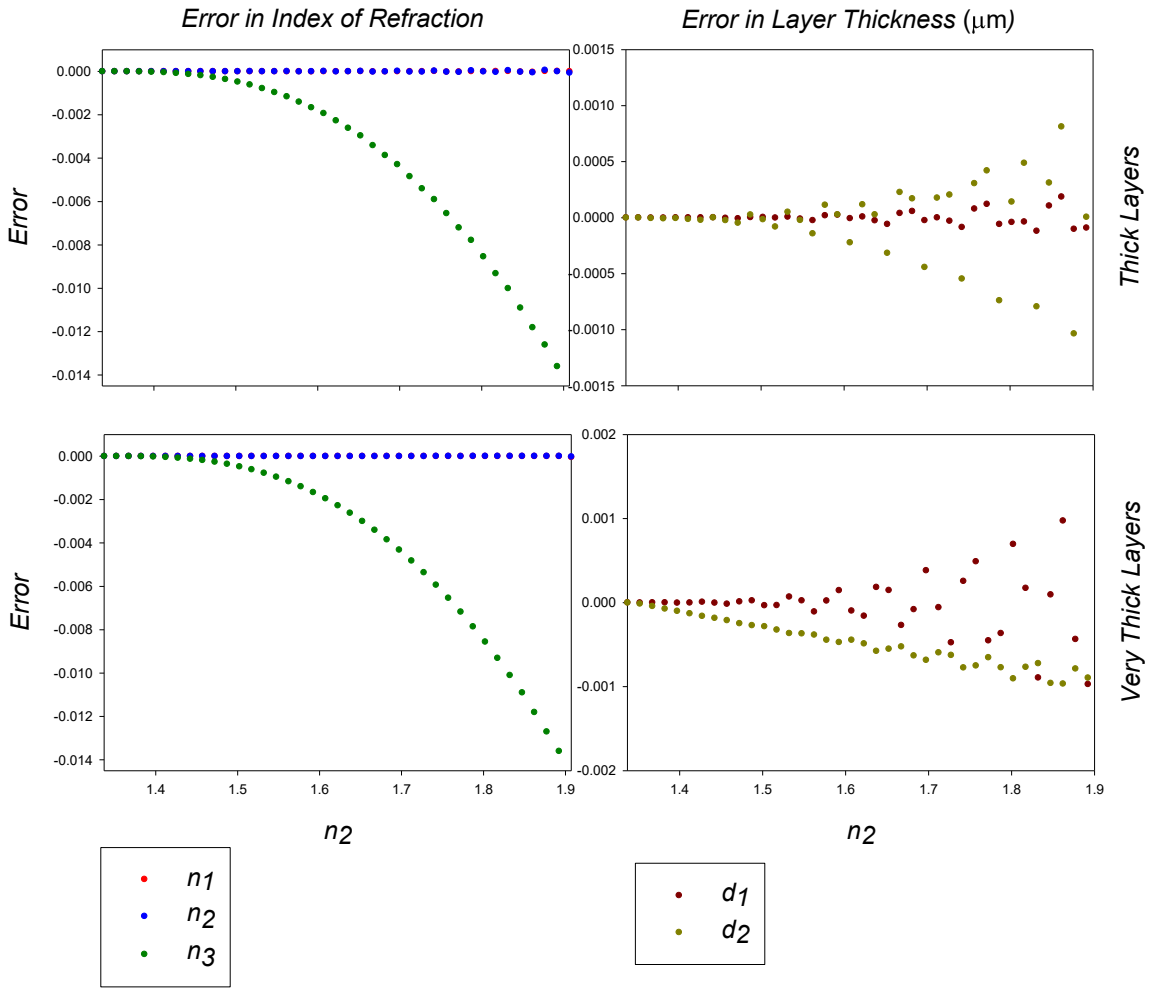

Figure 7.14: Impact of sample index contrast (varying n_2) on the accuracy of the second optimization approach when ε=1.00 μm. The the left panes show the errors in the calculation of the index of refraction and on the right are shown the errors in the calculation of the thicknesses. Both a thin (top) and thick (bottom) case are shown. In this figure $n_1 = 1.345$ and $n_3 = 1.337$.

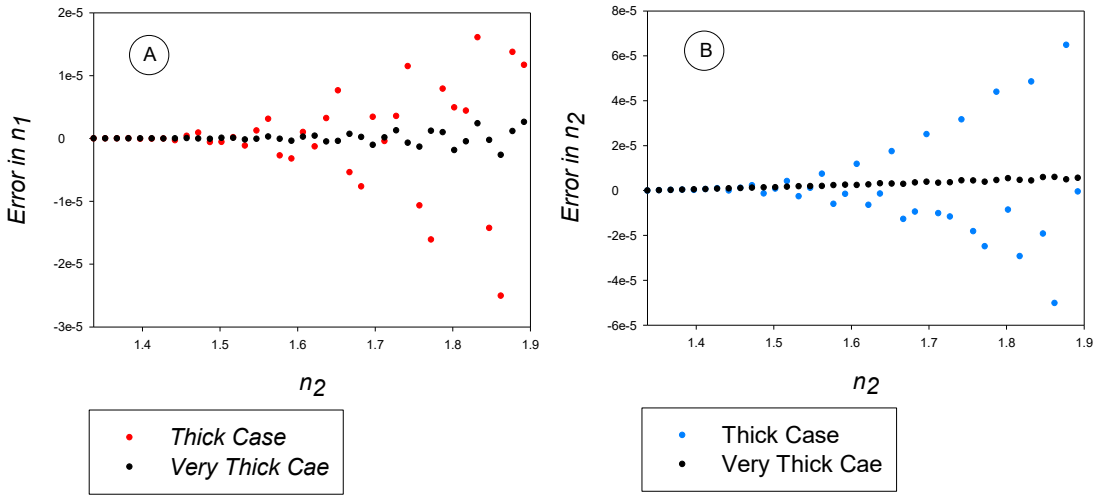

Figure 7.15: Variation in error corresponding to A) n_1 and B) n_2 of Figure 7.14 for both the thick and very thick cases.

For the error of n_2, from Figure 7.15 B for the fixed value on n_1, the error of n_2 also increases with increasing n_2. The increase in error of n_2 can be seen from Figure 7.15 B, is rather insignificant while it is more stable for the very thick case than the thick case. The error in n_2 varies between $\sim 10^{-8}$ to $\sim 10^{-5}$ for the thick case and $\sim 10^{-8}$ to $\sim 10^{-6}$ for the very thick case. From the previous discussion of Figure 7.12, the error of n_2 also depends on its contrast with respect to n_1. The errors corresponding to d_1 and d_2 are related to the errors in $n_1$and n_2 respectively, Eq(6.1). For the error in n_3 it can be seen from Figure 7.14 that the error increases with increasing n_2 with the same values for both the thick and very thick cases. The error in n_3 in Figure 7.14 and in Figure 7.12 is the same so we may conclude that the error of n_3 depends on the contrast of $n_1$and n_2 in the same manner.

The impact of the third layer index contrast on the accuracy of the extracted parameters is illustrated in Figure 7.16. The vertical axis corresponds to the errors in the extracted parameters and the horizontal axis corresponds to n_3 which is ranged between 1.337 and 2.1 in 0.015 increments while the other indices are $n_1 = 1.345$ and $n_2 = 1.351$. In Figure 7.16 the differences in errors corresponding to n_1 and n_2 are small and difficult to see, so they are plotted separately at higher magnification in Figure 7.17 . It can be seen from Figure 7.17 that increasing n_3 has slight impact on the error in n_1 and n_2. The error in n_1 ranged from $\sim 10^{-11}$ to $\sim 10^{-7}$ for the thick case and from $\sim 10^{-11}$ to $\sim 10^{-8}$ for the very thick case. The error in n_2 ranged from $\sim 10^{-8}$ to $\sim 10^{-6}$ for the thick case and stays around $\sim 10^{-8}$ for the very thick case. The error of d_1 and d_2 on the right pane of Figure 7.16 thus follows the behaviour of errors in n_1 and n_2. The error of n_3 is increases from $\sim 10^{-8}$ to $\sim 10^{-5}$ for both the thick and very thick cases with the slope of $\sim 1.75 \times 10^{-5}$.

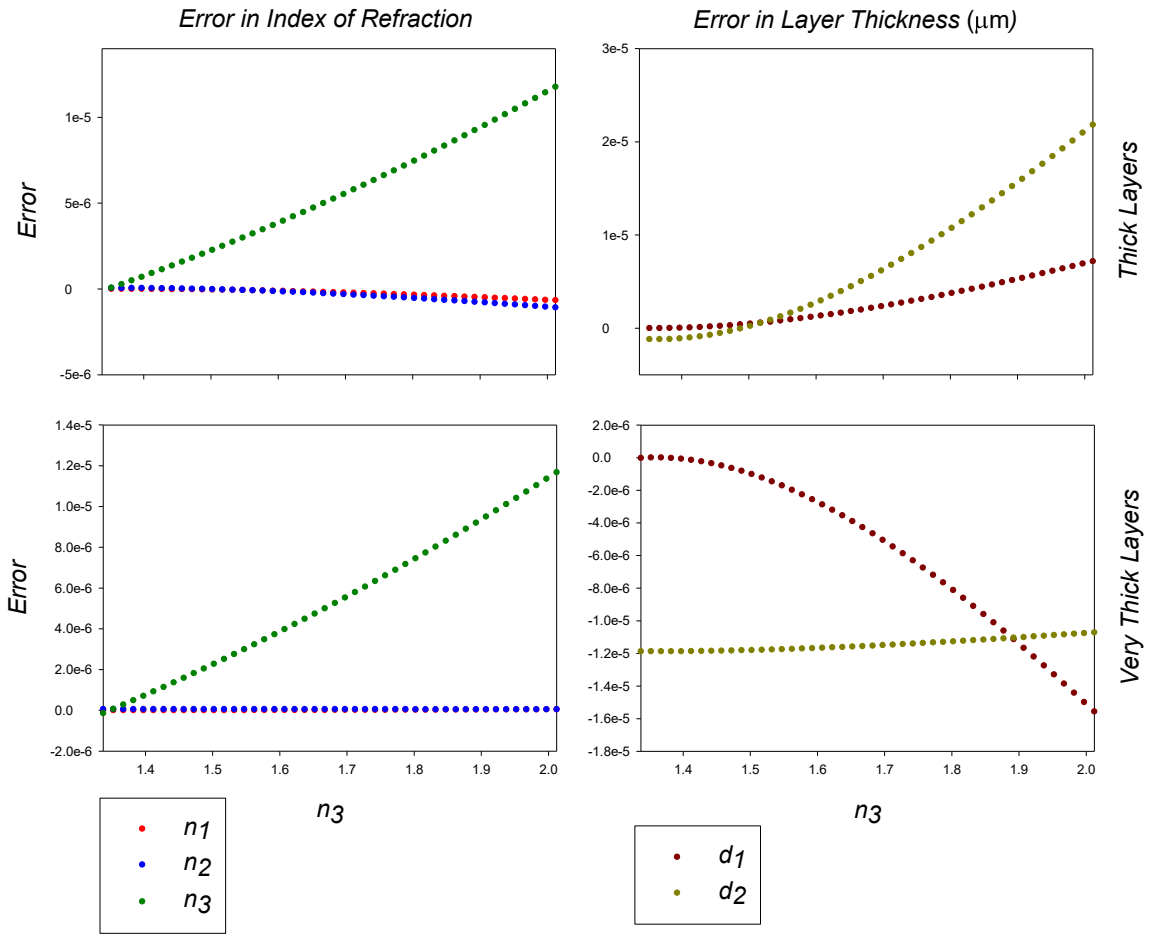

Figure 7.16: Impact of sample index contrast (varying n_3) on the accuracy of the second optimization approach when ε=1.00 μm. The left panes show the errors in the calculation of the index of refraction and on the right are shown the errors in the calculation of the thicknesses. Both a thin (top) and thick (bottom) case are shown. In this figure $n_1 = 1.345$ and $n_2 = 1.351$.

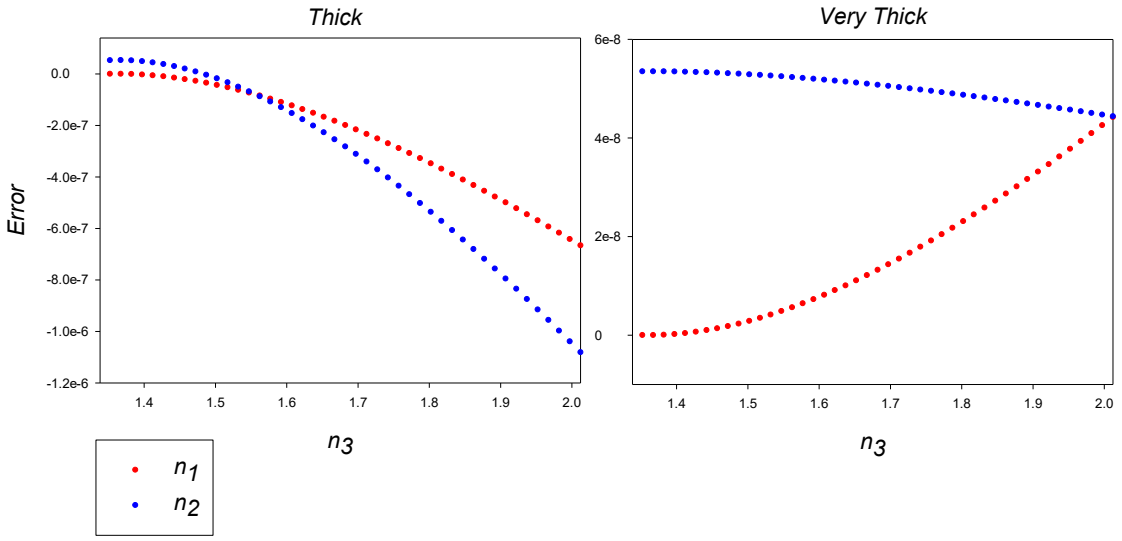

Figure 7.17: The error of n_1 and n_2 for the range of n_3 corresponding to Figure 7.16.

From the test results illustrated in Figure 7.12 to Figure 7.16 we can have a rough estimate of the range of the parameters error with respect to each index value when other indices are constant. The same pattern for the parameters error was obtained with $\varepsilon = 0.1, 0.2,$ and 0.5 μm which shows that the parameters error with repect to indices is independent from ε in that range of OT errors. In order to have a better estimate of error distribution with respect to index contrast in general, we need to explore a broad range of possible contrast. From Figure 7.16 it is seen that increasing n_3 does not have much impact on the error on other parameters. Therefore a parameters error distribution map is provided for models with n_1 and n_2 varying from 1.337 to 1.9 in 0.011 increments while $n_3 = 1.337$ but must still be extracted by the software. Both thicknesses are set to 30 μm and ε is set to 0.1 μm. A total number of 2600 test models were tested. In the following figures (Figure 7.18 to Figure 7.21), the horizontal axis corresponds to actual n_1 and the vertical axis corresponds to actual n_2, the color map is the extracted parameters error without

any optimization on the top pane and after performing the second optimization method on bottom pane.

The error distribution corresponding to the extracted n_1 is shown in Figure 7.18. It can be seen from the bottom pane of the figure that n_1 can be extracted by the second optimization method with error of ± 0.001 and better, suitable for biological applications, in the entire n_1 and n_2 space tested. This is also consistent with the test results in Figure 7.12 and Figure 7.14. The error distribution in n_1 on the bottom pane of Figure 7.18 should be compared to the top pane which shows that the second optimization method improves greatly the usefulness of this solution. Without optimization, the error in extracted n_1 varies between -1.40 to $+0.70$.

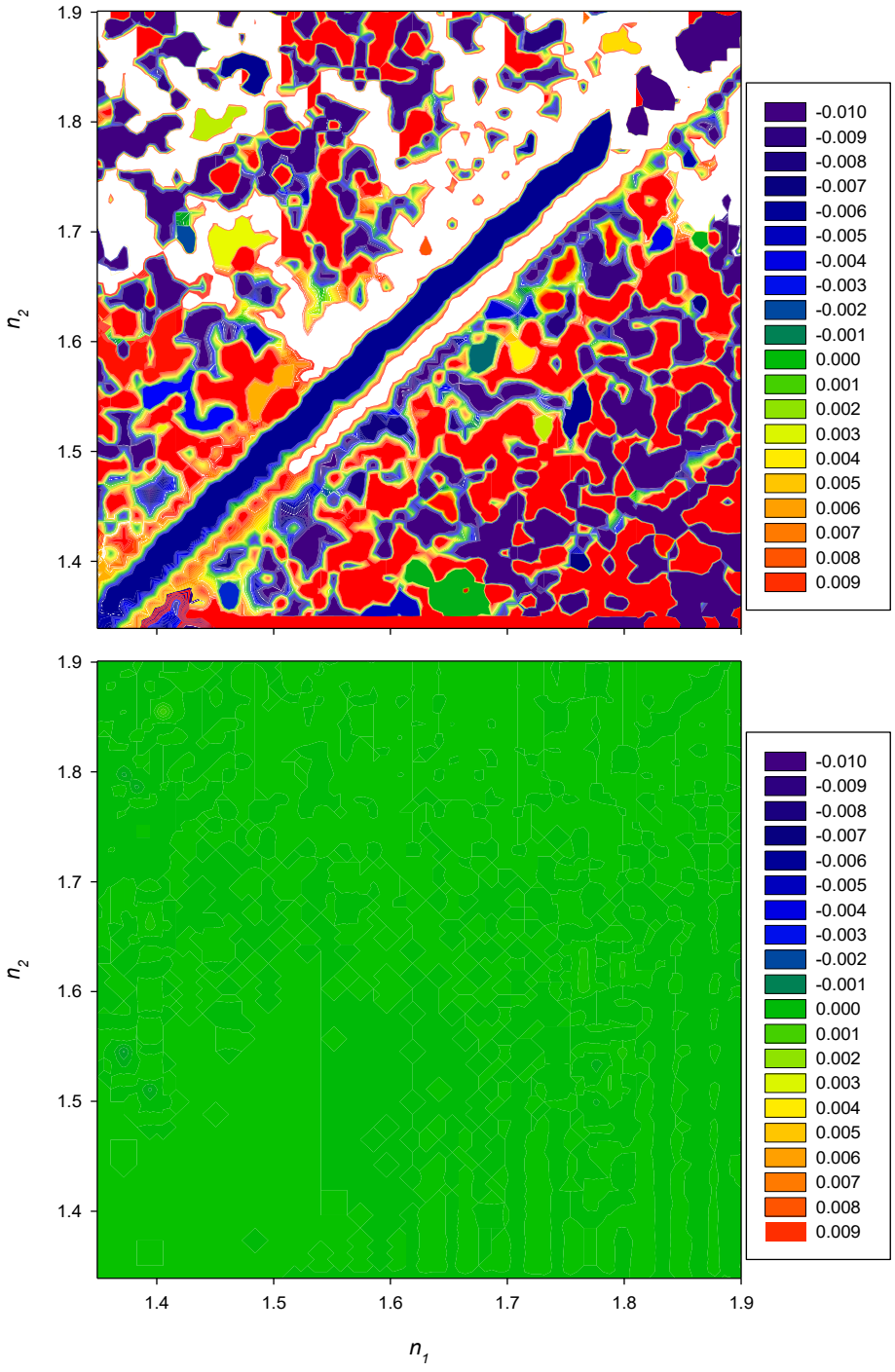

Figure 7.18: The contour map corresponding to error distribution of the extracted n_1 with $\varepsilon = 0.1$ μm. The horizontal axis corresponds to varying n_1 and the vertical axis corresponds to varying n_2. On the top pane is shown the extracted n_1 without optimization and on the bottom pane is shown the result from the second optimization method.

The error distribution corresponding to the extracted n_2 is shown in Figure 7.19. It can be seen from the bottom pane of the figure that n_2 can be extracted by the second optimization method with error of ± 0.001 or better in an area limited by $n_1 < 1.55$ and $n_2 < 1.90$. This is also consistent with the test result in Figure 7.14. The improvement that is achieved by the second optimization should be compared to the top pane of Figure 7.19 where the error in n_2 varies between -1.88 to $+0.67$. The irregularities on the top right of the figure corresponds to models that their optical thicknesses could not be determined correctly.

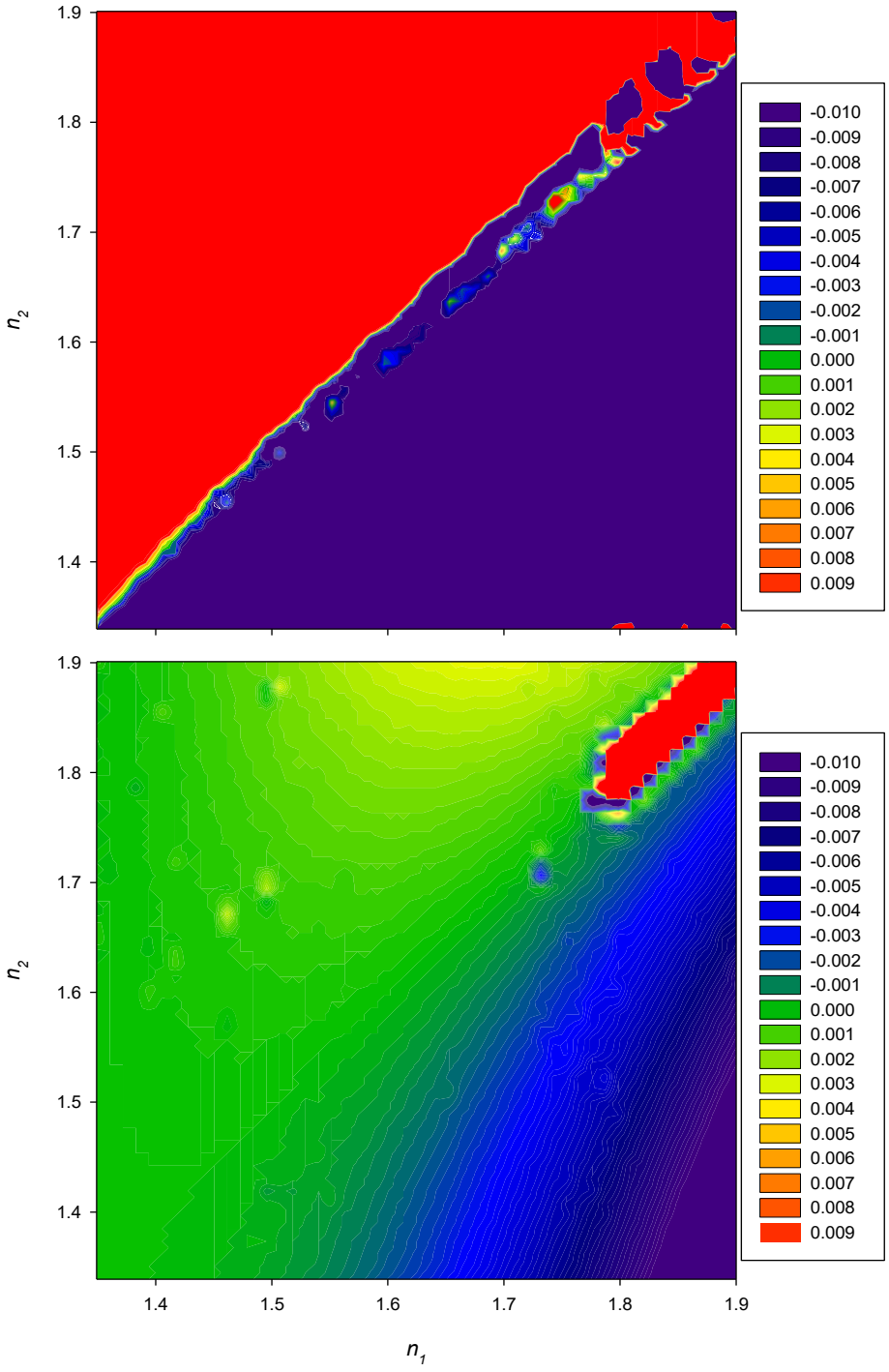

Figure 7.19: The contour map corresponding to the error distribution of the extracted n_2 with $\varepsilon = 0.1$ μm. The horizontal axis corresponds to varying n_1 and the vertical axis corresponds to varying n_2. On the top pane is shown the extracted n_2 without optimization and on the bottom pane is shown the result from the second optimization method.

The error distribution corresponding to the extracted n_3 is shown in Figure 7.20. It can be seen from the bottom pane of the figure that n_3 can be extracted by the second optimization method with error of ± 0.001 or better in area limited by $n_1 < 1.55$ and $n_2 < 1.6$. The improvement that is done by the second optimization should be compared to the top pane of Figure 7.20 where the error in n_3 varies between -1.17 to -0.02 and never reaches the targeted 0.001 accuracy. The irregularities on the top right of the figure corresponds to models that their optical thicknesses could not be determined correctly.

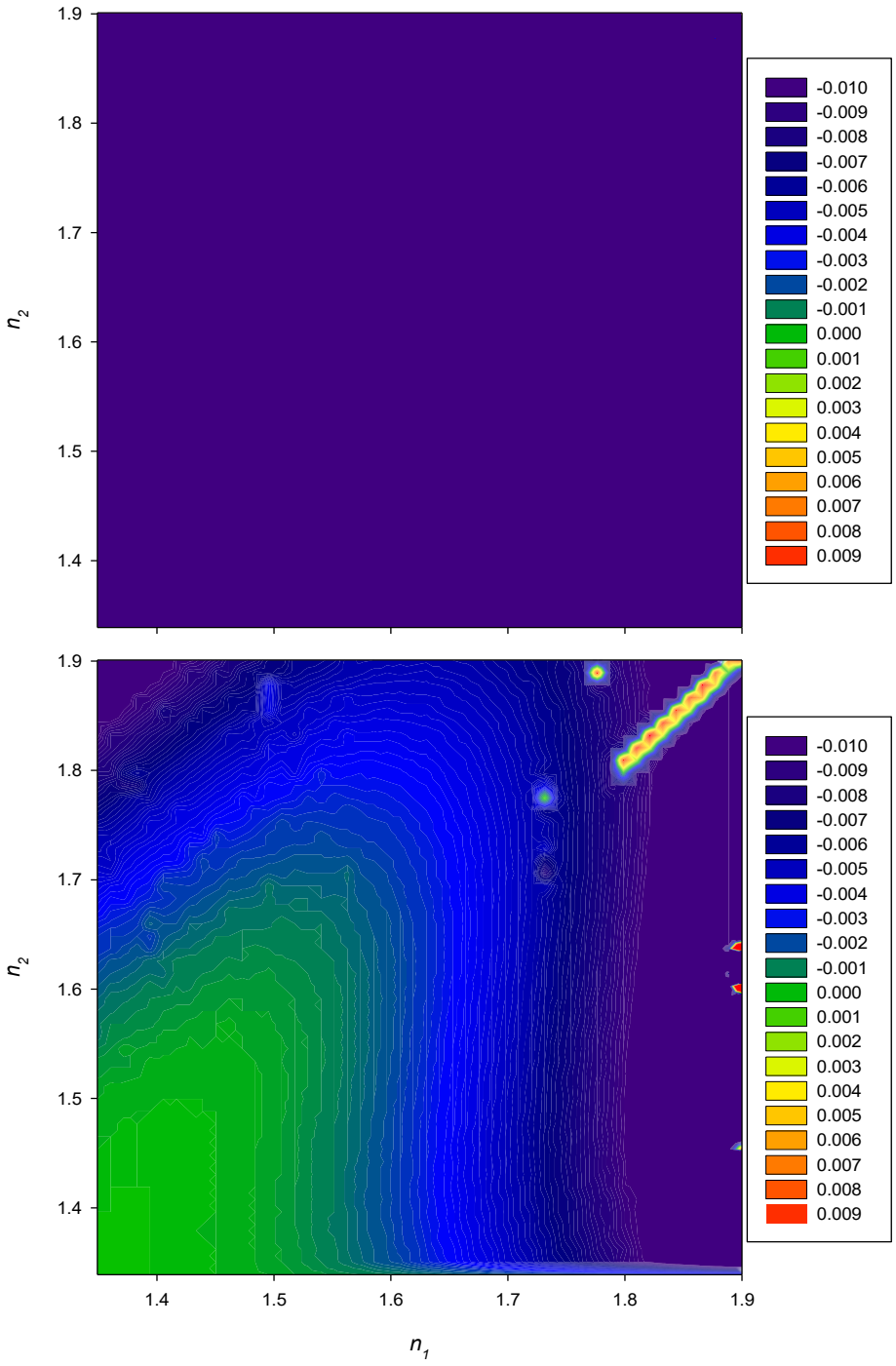

Figure 7.20: The contour map corresponding to error distribution of the extracted n_3 with $\varepsilon = 0.1$ μm. The horizontal axis corresponds to varying n_1 and the vertical axis corresponds to varying n_2. On the top pane is shown the extracted n_3 without optimization and on the bottom pane is shown the result from the second optimization method.

The relative error distribution corresponding to the extracted thicknesses by the second optimization method is shown in Figure 7.21. On the left pane is shown the relative error in d_1 and on the right pane is shown the relative error in d_2. Like the previous figures, the irregularities on the top right and the narrow band on the bottom of the right pane correspond to models with incorrectly determined optical thicknesses. The relative error in $d_{1,2}$ follows the error pattern of the corresponding indices $n_{1,2}$. It can be seen from the left pane of Figure 7.21 that the relative error in d_1 is within ± 0.001 for almost all cases whereas for d_2 is limited to the region with $n_1 < 1.55$.

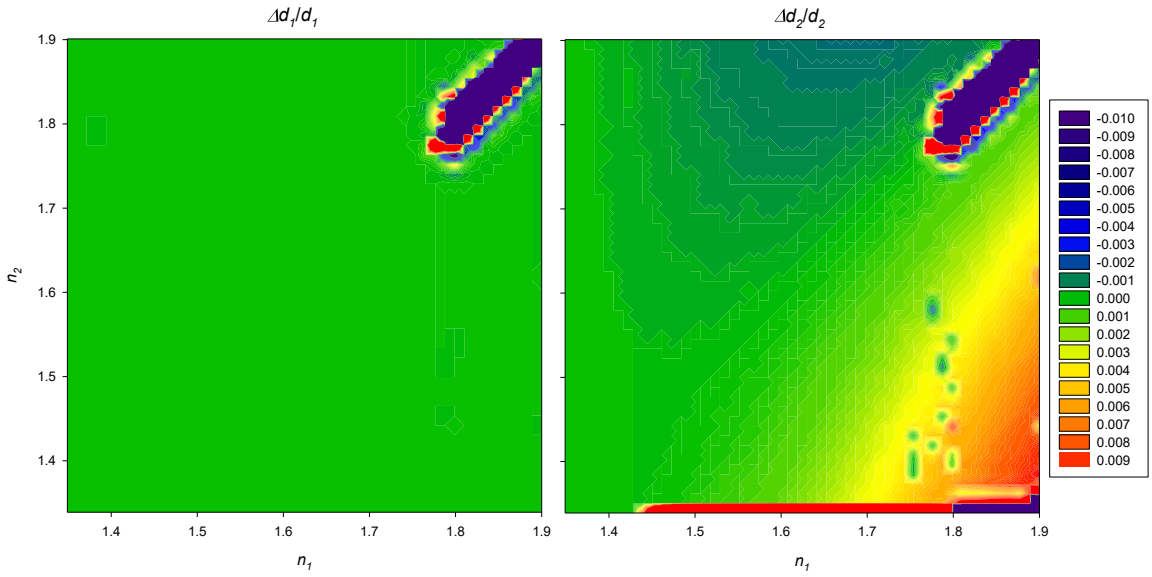

Figure 7.21: The contour map corresponding to relative error distribution of the extracted thicknesses from the second optimization method with $\varepsilon = 0.1$ μm. The horizontal axis corresponds to varying n_1 and the vertical axis corresponds to varying n_2. The left pane corresponds to the relative error in d_1 and the right pane corresponds to the relative error in d_2.

In conclusion, if we are looking for extracting the refractive index parameters of a two layer system with error within the range of ± 0.001, suitable for biological applications, the second optimization method can be used to achieve this accuracy for the full parameter space explored. From the bottom pane of Figure 7.18, n_1 can be extracted with the above accuracy for the whole range of the given contrast. n_2 can be extracted for cases with $n_1 < 1.55$ and $n_2 < 1.90$ and n_3 can be extracted for $n_1 < 1.55$ and $n_2 < 1.6$.

7.4.4. The Effect of Non-zero Mismatch Arm's Length

To investigate the behaviour of the second optimization method in the presence of non-zero mismatch arm's length, we recall the test models with low and high contrast given in Table 6.1 when the thicknesses are $d_1 = 10$ μm and $d_2 = 30$ μm. ε is swept between $\varepsilon_{1,2} \approx 0$ to $\varepsilon_{1,2} = +1$ μm in 0.01 μm increment for both layers. The mismatch arm's length is set to $\Delta_{rz_0} = 10$ μm and the test results are shown on Figure 7.22. In this figure the errors in the extracted parameters are shown on the vertical axes and they are plotted versus ε on the horizontal axis. The left panes show the errors in the index of refraction and on the right are shown the errors in the thicknesses. Both a low contrast (top) and high contract (bottom) case are shown. Figure 7.22 is almost the exact replica of Figure 7.9 where $\Delta_{rz_0} = 0$. Like Figure 7.9, the errors in the indices are higher for the high contrast case as expected due to increase in the amplitude of the multiple reflections. We may conclude that the mismatch arm's length has no effect on parameter extraction. Some data points in Figure 7.22 seemed to be missed. As described in section 7.4.1, the missing points

correspond to situation where the global minimum of RSS was not found by the search algorithm because of sampling density and the stochastic nature of the process . For the outliers, if we re-run the program and increase the number of searches, the program does converge to the correct solution that represents a global minimum. Therefore there is no physical restriction for the missed data points.

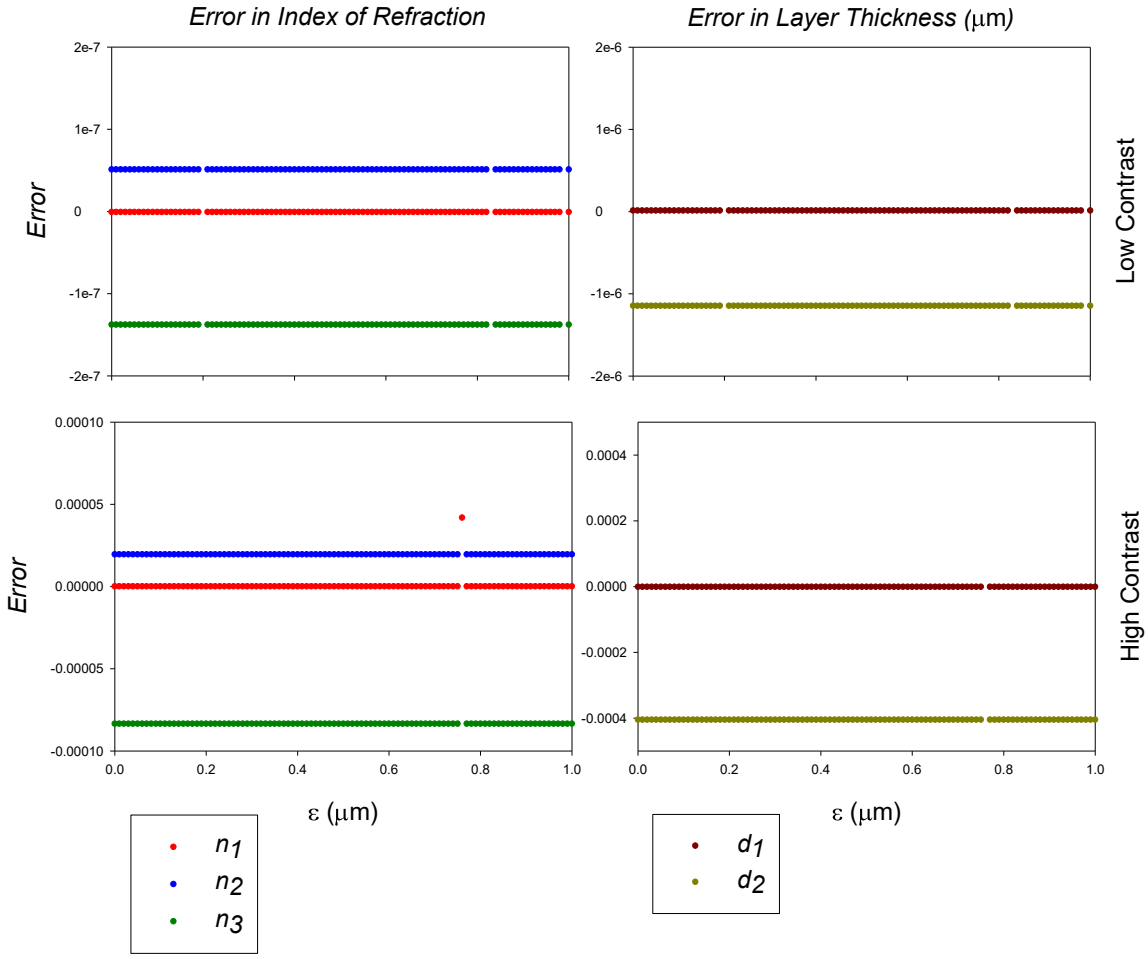

Figure 7.22: Impact of mismatch arm's length (Δ_{rz_0} = 10 μm) on the accuracy of the second optimization approach. The left panes show the errors in calculation of the indices and on the right are shown the errors in the calculation of the thicknesses. Both a low contrast (top) and high contract (bottom) case are shown.

7.5. The Effect of White Noise

The next step is to look at the more realistic case where the spectrum contains noise. In this test we will add different level of noise to the spectral response. Only white noise is considered here. This noise is generated using the Mathcad "rnorm" function. This function generates random numbers having the normal distribution with zero mean value and the standard deviation as 1. The random value generated by "rnorm" function is multiplied by the noise percentage times the absolute maximum value of the normalized signal. This noisy spectral response used in the same way as described in chapter 6 and earlier in chapter 7 to extract the parameters. The noisy signal for two different level of noise is shown in Figure 7.23 where the normalized signal (correspond to the high contrast case) is plotted versus the wavenumber.

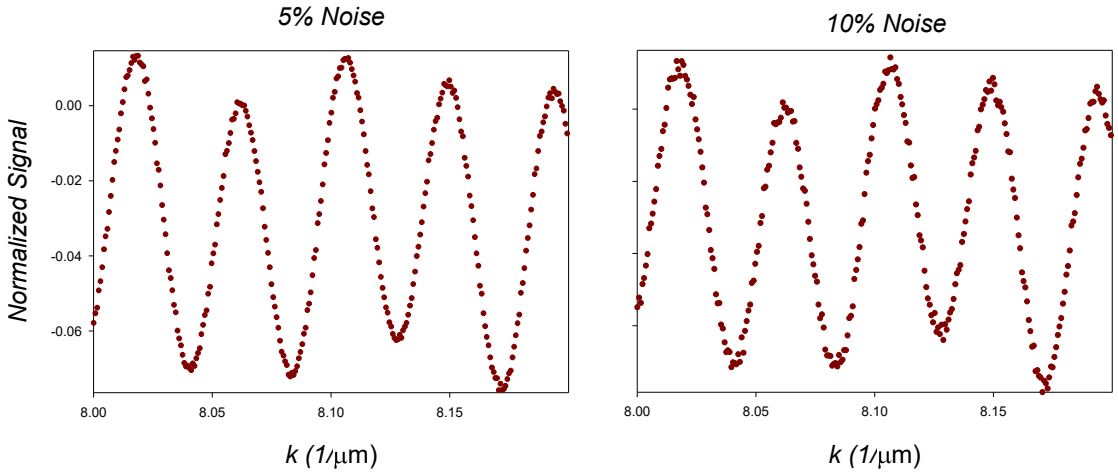

Figure 7.23: the effect of white noise on the normalized signal for noise level of 5% (left) and 10% (right) of the signal's maximum value. Only a portion of the spectrum is shown.

We illustrate the impact of white noise on the error of the extracted parameters (n_1, n_2, n_3, d_1, d_2) for the two test models given in Table 6.1 (low and high contrast models) when the thicknesses are $d_1 = 10$ μm and $d_2 = 30$ μm (optically thick) and when $d_1 = 500$ μm and $d_2 = 300$ μm (optically very thick). This time ε is fixed at $\varepsilon_{1,2} = +0.1$ μm and the number of searches for the tests in this section is set to 100 searches. The level of noise is varied from 0% to 100% with unit increments.

The test result for the low contrast and high contrast cases are shown in Figure 7.24 and Figure 7.25 respectively. In these figures, the top row corresponds to the optically thick layers and the bottom row corresponds to the optically very thick. The vertical axis is the deviation of the fitted parameters $\{b_i\}$ from their true values $\{n_i, d_i\}$ and the horizontal axis is the noise level in percentage. The right pane shows the error of index and left pane shows the error of thickness.

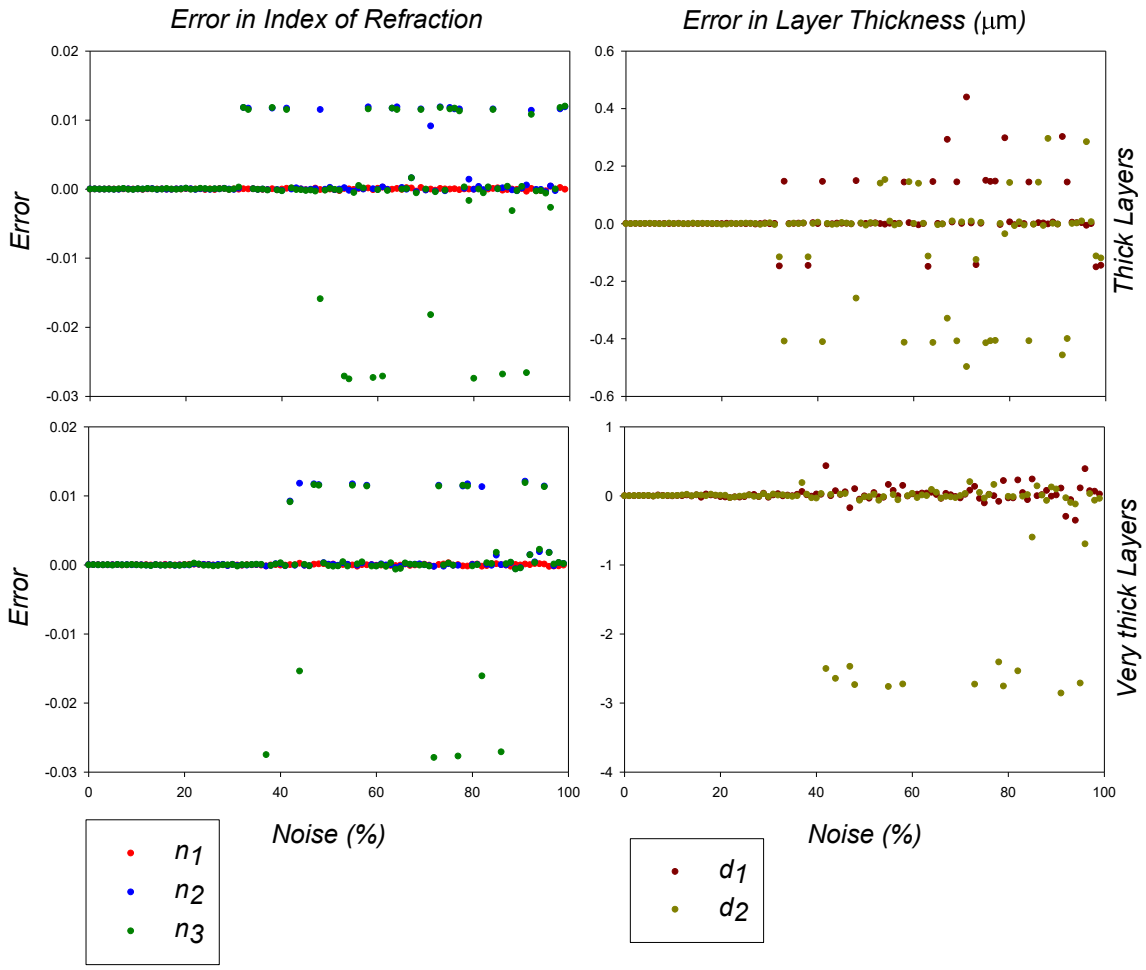

Figure 7.24: Impact of white noise on the accuracy of the second optimization method for the low contrast case. The left panes shows the error in the extracted index of refraction and on the right are shown the errors of the extracted thicknesses. Both a thick (top) and very thick (bottom) case are shown.

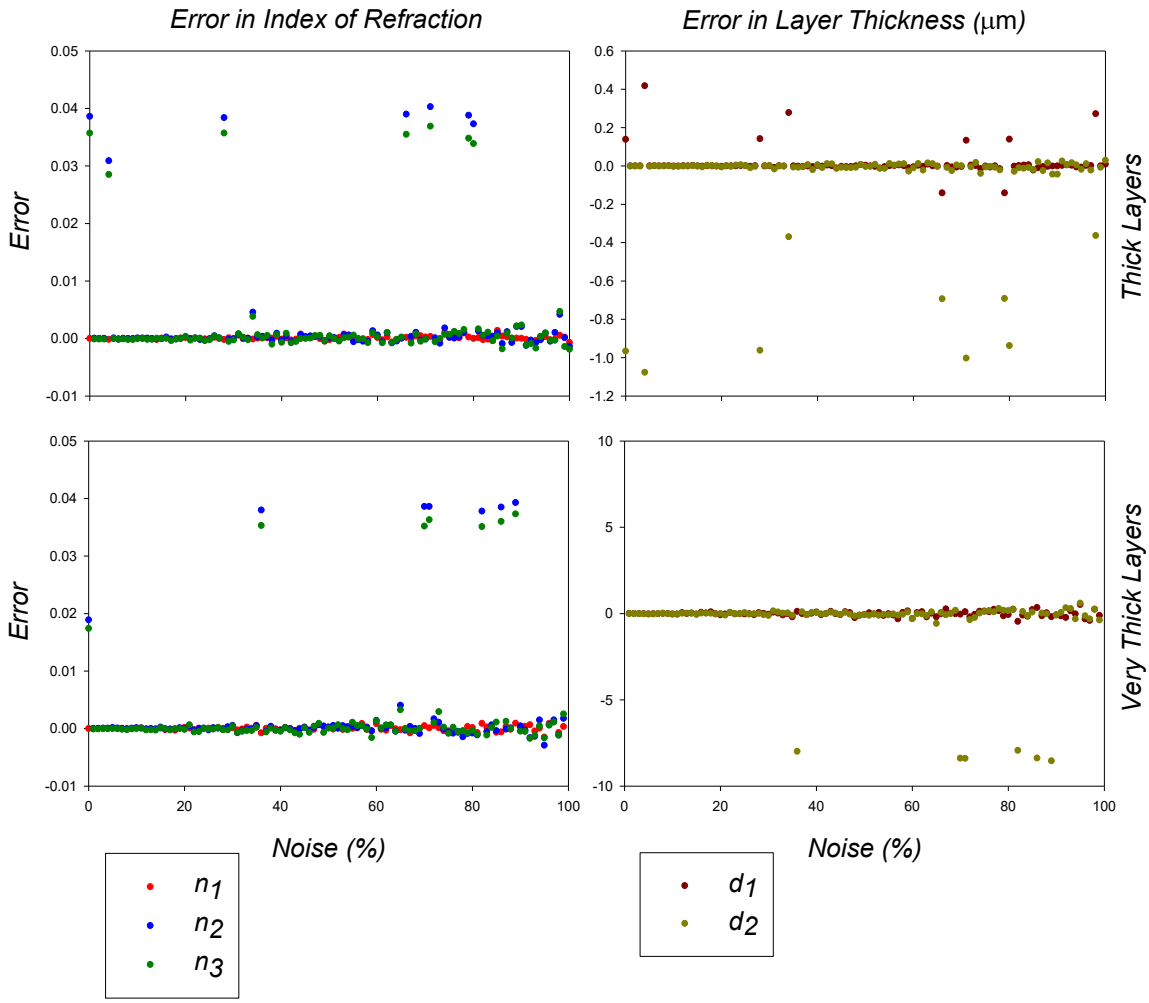

Figure 7.25: Impact of white noise on the accuracy of the second optimization method for the high contrast case. The left panes shows the error of the extracted index of refraction and on the right are shown the errors of the extracted thicknesses. Both a thick (top) and very thick (bottom) case are shown.

For the low contrast case, it can be seen from the top row of Figure 7.24 that for optically thick layers the system can tolerate noise up to 30% for all indices extraction with error less than 0.001. Within this region the average error for parameters n_1, n_2, n_3, d_1, d_2 are 2.82×10^{-6}, 4.43×10^{-6}, 1.11×10^{-5}, 5.94×10^{-5} μm and 3.60×10^{-5} μm respectively. For optically very thick layers on the bottom row, the acceptable range of noise is up to %36 where the average error of the

parameters are 7.10×10^{-7}, 1.02×10^{-5}, 1.97×10^{-5}, 3.23×10^{-4} μm and 2.34×10^{-3} μm. For the high contrast case, it can be seen from the top row of Figure 7.25 that for optically thick layers the system can tolerate noise up to 27% for all indices extraction with error less than 0.001 (excluding the first two outliers). Within this region the average error for parameters n_1, n_2, n_3, d_1, d_2 are 6.91×10^{-6}, 8.32×10^{-6}, 6.33×10^{-5}, 7.66×10^{-5} μm and 1.43×10^{-4} μm respectively. For optically very thick layers on the bottom row, the acceptable range of noise is up to 35% (excluding the first outlier) where the average error of parameters are 6.16×10^{-6}, 9.86×10^{-6}, 1.02×10^{-4}, 2.36×10^{-3} μm and 1.98×10^{-3} μm.

7.6. A Thin Layer Example

In order to test new methodology in optically thin layers with physical thicknesses on the order of a fraction of a wavelength, a very short coherence length is needed. This requires a very wide spectral source and therefore a very wide spectrometer bandwidth. As an illustrative example, we use a light source with 700 nm bandwidth that gives a coherence length of 0.4 μm. The source and spectrometer specification in this test are provided in Table 7.1.

Table 7.1: The light source and detection system specifications for optically thin layer test

Parameter	Symbol	Relation to other parameters	The value
The Light Source			
Central wavelength	$\lambda 0$		0.8 μm
Central wavenumber	$k0$	$\frac{2\pi}{\lambda 0}$	7.85 μm^{-1}
The source bandwidth	$\Delta\lambda_{FWHM}$		0.7 μm
The source bandwidth	Δk_{FWHM}	$\frac{\pi}{\sqrt{\ln(2)}}\frac{\Delta\lambda_{FWHM}}{\lambda 0^2}$	4.127 μm^{-1}
The coherence length (round trip)		$\frac{2\,ln(2)}{\pi}\frac{\lambda 0^2}{\Delta\lambda}$	0.4 μm

The Detection System			
Number of data points	N		4096
The Spectrometer bandwidth	$\Lambda\lambda$		1638 μm
The Spectrometer bandwidth	Λk	$k_{N-1} - k_0$	1570 μm^{-1}
The Spectrometer resolution	$\delta\lambda$	$\frac{\Lambda\lambda}{N-1}$	0.4 μm
The Spectrometer resolution	δk	$\frac{\Lambda k}{N-1}$	0.004 μm^{-1}
sampling frequency		$\frac{1}{\delta k}$	2.6×10^2 μm
detectable range	z_{max}	$\frac{\pi}{2\delta k}$	410 μm
Fourier transformed bin spacing (imaging resolution)	δz	$\frac{\pi}{N\delta k}$	0.2 μm

To investigate the behavior of the parameters error of the second optimization method, we recall the two layer test models with low and high contrast noted in Table 6.1 when the thicknesses are $d_{1,2} = 0.5$ μm. ε is swept between $\varepsilon_{1,2} = 0$ to $\varepsilon_{1,2} = 2$ μm in 0.02 μm increment. The test results are shown on Figure 7.26. In this figure the extracted parameter errors is plotted versus ε. The left panes show the error of the index of refraction and on the right are shown the error of the thicknesses. Both a low contrast (top) and high contract (bottom) case are shown.

only 100 searches were used in the algorithm to find the minimum RSS. The figure shows that the second optimization method works for optically thin samples for the range of $\varepsilon \approx 0.4$ μm. Higher range can be achieved with higher number of searches as was shown in Figure 7.5. For the region with $\varepsilon < 0.4$ μm, the extracted parameters error has the same order of magnitude as the thick and very thick case described in section 7.4.1 and the stable region of Figure 7.9.

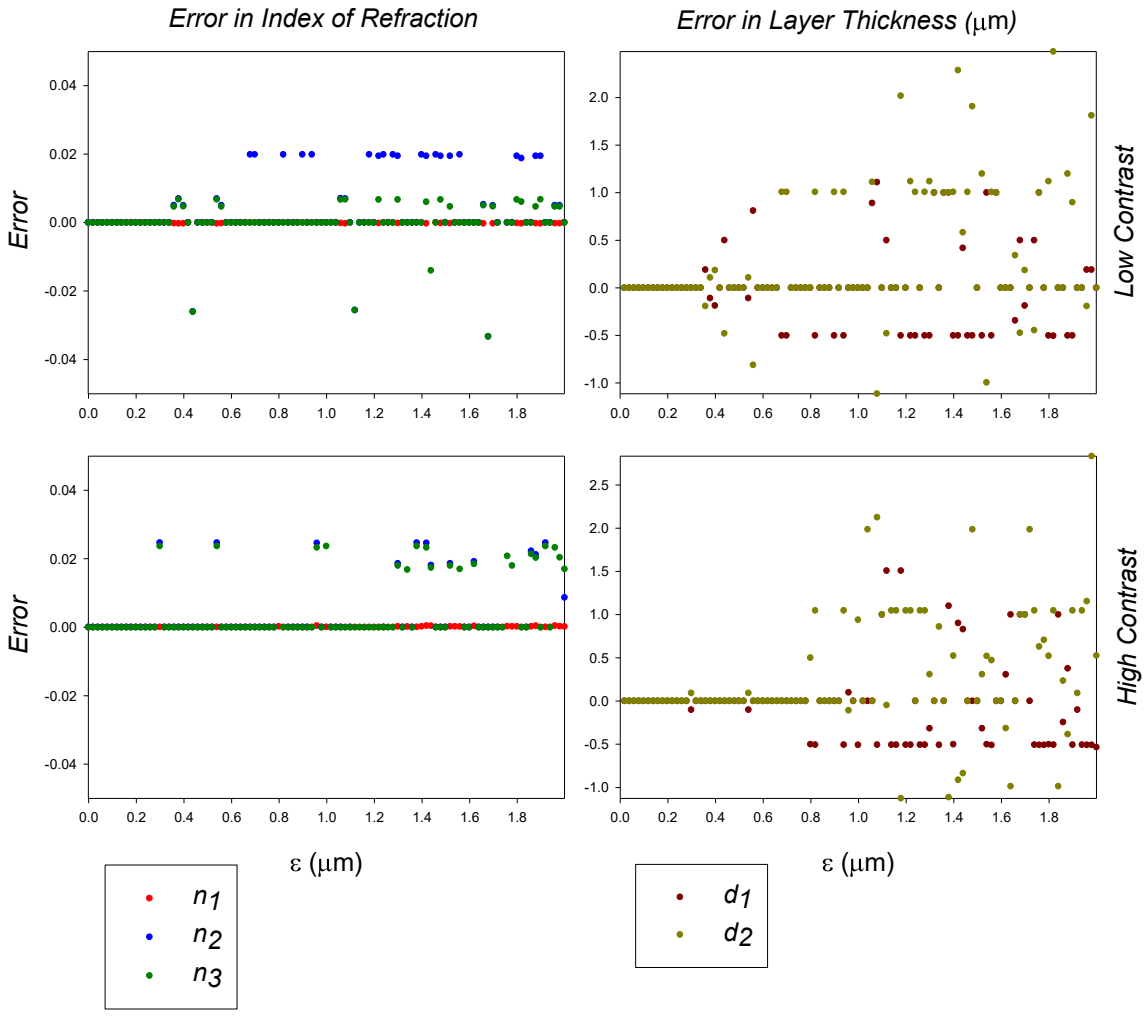

Figure 7.26: Impact of optical thickness errors (ε) on the accuracy of the second approach optimization results for optically thin layers system. The left panes shows the errors in index of refraction and on the right are shown the errors in the calculation of the thicknesses

7.7. A three layer example

In this section the second optimization method is applied to a three layer case to illustrate that this is generalizable. A low contrast test model is exampled here with the specifications as $n_0 = 1.337$, $n_1 = 1.345$ $n_2 = 1.351$, $n_3 = 1.345$, $n_4 = 1.337$ with thicknesses as $d_1 = 10$ μm, $d_2 = 30$ μm, $d_3 = 10$μm. The parameters to be extracted are the index and thickness of each layer and the last medium index of refraction i.e. $n_1, n_2, n_3, n_4, d_1, d_2, d_3$, assuming the front medium index of refraction is known. The test results are shown on Figure 7.27. In this figure the parameter errors (the deviation of the fitting parameters $\{b_i\}$ from their true values $\{n_i, d_i\}$) are plotted versus ε which is swept between $\varepsilon_{1,2,3} = 0$ to $\varepsilon_{1,2,3} = +1.00$ μm in 0.01 μm increment. The simulation results are shown in Figure 7.27. The left panes of Figure 7.27 show the error in the index of refraction and on the right is shown the error of the thicknesses. Since the second optimization algorithm in this test example must randomly check the RSS for three OTs, it is rather difficult to find the real minimum of the RSS with the same number of searches as of two layer systems. The number of searches for the test shown in Figure 7.27 was 1500 and the figure shows that it can support a range of ε up to ~0.5 μm. in order to extend this range up to 1 μm, the required number of searches has been estimated to be 6000 searches. From the data corresponding to Figure 7.27, the average error of extracted the indices n_1, n_2, n_3, n_4 are of the order of $\sim 10^{-11}$, $\sim 10^{-8}$, $\sim 10^{-7}$, $\sim 10^{-7}$ respectively and for the thicknesses d_1, d_2, d_3 the average error are $\sim 10^{-9}$, $\sim 10^{-6}$, $\sim 10^{-7}$ μm.

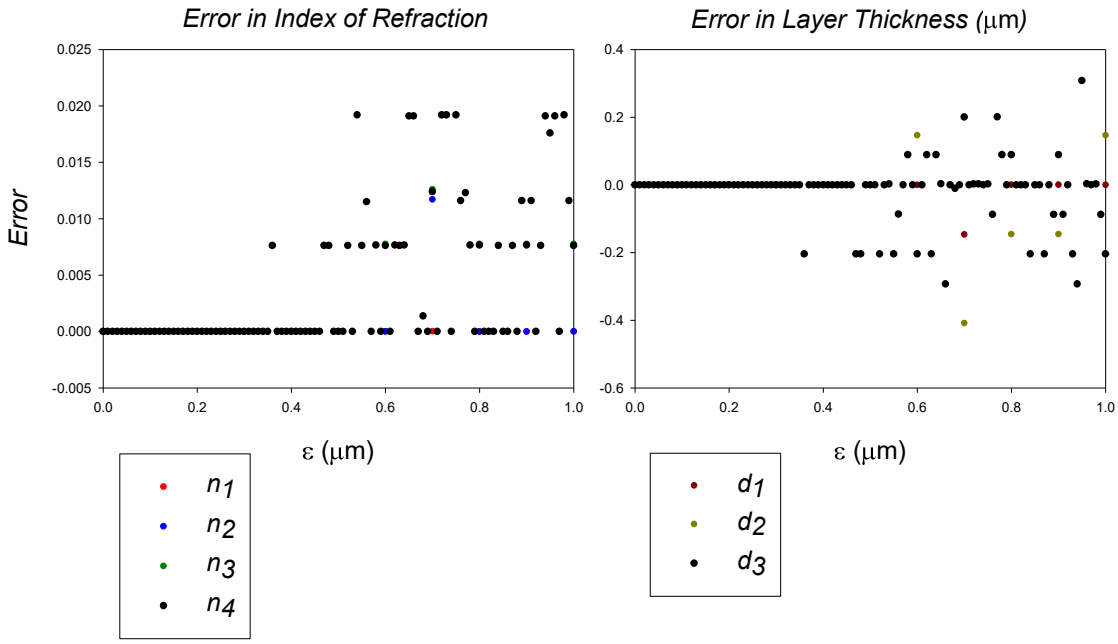

Figure 7.27: Impact of optical thickness errors (ε) on the accuracy of the second approach optimization results for a three layer system with low index contrasts. The left panes show the errors index of refraction and on the right are shown the errors in the calculation of the thicknesses. In this figure, the indices are $n_1 = 1.345$ $n_2 = 1.351$, $n_3 = 1.345$, $n_4 = 1.337$ and the thicknesses are $d_1 = 10$ μm , $d_2 = 30$ μm, $d_3 = 10$ μm.

Chapter 8. Conclusion and future works

To the best of the author's knowledge, the method for the simultaneous extraction of refractive index and thickness of multi layer systems as well as the methodology introduced for selecting the best spectral components are novel and the only method by now for extracting the object's optical parameters and morphology as well as the last medium index in a single experiment using only the object's spectral response available by any FD-OCT system without using any additional outside measurements.

Simulations show that the potential accuracy of the method is superior to all other approaches reported in the literature for biological applications. The accuracy depends significantly on the indices contrast of the object under the test because of the dependence on a layered sample model that ignores multiple reflections. In was shown in section 7.4.3 that through the second optimization method (section 7.4), all parameters of a two layer system and the last medium index of refraction can be obtained with accuracy of ± 0.001 and better when $n_1 < 1.55$ and $n_2 < 1.6$ which shows that this method can be a suitably work for biological applications. It was shown that the accuracy of the result is independent of the sample's thickness profile (section 7.4.2). Also the introduced method can tolerate large error in optical thickness measurement ε, the main input to the method for finding index and thickness, (section 7.4.1) and up to $\sim 30\%$ of white noise (section 7.5). The new method can be generalized to multi layer systems (>2) as shown by the example of a three layer system in section 7.7 and the general theoretical solution in section 4.3.

The test models in this thesis were assumed to be planar multilayer systems with solid (no thickness) and ideally flat interfaces. For biological applications these conditions are not usually fulfilled completely and thus an increase in the extracted parameters error is expected. Surfaces with roughness much smaller than the illuminating wavelength can be approximated as ideally flat. In this thesis the illuminating light central wavelength was 800 nm so any surface roughness of the nanometer scale can be considered flat and thus the test results presented in this thesis are still valid for them. The object's interfaces were also assumed to be solid with zero width. Some tests were done considering width of a few nanometer (i.e. <5 nm) as a hidden layer with the index the average of indices on both sides of the interface. The test results showed that the induced error in extracting parameters was not exceeding our defined tolerable error of ±0.001.

It was shown in this thesis that the index contrast is the main factor affecting the accuracy of the parameters extraction. This is due to inherent differences between the actual spectrum, modeled using the transfer matrix method (multiple scattering regime), and the theoretical modeled spectrum which uses the summation method (single scattering regime). The summation model ignores the loss of signal at each interface as well as the multiple reflections inside the sample. This problem may possibly be overcome by modifying the second optimization modeled signal (section 7.4) to take into account the loss of signal at each interface and multiple reflections (will be left for future work). Since the residual exists even with very low contrast test models, error is always associated with the extracted parameters and it increases with increasing index contrast. It was shown in section 7.4.3 that for

biological applications the parameters can be extracted within the defined tolerable error for models with refractive index <1.55. This implies that the maximum tolerable index contrast is in the range of $|1.55 - 1.337| = 0.233$.

Some practical implementation limitations need to be investigated more deeply to better understand the real limits of the solution the two most important are likely speckle noise and the impact of the focusing optical beam (non-uniform sample illumination). For an ideally flat interface locates at the focus of the lens in the sample arm, the speckle effect does not take place. The speckle effect occurs when light from a coherent source illuminates scatters separated by distances (laterally or axially) near that of the coherence length of the source. Therefore speckle can be observed when imaging rough surfaces or dense biological tissues. The impact of this multiple scattering regime on the interference spectrum can be modeled using the so-called extended Huygens-Fresnel principle (section 4.4.2). Multiple scattering causes a loss of spatial coherence of the sample field causing the alteration of the returning wavefront and reduction of the interference contrast. Speckle intensity thus depends on the number, size, optical properties and spatial distribution of scatterers. It was briefly discussed in section 6.2.2 that the result in the image is to degrade the sharpness of layer boundaries and reducing the image contrast near the boundaries that leads to increase the uncertainty in optical thickness measurement. This impact can be overcome by the second optimization method as discussed in section 7.4.1.

The proposed methodology, especially the selection of the best spectral components in section 6.2.1 is based on empirical examples and has not been

proven to be the best methodology and needs to be validated through a proper theoretical workup. Having said that, some of the works in this thesis need to be generalized and is left for future works. For example,

- Experimental verification of the method
- Formalizing the relation between the extracted parameters error and wavenumber components
- Improving the modeled signal to account for multiple reflections and support higher index contrast
- Developing a more realistic modeled signal spectrum in the second optimization method to include the multiple reflections effect and extend the application of the method to high contrast cases.
- Extend the method to non-biological applications
- Investigating the impact of the speckle noise and focusing beam on the signal spectrum and their impact on the extracted parameters.

Appendices

A. Derivation of the Determinant's roots

The matrix equation is solvable for those spectral components which do not result in a determinant of 0. To find out which frequencies are not suitable, the determinant given in Eq(4.13) is set to zero and solved for frequencies. The analysis is presented here for the cases when $\Delta_{rz_0} \neq 0$ and when $\Delta_{rz_0} = 0$.

A.1. Two layer system, Non-zero mismatch

The determinant in this case was given by Eq(4.13). The determinant is zero whenever two rows or columns are equal or linearly depend on each other. Also the determinant is zero whenever one row or column is zero. The first set of solutions is obtained when we equate the first and second columns together, we obtain

$$2k_i\Delta_{rz_0} = 2m_i\pi \pm 2k_i\left(\Delta_{rz_0} - \delta_1\right), \tag{A.1}$$

for $i = 1,2,3$. For the plus sign we obtain

$$k_i = \frac{m_i\pi}{\delta_1}, \tag{A.2}$$

or generally

$$\Delta k_{ij} = \left|k_i - k_j\right| = \frac{m\pi}{\delta_1}, \tag{A.3}$$

for $i, j = 1,2,3$. This relation tells that for value of k_1 given by Eq(A.2), if the other two frequencies follow the step given by (A.3), the determinant will be zero. For the minus sign in Eq(A.1) we obtain

$$k_i = \frac{m_i \pi}{2\Delta_{rz_0} - \delta_1}, \tag{A.4}$$

or

$$\Delta k_{ij} = \frac{m\pi}{2\Delta_{rz_0} - \delta_1}. \tag{A.5}$$

For equating the first and third column it is obtained

$$2k_i\Delta_{rz_0} = 2m_i\pi \pm 2k_i\left(\Delta_{rz_0} - \delta_1 - \delta_2\right). \tag{A.6}$$

For the plus sign it yield

$$k_i = \frac{m_i \pi}{\delta_1 + \delta_2}, \tag{A.7}$$

or

$$\Delta k_{ij} = \frac{m\pi}{\delta_1 + \delta_2}. \tag{A.8}$$

And for the minus sign of Eq(A.6), it is obtained that

$$k_i = \frac{m_i \pi}{2\Delta_{rz_0} - \delta_1 - \delta_2}, \tag{A.9}$$

or

$$\Delta k_{ij} = \frac{m\pi}{2\Delta_{rz_0} - \delta_1 - \delta_2}. \tag{A.10}$$

Similarly for equating the second and third columns we obtain

$$2k_i\left(\Delta_{rz_0} - \delta_1\right) = 2m_i\pi \pm 2k_i\left(\Delta_{rz_0} - \delta_1 - \delta_2\right). \tag{A.11}$$

For the plus sign it can be obtained that

$$k_i = \frac{m_i \pi}{\delta_2}, \tag{A.12}$$

or

$$\Delta k_{ij} = \frac{m\pi}{\delta_2}. \tag{A.13}$$

And for the minus sign

$$k_i = \frac{m_i \pi}{2\Delta_{rz_0} - 2\delta_1 - \delta_2}, \tag{A.14}$$

or

$$\Delta k_{ij} = \frac{m\pi}{2\Delta_{rz_0} - 2\delta_1 - \delta_2}. \tag{A.15}$$

Furthermore the determinant is zero when a column or a row is zero. Here we examine the condition in which a column is zero. If the first column is set to zero, one can obtain the following condition for the frequencies

$$k_i = \frac{(m_i + \frac{1}{2})\pi}{2\Delta_{rz_0}} = \frac{(2m_i + 1)\pi}{4\Delta_{rz_0}}. \tag{A.16}$$

This condition defines the first wavenumber value. The other wavenumbers must differ by the following steps

$$\Delta k_{ij} = \frac{m\pi}{2\Delta_{rz_0}}. \tag{A.17}$$

Similarly by setting the second column to zero, the wavenumbers must satisfy the following condition

$$k_i = \frac{(2m_i + 1)\pi}{4\left(\Delta_{rz_0} - \delta_1\right)}. \tag{A.18}$$

This condition fixes the first wavenumber and the other two frequencies must follow by the steps equal to

$$\Delta k_{ij} = \frac{m\pi}{2(\Delta_{rz_0} - \delta_1)}. \tag{A.19}$$

And finally from the third column we obtain that

$$k_i = \frac{(2m_i + 1)\pi}{4\left(\Delta_{rz_0} - \delta_1 - \delta_2\right)}, \tag{A.20}$$

with the steps for other frequencies given by

$$\Delta k_{ij} = \frac{m\pi}{2(\Delta_{rz_0} - \delta_1 - \delta_2)} \tag{A.21}$$

In summary there are nine sets of frequencies which are the roots of the determinant and listed in

Table 4.1.

A.2. Two layer system, Zero mismatch

A simpler case is when the mismatch arm's length is zero. The matrix in this case is

$$[P] = \begin{bmatrix} 1 & \cos 2k_1(\delta_1) & \cos 2k_1(\delta_1 + \delta_2) \\ 1 & \cos 2k_2(\delta_1) & \cos 2k_2(\delta_1 + \delta_2) \\ 1 & \cos 2k_3(\delta_1) & \cos 2k_3(\delta_1 + \delta_2) \end{bmatrix}. \tag{A.22}$$

Since all the elements of the first column are 1, the determinant is zero when all the elements of the second or the third column have the same value. For the second column elements to be equal, we obtain

$$2k_i(\delta_1) = 2m\pi \pm 2k_j(\delta_1), \tag{A.23}$$

for $i, j = 1,2,3$. For the plus sign we obtain

$$\Delta k_{ij} = \frac{m\pi}{\delta_1}. \tag{A.24}$$

Eq(A.24) states that for any value chosen for k_1, if the other wavenumber components follow the step of multiple integer of π/δ_1, the determinant will be zero. For the minus sign we obtain

$$k_j = \frac{m\pi}{\delta_1} - k_i, \tag{A.25}$$

this condition is the same as the one given by Eq(A.23).

A particular case is when all the elements of the second column are equal to ± 1. In this case we have

$$2k_i(\delta_1) = m_i\pi, \tag{A.26}$$

or

$$k_i = \frac{m_i\pi}{2\delta_1}. \tag{A.27}$$

This condition fixes one wavenumber and other frequencies follow the step given by

$$\Delta k_{ij} = \frac{m\pi}{2\delta_1}. \tag{A.28}$$

The difference between the conditions given by Eq(A.24) and (A.28) is that in the former case the first component can have any value but in the latter condition the first component is fixed. Another particular case is when all the elements of the second column are zero. In this case we have

$$2k_i(\delta_1) = (2m_i + 1)\frac{\pi}{2}, \tag{A.29}$$

or

$$k_i = (2m_i + 1)\frac{\pi}{4\delta_1}. \tag{A.30}$$

This condition fixes one wavenumber component and provides the step for others given by

$$\Delta k_{ij} = \frac{m\pi}{2\delta_1}. \tag{A.31}$$

The same argument can be applied to the third column. For general equality of the elements we obtain

$$\Delta k_{ij} = \frac{m\pi}{\delta_1 + \delta_2}. \tag{A.32}$$

For all the elements equal to ± 1, the first component is fixed at

$$k_i = \frac{m_i\pi}{2(\delta_1 + \delta_2)}, \tag{A.33}$$

and the others must follow the step given by

$$\Delta k_{ij} = \frac{m\pi}{2(\delta_1 + \delta_2)}. \tag{A.34}$$

And for all elements equal to zero, the first component is fixed at

$$k_i = (2m_i + 1)\frac{\pi}{4(\delta_1 + \delta_2)}, \tag{A.35}$$

and the others must follow the step given by

$$\Delta k_{ij} = \frac{m\pi}{2(\delta_1 + \delta_2)}. \tag{A.36}$$

The final set of condition is obtained when the elements of the second and the third column are equal. In this case

$$cos\, 2k_i(\delta_1) = cos\, 2k_i(\delta_1 + \delta_2), \tag{A.37}$$

where $i = 1,2,3$. This equation requires that

$$2k_i(\delta_1) = 2m_i\pi \pm 2k_i(\delta_1 + \delta_2). \tag{A.38}$$

For the plus sign we obtain

$$k_i = \frac{m_i\pi}{\delta_2}, \tag{A.39}$$

or generally

$$\Delta k_{ij} = \frac{m\pi}{\delta_2}. \tag{A.40}$$

This equation states that the determinant is zero if the first wavenumber is chosen from Eq(A.39) and the other two by steps given by Eq(A.40). For minus sign of Eq(A.38) we obtain

$$k_i = \frac{m_i\pi}{2\delta_1 + \delta_2}, \tag{A.41}$$

Or

$$\Delta k_{ij} = \frac{m\pi}{2\delta_1 + \delta_2}. \tag{A.42}$$

Again this equation states that the determinant is zero if the first wavenumber is chosen from Eq(A.41) and the other two by steps given by Eq(A.42).

In summary we have obtained eight set of solutions for the wavenumbers that make the determinant to be zero and hence the matrix equation would be unsolvable. Those are listed in Table A.1

Table A.1: Solution sets of the determinant's roots for zero mismatch case

Solution sets	Relations for The matrix components	k_1	k_2	k_3
1.	Column 2 $\equiv 0$	$\frac{(2m+1)\pi}{4\delta_1}$	$k_1 + \frac{m'\pi}{2\delta_1}$	$k_1 + \frac{m''\pi}{2\delta_1}$
2.	Column 2 $\equiv \pm 1$	$\frac{m\pi}{2\delta_1}$	$k_1 + \frac{m'\pi}{2\delta_1}$	$k_1 + \frac{m''\pi}{2\delta_1}$
3.	Column 3 $\equiv 0$	$\frac{(2m+1)\pi}{4(\delta_1+\delta_2)}$	$k_1 + \frac{m'\pi}{2(\delta_1+\delta_2)}$	$k_1 + \frac{m''\pi}{2(\delta_1+\delta_2)}$
4.	Columns 3 $\equiv \pm 1$	$\frac{m\pi}{2(\delta_1+\delta_2)}$	$k_1 + \frac{m'\pi}{2(\delta_1+\delta_2)}$	$k_1 + \frac{m''\pi}{2(\delta_1+\delta_2)}$
5.	Column 2 = Column3 (+sign)	$\frac{m\pi}{\delta_2}$	$k_1 + \frac{m'\pi}{\delta_2}$	$k_1 + \frac{m''\pi}{\delta_2}$
6.	Column 2 = Column3 (−sign)	$\frac{m\pi}{2\delta_1+\delta_2}$	$k_1 + \frac{m'\pi}{2\delta_1+\delta_2}$	$k_1 + \frac{m''\pi}{2\delta_1+\delta_2}$
7.	Column 3, equal elements	any else than set 3 and set 4	$k_1 + \frac{m'\pi}{(\delta_1+\delta_2)}$	$k_1 + \frac{m''\pi}{(\delta_1+\delta_2)}$
8.	Column 2, equal elements′	any else than set 1 and set 2	$k_1 + \frac{m'\pi}{\delta_1}$	$k_1 + \frac{m''\pi}{\delta_1}$

Solution sets given in Table A.1 can be represented in a more compact form. For example solution sets 1,2 and 8 can be expressed as for any initial component, the step for the others equal to $m\pi/2\delta_1$ will make the determinant zero. With the same argument, solution sets 3,4 and 7 can be united together. Therefore Table A.1 can be reduced to a more compact format as presented in Table 4.2

References

[1] J. Z. Wang, X. Liang, Q. Zhang, L. L. Fajardo, and H. Jiang, "Automated breast cancer classification using near-infrared optical tomographic images," J. Biomed. Opt., vol. 13, no. 4, p. 044001, Aug. 2008.

[2] S. Fantini, S. A. Walker, M. A. Franceschini, M. Kaschke, P. M. Schlag, and K. T. Moesta, "Assessment of the size, position, and optical properties of breast tumors in vivo by noninvasive optical methods," Appl. Opt., vol. 37, no. 10, pp. 1982–1989, Apr. 1998.

[3] Z. Wang, K. Tangella, A. Balla, and G. Popescu, "Tissue refractive index as marker of disease," J. Biomed. Opt., vol. 16, no. 11, Nov. 2011.

[4] O. Zhernovaya, O. Sydoruk, V. Tuchin, and A. Douplik, "The refractive index of human hemoglobin in the visible range," Phys. Med. Biol., vol. 56, no. 13, pp. 4013–4021, Jul. 2011.

[5] G. Mazarevica, T. Freivalds, and A. Jurka, "Properties of erythrocyte light refraction in diabetic patients," J. Biomed. Opt., vol. 7, no. 2, pp. 244–247, 2002.

[6] Y. Zhou, K. K. H. Chan, T. Lai, and S. Tang, "Characterizing refractive index and thickness of biological tissues using combined multiphoton microscopy and optical coherence tomography," Biomed. Opt. Express, vol. 4, no. 1, pp. 38–50, Dec. 2012.

[7] J. M. Schmitt, "Optical coherence tomography (OCT): a review," IEEE J. Sel. Top. Quantum Electron., vol. 5, no. 4, pp. 1205–1215, Jul. 1999.

[8] A. F. Fercher, C. K. Hitzenberger, G. Kamp, and S. Y. El-Zaiat, "Measurement of intraocular distances by backscattering spectral interferometry," Opt. Commun., vol. 117, pp. 43–48, Feb. 1995.

[9] G. Ha¨usler and M. W. Lindner, "'Coherence Radar' and 'Spectral Radar'—New Tools for Dermatological Diagnosis," J. Biomed. Opt., vol. 3, no. 1, pp. 21–31, 1998.

[10] S. R. Chinn, E. A. Swanson, and J. G. Fujimoto, "Optical coherence tomography using a frequency-tunable optical source," Opt. Lett., vol. 22, no. 5, p. 340, Mar. 1997.

[11] S. Yun, G. Tearney, J. de Boer, N. Iftimia, and B. Bouma, "High-speed optical frequency-domain imaging," Opt. Express, vol. 11, no. 22, p. 2953, Nov. 2003.

[12] G. Weiss, "Wave Propagation in a Turbulent Medium. V. I. Tatarski. Translated by R. A. Silverman. McGraw-Hill, New York, 1961. 285 pp. Illus. $9.75," Science, vol. 134, no. 3475, pp. 324–325, Aug. 1961.

[13] M. Born and E. Wolf, Principles of Optics: Electromagnetic Theory of Propagation, Interference and Diffraction of Light. CUP Archive, 2000.

[14] J. Goodman, Introduction to Fourier Optics, 3rd Edition edition. Englewood, Colo: Roberts and Company Publishers, 2004.

[15] V. I. Tatarski, Wave propagation in a turbulent medium. McGraw-Hill, 1961.

[16] L. A. Chernov, Wave propagation in a random medium. 1967.

[17] Lars Thrane, “Optical Coherence Tomography: Modeling and Applications.” Risø National Laboratory, Roskilde, Denmark.
[18] K. Iwata and R. Nagata, “Calculation of Refractive Index Distribution from Interferograms Using the Born and Rytov’s Approximation,” Jpn. J. Appl. Phys., vol. 14, no. S1, p. 379, Jan. 1975.
[19] Y. Sung, W. Choi, C. Fang-Yen, K. Badizadegan, R. R. Dasari, and M. S. Feld, “Optical diffraction tomography for high resolution live cell imaging,” Opt. Express, vol. 17, no. 1, p. 266, Jan. 2009.
[20] W. Choi, “Chapter 12 - Tomographic Phase Microscopy (TPM),” in Biomedical Optical Phase Microscopy and Nanoscopy, N. T. Shaked, Z. Zalevsky, and L. L. Satterwhite, Eds. Oxford: Academic Press, 2013, pp. 231–260.
[21] J. W. Goodman, Statistical Optics, 1 edition. New York: Wiley-Interscience, 2000.
[22] A. Kaufman, “Modeling the Ocean - Introduction to Wave Propagation in a Turbulent Medium,” Jan. 1976.
[23] M. Slaney, A. C. Kak, and L. E. Larsen, “Limitations of Imaging with First-Order Diffraction Tomography,” IEEE Trans. Microw. Theory Tech., vol. 32, no. 8, pp. 860–874, Aug. 1984.
[24] A. Devaney and J. Cheng, “Optical diffraction tomography in an inhomogeneous background medium,” Meas. Sci. Technol., vol. 19, no. 8, p. 085505, Aug. 2008.
[25] Emil Wolf, “Three-dimensional structure determination of semi-transparent objects from holographic data,” Optics Communications, vol. 1, no. 4, pp. 153–156.
[26] A. J. Devaney, “A Filtered Backpropagation Algorithm for Diffraction Tomography,” Ultrason. Imaging, vol. 4, no. 4, pp. 336–350, Oct. 1982.
[27] A. J. Devaney, “Inverse-scattering theory within the Rytov approximation,” Opt. Lett., vol. 6, no. 8, p. 374, Aug. 1981.
[28] R. Dändliker and K. Weiss, “Reconstruction of the three-dimensional refractive index from scattered waves,” Opt. Commun., vol. 1, no. 7, pp. 323–328, 1970.
[29] T. C. Wedberg and J. J. Stamnes, “Analytical and Numerical Examination of the Quantitative Imaging Properties of Optical Diffraction Tomography,” J. Mod. Opt., vol. 42, no. 9, pp. 1825–1836, Sep. 1995.
[30] A. F. Fercher, W. Drexler, and C. K. Hitzenberger, “OCT techniques,” 1996, vol. 2930, pp. 164–174.
[31] A. F. Fercher, “Optical coherence tomography,” J. Biomed. Opt., vol. 1, no. 2, pp. 157–173, 1996.
[32] F. Lexer, C. K. Hitzenberger, A. F. Fercher, and M. Kulhavy, “Wavelength-tuning interferometry of intraocular distances,” Appl. Opt., vol. 36, no. 25, p. 6548, Sep. 1997.
[33] Avinash C. Kak (last) and Malcolm Slaney, Principles of Computerized Tomographic Imaging. IEEE Press, 1988.

[34] M. Kaveh, M. Soumekh, and R. K. Mueller, “Tomographic imaging via wave equation inversion,” in Acoustics, Speech, and Signal Processing, IEEE International Conference on ICASSP ’82., 1982, vol. 7, pp. 1553–1556.
[35] A. C. Kak, “Computerized tomography with X-ray, emission, and ultrasound sources,” Proc. IEEE, vol. 67, no. 9, pp. 1245–1272, Sep. 1979.
[36] T. C. Wedberg and J. J. Stamnes, “Comparison of phase retrieval methods for optical diffraction tomography,” Pure Appl. Opt. J. Eur. Opt. Soc. Part A, vol. 4, no. 1, pp. 39–54, Jan. 1995.
[37] T. C. Wedberg and J. J. Stamnes, “Experimental examination of the quantitative imaging properties of optical diffraction tomography,” J. Opt. Soc. Am. A, vol. 12, no. 3, p. 493, Mar. 1995.
[38] T. C. Wedberg and W. C. Wedberg, “Tomographic reconstruction of the cross-sectional refractive index distribution in semi-transparent, birefringent fibres,” J. Microsc., vol. 177, no. 1, pp. 53–67, Jan. 1995.
[39] F. Charrière, A. Marian, F. Montfort, J. Kuehn, T. Colomb, E. Cuche, P. Marquet, and C. Depeursinge, “Cell refractive index tomography by digital holographic microscopy,” Opt. Lett., vol. 31, no. 2, p. 178, 2006.
[40] W. Singer, B. Dobler, H. Schreiber, K.-H. Brenner, and B. Messerschmidt, “Refractive-index measurement of gradient-index microlenses by diffraction tomography,” Appl. Opt., vol. 35, no. 13, p. 2167, May 1996.
[41] A. F. Fercher, R. Leitgeb, C. K. Hitzenberger, H. Sattmann, and M. Wojtkowski, “Complex spectral interferometry OCT,” 1998, vol. 3564, pp. 173–178.
[42] A. F. Fercher, W. Drexler, C. K. Hitzenberger, and T. Lasser, “Optical coherence tomography - principles and applications,” Rep. Prog. Phys., vol. 66, no. 2, p. 239, Feb. 2003.
[43] A. F. Fercher and C. K. Hitzenberger, “Chapter 4 - Optical coherence tomography,” in Progress in Optics, vol. 44, E. Wolf, Ed. Elsevier, 2002, pp. 215–302.
[44] P. H. Tomlins and R. K. Wang, “Simultaneous analysis of refractive index and physical thickness by Fourier domain optical coherence tomography,” IEE Proc. - Optoelectron., vol. 153, no. 5, p. 222, 2006.
[45] P. H. Tomlins and R. K. Wang, “Matrix approach to quantitative refractive index analysis by Fourier domain optical coherence tomography,” J. Opt. Soc. Am. A, vol. 23, no. 8, p. 1897, 2006.
[46] S. Chang, Y. Cheng, K. V. Larin, Y. Mao, S. Sherif, and C. Flueraru, “Optical coherence tomography used for security and fingerprint-sensing applications,” IET Image Process., vol. 2, no. 1, pp. 48–58, Feb. 2008.
[47] S. Chang, Y. Mao, G. Chang, and C. Flueraru, “Jade detection and analysis based on optical coherence tomography images,” Opt. Eng., vol. 49, no. 6, pp. 063602–063602–8, 2010.
[48] U. Morgner, W. Drexler, F. X. Kärtner, X. D. Li, C. Pitris, E. P. Ippen, and J. G. Fujimoto, “Spectroscopic optical coherence tomography,” Opt. Lett., vol. 25, no. 2, p. 111, Jan. 2000.

[49] P. D. J. Fujimoto and P. D. W. Drexler, “Introduction to Optical Coherence Tomography,” in Optical Coherence Tomography, P. D. W. Drexler and P. D. J. G. Fujimoto, Eds. Springer Berlin Heidelberg, 2008, pp. 1–45.
[50] W. Drexler, U. Morgner, F. X. Kärtner, C. Pitris, S. A. Boppart, X. D. Li, E. P. Ippen, and J. G. Fujimoto, “In vivo ultrahigh-resolution optical coherence tomography,” Opt. Lett., vol. 24, no. 17, p. 1221, Sep. 1999.
[51] S. Fuchs, A. Blinne, C. Rödel, U. Zastrau, V. Hilbert, M. Wünsche, J. Bierbach, E. Frumker, E. Förster, and G. G. Paulus, “Optical coherence tomography using broad-bandwidth XUV and soft X-ray radiation,” Appl. Phys. B, vol. 106, no. 4, pp. 789–795, Mar. 2012.
[52] D. Huang, E. A. Swanson, C. P. Lin, J. S. Schuman, W. G. Stinson, W. Chang, M. R. Hee, T. Flotte, K. Gregory, C. A. Puliafito, and A. Et, “Optical coherence tomography,” Science, vol. 254, no. 5035, pp. 1178–1181, Nov. 1991.
[53] A. F. Fercher, C. K. Hitzenberger, W. Drexler, G. Kamp, and H. Sattmann, “In vivo optical coherence tomography,” Am. J. Ophthalmol., vol. 116, no. 1, pp. 113–114, Jul. 1993.
[54] E. A. Swanson, J. A. Izatt, M. R. Hee, D. Huang, C. P. Lin, J. S. Schuman, C. A. Puliafito, and J. G. Fujimoto, “In vivo retinal imaging by optical coherence tomography,” Opt. Lett., vol. 18, no. 21, p. 1864, Nov. 1993.
[55] J. G. Fujimoto, C. Pitris, S. A. Boppart, and M. E. Brezinski, “Optical Coherence Tomography: An Emerging Technology for Biomedical Imaging and Optical Biopsy,” Neoplasia N. Y. N, vol. 2, no. 1–2, pp. 9–25, Jan. 2000.
[56] A. F. Fercher, W. Drexler, C. K. Hitzenberger, and G. Kamp, “Measurement of optical distances by optical spectrum modulation,” 1994, vol. 2083, pp. 263–267.
[57] N. Tan-no, T. Ichimura, T. Funaba, N. Anndo, and Y. Odagiri, “Optical multimode frequency-domain reflectometer,” Opt. Lett., vol. 19, no. 8, p. 587, Apr. 1994.
[58] J. Schwider and L. Zhou, “Dispersive interferometric profilometer,” Opt. Lett., vol. 19, no. 13, p. 995, Jul. 1994.
[59] S. R. Chinn, E. A. Swanson, and J. G. Fujimoto, “Optical coherence tomography using a frequency-tunable optical source,” Opt. Lett., vol. 22, no. 5, p. 340, Mar. 1997.
[60] M. A. Bail, G. Haeusler, J. M. Herrmann, M. W. Lindner, and R. Ringler, “Optical coherence tomography with the ‘spectral radar’: fast optical analysis in volume scatterers by short-coherence interferometry,” 1996, vol. 2925, pp. 298–303.
[61] R. Leitgeb, C. Hitzenberger, and A. Fercher, “Performance of fourier domain vs time domain optical coherence tomography,” Opt. Express, vol. 11, no. 8, p. 889, Apr. 2003.
[62] M. Choma, M. Sarunic, C. Yang, and J. Izatt, “Sensitivity advantage of swept source and Fourier domain optical coherence tomography,” Opt. Express, vol. 11, no. 18, p. 2183, Sep. 2003.
[63] J. F. de Boer, B. Cense, B. H. Park, M. C. Pierce, G. J. Tearney, and B. E. Bouma, “Improved signal-to-noise ratio in spectral-domain compared with

time-domain optical coherence tomography," Opt. Lett., vol. 28, no. 21, p. 2067, Nov. 2003.
[64] C. S. Seelamantula, M. L. Villiger, R. A. Leitgeb, and M. Unser, "Exact and efficient signal reconstruction in frequency-domain optical-coherence tomography," J. Opt. Soc. Am. A, vol. 25, no. 7, p. 1762, Jul. 2008.
[65] M. Wojtkowski, A. Kowalczyk, R. Leitgeb, and A. F. Fercher, "Full range complex spectral optical coherence tomography technique in eye imaging," Opt. Lett., vol. 27, no. 16, p. 1415, Aug. 2002.
[66] S. Chang, Y. Mao, C. Flueraru, and S. Sherif, "Optical coherence tomography: technology and applications," 2008, vol. 7156, pp. 715606–715606–9.
[67] R. A. Leitgeb, C. K. Hitzenberger, A. F. Fercher, and T. Bajraszewski, "Phase-shifting algorithm to achieve high-speed long-depth-range probing by frequency-domain optical coherence tomography," Opt. Lett., vol. 28, no. 22, p. 2201, Nov. 2003.
[68] F. Carreno and E. Bernabeu, "Statistical algorithm to obtain refractive index and thickness from spectrophotometric interference patterns," 1995, vol. 2208, pp. 77–87.
[69] F. Carreño, J. C. Martínez-Antón, and E. Bernabeu, "Optical interference method to obtain thickness and refractive indices of a uniaxial medium," Rev. Sci. Instrum., vol. 65, no. 8, pp. 2489–2493, Aug. 1994.
[70] P. Yeh, Optical Waves in Layered Media. 1988.
[71] O. S. Heavens, Optical Properties of Thin Solid Films. .
[72] Flory, Thin Films for Optical Systems. CRC Press, 1995.
[73] F. Abelès, "VI Methods for Determining Optical Parameters of Thin Films," in Progress in Optics, vol. 2, E. Wolf, Ed. Elsevier, 1963, pp. 249–288.
[74] F. Abelès, "La détermination de l'indice et de l'épaisseur des couches minces transparentes," J Phys Radium, vol. 11, no. 7, pp. 310–314, 1950.
[75] D. B. Kushev, N. N. Zheleva, Y. Demakopoulou, and D. Siapkas, "A new method for the determination of the thickness, the optical constants and the relaxation time of weakly absorbing semiconducting thin films," Infrared Phys., vol. 26, no. 6, pp. 385–393, Nov. 1986.
[76] D. A. Minkov, "Calculation of the optical constants of a thin layer upon a transparent substrate from the reflection spectrum," J. Phys. Appl. Phys., vol. 22, no. 8, p. 1157, Aug. 1989.
[77] T. Güngör and B. Saka, "Calculation of the optical constants of a thin layer upon a transparent substrate from the reflection spectrum using a genetic algorithm," Thin Solid Films, vol. 467, no. 1–2, pp. 319–325, Nov. 2004.
[78] J. C. Manifacier, J. Gasiot, and J. P. Fillard, "A simple method for the determination of the optical constants n, k and the thickness of a weakly absorbing thin film," J. Phys. [E], vol. 9, no. 11, p. 1002, Nov. 1976.
[79] R. Swanepoel, "Determination of the thickness and optical constants of amorphous silicon," J. Phys. [E], vol. 16, no. 12, pp. 1214–1222, Dec. 1983.
[80] S. Humphrey, "Direct calculation of the optical constants for a thin film using a midpoint envelope," Appl. Opt., vol. 46, no. 21, pp. 4660–4666, Jul. 2007.

[81] I. Ohlídal, “Immersion spectroscopic reflectometry of multilayer systems. I. Theory,” J. Opt. Soc. Am. A, vol. 5, no. 4, p. 459, Apr. 1988.
[82] I. Ohlídal and K. Navrátil, “Optical analysis of non-absorbing double layers by means of immersion reflectometry I: Liquid immersion method,” Thin Solid Films, vol. 67, no. 2, pp. 245–251, Aug. 1980.
[83] I. Ohlídal and K. Navrátil, “Optical analysis of non-absorbing double layers by means of immersion reflectometry II: Solid state immersion method,” Thin Solid Films, vol. 71, no. 1, pp. 91–102, Aug. 1980.
[84] I. Ohlídal, “General Formulae for the Optical Characterization of Single Layers with Spectroscopic Reflectometry,” J. Mod. Opt., vol. 35, no. 8, pp. 1373–1381, Aug. 1988.
[85] W. P. Ellis, “Immersion Spectrophotometry of Interference Films: Refractive Indices of Fluoride Films on Uranium Dioxide and Anodic Oxide Films on Uranium Metal,” J. Opt. Soc. Am., vol. 53, no. 5, p. 613, May 1963.
[86] W. P. Ellis, L. D. Allen, and A. D. Mulford, “Application of Immersion Reflectometry to the Study of Interference Layers,” Appl. Opt., vol. 8, no. 11, p. 2177, Nov. 1969.
[87] I. Fränz and W. Langheinrich, “The investigation of double layers in semiconductor technology,” Solid State Electron., vol. 13, pp. 807–814, Jun. 1970.
[88] I. Ohlídal, K. Navrátil, and V. Holý, “Immersion spectroscopic reflectometry of multilayer systems. II. Experimental results,” J. Opt. Soc. Am. A, vol. 5, no. 4, p. 465, Apr. 1988.
[89] W.-C. Kuo, Y.-K. Bou, and C.-M. Lai, “Simultaneous measurement of refractive index and thickness of transparent material by dual-beam confocal microscopy,” Meas. Sci. Technol., vol. 24, no. 7, p. 075003, Jul. 2013.
[90] Y.-S. Ghim and S.-W. Kim, “Dispersive white-light interferometry for thin-film thickness profile measurement,” 2005, vol. 5856, pp. 419–426.
[91] U. Schnell, E. Zimmermann, and R. Dandliker, “Absolute distance measurement with synchronously sampled white-light channelled spectrum interferometry,” Pure Appl. Opt. J. Eur. Opt. Soc. Part A, vol. 4, no. 5, p. 643, Sep. 1995.
[92] G. J. Tearney, M. E. Brezinski, J. F. Southern, B. E. Bouma, M. R. Hee, and J. G. Fujimoto, “Determination of the refractive index of highly scattering human tissue by optical coherence tomography,” Opt. Lett., vol. 20, no. 21, p. 2258, Nov. 1995.
[93] M. Ohmi, T. Shiraishi, H. Tajiri, and M. Haruna, “Simultaneous Measurement of Refractive Index and Thickness of Transparent Plates by Low Coherence Interferometry,” Opt. Rev., vol. 4, no. 4, pp. 507–515, Jul. 1997.
[94] M. Ohmi, Y. Ohnishi, K. Yoden, and M. Haruna, “In vitro simultaneous measurement of refractive index and thickness of biological tissue by the low coherence interferometry,” IEEE Trans. Biomed. Eng., vol. 47, no. 9, pp. 1266–1270, Sep. 2000.
[95] M. Haruna, M. Ohmi, T. Mitsuyama, H. Tajiri, H. Maruyama, and M. Hashimoto, “Simultaneous measurement of the phase and group indices and

the thickness of transparent plates by low-coherence interferometry," Opt. Lett., vol. 23, no. 12, p. 966, Jun. 1998.
[96] H. Maruyama, S. Inoue, T. Mitsuyama, M. Ohmi, and M. Haruna, "Low-Coherence Interferometer System for the Simultaneous Measurement of Refractive Index and Thickness," Appl. Opt., vol. 41, no. 7, p. 1315, Mar. 2002.
[97] T. Fukano and I. Yamaguchi, "Separation of Measurement of the Refractive Index and the Geometrical Thickness by Use Of A Wavelength-Scanning Interferometer with A Confocal Microscope," Appl. Opt., vol. 38, no. 19, p. 4065, Jul. 1999.
[98] K. Zhang, L. Tao, W. Cheng, J. Liu, and Z. Chen, "Air etalon facilitated simultaneous measurement of group refractive index and thickness using spectral interferometry," Appl. Opt., vol. 53, no. 31, pp. 7483–7486, Nov. 2014.
[99] S. Kim, J. Na, M. J. Kim, and B. H. Lee, "Simultaneous measurement of refractive index and thickness by combining low-coherence interferometry and confocal optics," Opt. Express, vol. 16, no. 8, p. 5516, Apr. 2008.
[100] H. Maruyama, T. Mitsuyama, M. Ohmi, and M. Haruna, "Simultaneous Measurement of Refractive Index and Thickness by Low Coherence Interferometry Considering Chromatic Dispersion of Index," Opt. Rev., vol. 7, no. 5, pp. 468–472, Sep. 2000.
[101] M. Ohmi, H. Nishi, Y. Konishi, Y. Yamada, and M. Haruna, "High-speed simultaneous measurement of refractive index and thickness of transparent plates by low-coherence interferometry and confocal optics," Meas. Sci. Technol., vol. 15, no. 8, p. 1531, Aug. 2004.
[102] T. Fukano and I. Yamaguchi, "Simultaneous measurement of thicknesses and refractive indices of multiple layers by a low-coherence confocal interference microscope," Opt. Lett., vol. 21, no. 23, p. 1942, Dec. 1996.
[103] X. Wang, C. Zhang, L. Zhang, L. Xue, and J. Tian, "Simultaneous refractive index and thickness measurements of bio tissue by optical coherence tomography," J. Biomed. Opt., vol. 7, no. 4, pp. 628–632, Oct. 2002.
[104] S. A. Alexandrov, A. V. Zvyagin, K. K. M. B. D. Silva, and D. D. Sampson, "Bifocal optical coherenc refractometry of turbid media," Opt. Lett., vol. 28, no. 2, pp. 117–119, Jan. 2003.
[105] A. Zvyagin, K. K. M. B. Silva, S. Alexandrov, T. Hillman, J. Armstrong, T. Tsuzuki, and D. Sampson, "Refractive index tomography of turbid media by bifocal optical coherence refractometry," Opt. Express, vol. 11, no. 25, pp. 3503–3517, Dec. 2003.
[106] G. Min, J. W. Kim, and B.-H. Lee, "The refractive index measurement technique based on the defocus correction method in full-field optical coherence tomography," 2012, vol. 8428, p. 84281M–84281M–7.
[107] G. Min, W. J. Choi, J. W. Kim, and B. H. Lee, "Refractive index measurements of multiple layers using numerical refocusing in FF-OCT," Opt. Express, vol. 21, no. 24, pp. 29955–29967, Dec. 2013.
[108] J. Jin, J. W. Kim, C.-S. Kang, J.-A. Kim, and T. B. Eom, "Thickness and refractive index measurement of a silicon wafer based on an optical comb," Opt. Express, vol. 18, no. 17, pp. 18339–18346, Aug. 2010.

[109] H.-C. Cheng and Y.-C. Liu, “Simultaneous measurement of group refractive index and thickness of optical samples using optical coherence tomography,” Appl. Opt., vol. 49, no. 5, p. 790, Feb. 2010.
[110] W. V. Sorin and D. F. Gray, “Simultaneous thickness and group index measurement using optical low-coherence reflectometry,” IEEE Photonics Technol. Lett., vol. 4, no. 1, pp. 105–107, Jan. 1992.
[111] Y.-P. Wang, D.-N. Wang, W. Jin, J.-P. Chen, X.-W. Li, and J.-H. Zhou, “Reflectometry measuring refractive index and thickness of polymer samples simultaneously,” J. Mod. Opt., vol. 53, no. 13, pp. 1845–1851, Sep. 2006.
[112] C.-T. Yen, J.-F. Huang, M.-J. Wu, Y.-F. Lee, C.-T. Huang, S.-F. Huang, and H.-C. Cheng, “Simultaneously measuring the refractive index and thickness of an optical sample by using improved fiber-based optical coherence tomography,” Opt. Eng., vol. 53, no. 4, pp. 044108–044108, 2014.
[113] Y.-S. Ghim and S.-W. Kim, “Thin-film thickness profile and its refractive index measurements by dispersive white-light interferometry,” Opt. Express, vol. 14, no. 24, p. 11885, 2006.
[114] S. J. Park, K. S. Park, Y. H. Kim, and B. H. Lee, “Simultaneous Measurements of Refractive Index and Thickness by Spectral-Domain Low Coherence Interferometry Having Dual Sample Probes,” IEEE Photonics Technol. Lett., vol. 23, no. 15, pp. 1076–1078, Aug. 2011.
[115] A. Hirai and H. Matsumoto, “Low-coherence tandem interferometer for measurement of group refractive index without knowledge of the thickness of the test sample,” Opt. Lett., vol. 28, no. 21, pp. 2112–2114, Nov. 2003.
[116] H. Matsumoto, K. Sasaki, and A. Hirai, “In situ measurement of group refractive index using tandem low-coherence interferometer,” Opt. Commun., vol. 266, no. 1, pp. 214–217, Oct. 2006.
[117] J. A. Izatt and M. A. Choma, “Theory of Optical Coherence Tomography,” in Optical Coherence Tomography, P. D. W. Drexler and P. D. J. G. Fujimoto, Eds. Springer Berlin Heidelberg, 2008, pp. 47–72.
[118] P. H. Tomlins and R. K. Wang, “Layer dependent refractive index measurement by Fourier domain optical coherence tomography,” 2006, vol. 6079, pp. 607913–607913–6.
[119] J. M. Schmitt and A. Knüttel, “Model of optical coherence tomography of heterogeneous tissue,” J. Opt. Soc. Am. A, vol. 14, no. 6, p. 1231, Jun. 1997.
[120] R. F. Lutomirski and H. T. Yura, “Propagation of a Finite Optical Beam in an Inhomogeneous Medium,” Appl. Opt., vol. 10, no. 7, p. 1652, Jul. 1971.
[121] A. R. Knuettel, R. Schork, and D. Boecker, “Analytical modeling of spatial resolution curves in turbid media acquired with optical coherence tomography (OCT),” 1996, vol. 2655, pp. 258–270.
[122] L. Thrane, H. T. Yura, and P. E. Andersen, “Analysis of optical coherence tomography systems based on the extended Huygens–Fresnel principle,” J. Opt. Soc. Am. A, vol. 17, no. 3, p. 484, 2000.
[123] K. Ohta and H. Ishida, “Matrix formalism for calculation of electric field intensity of light in stratified multilayered films,” Appl. Opt., vol. 29, no. 13, p. 1952, May 1990.

[124] P. Jansz, S. Richardson, G. Wild, and S. Hinckley, “Modeling of low coherence interferometry using broadband multi-Gaussian light sources,” Photonic Sens., vol. 2, no. 3, pp. 247–258, Jul. 2012.
[125] M. Wojtkowski, V. J. Srinivasan, T. H. Ko, J. G. Fujimoto, A. Kowalczyk, and J. S. Duker, “Ultrahigh-resolution, high-speed, Fourier domain optical coherence tomography and methods for dispersion compensation,” Opt. Express, vol. 12, no. 11, p. 2404, 2004.
[126] T. Marvdashti, H. Y. Lee, and A. K. Ellerbee, “High-resolution spectrometer: solution to the axial resolution and ranging depth trade-off of SD-OCT,” 2013, vol. 8572, p. 85720I–85720I–10.
[127] R. A. Leitgeb, W. Drexler, A. Unterhuber, B. Hermann, T. Bajraszewski, T. Le, A. Stingl, and A. F. Fercher, “Ultrahigh resolution Fourier domain optical coherence tomography,” Opt. Express, vol. 12, no. 10, p. 2156, 2004.
[128] M. A. Choma, K. Hsu, and J. A. Izatt, “Swept source optical coherence tomography using an all-fiber 1300-nm ring laser source,” J. Biomed. Opt., vol. 10, no. 4, pp. 044009–044009–6, 2005.
[129] B. Potsaid, B. Baumann, D. Huang, S. Barry, A. E. Cable, J. S. Schuman, J. S. Duker, and J. G. Fujimoto, “Ultrahigh speed 1050nm swept source / Fourier domain OCT retinal and anterior segment imaging at 100,000 to 400,000 axial scans per second,” Opt. Express, vol. 18, no. 19, pp. 20029–20048, Sep. 2010.
[130] S.-W. Lee, H.-W. Jeong, B.-M. Kim, Y.-C. Ahn, W. Jung, and Z. Chen, “Optimization for Axial Resolution, Depth Range, and Sensitivity of Spectral Domain Optical Coherence Tomography at 1.3 μm,” J. Korean Phys. Soc., vol. 55, no. 6, pp. 2354–2360, Dec. 2009.
[131] A. Davila, J. M. Huntley, C. Pallikarakis, P. D. Ruiz, and J. M. Coupland, “Wavelength scanning interferometry using a Ti:Sapphire laser with wide tuning range,” Opt. Lasers Eng., vol. 50, no. 8, pp. 1089–1096, Aug. 2012.
[132] B. Liu and M. E. Brezinski, “Theoretical and practical considerations on detection performance of time domain, Fourier domain, and swept source optical coherence tomography,” J. Biomed. Opt., vol. 12, no. 4, p. 044007, Aug. 2007.
[133] M. Wojtkowski, R. Leitgeb, A. Kowalczyk, T. Bajraszewski, and A. F. Fercher, “In vivo human retinal imaging by Fourier domain optical coherence tomography,” J. Biomed. Opt., vol. 7, no. 3, pp. 457–463, 2002.
[134] P. Andretzky, M. W. Lindner, J. M. Herrmann, A. Schultz, M. Konzog, F. Kiesewetter, and G. Haeusler, “Optical coherence tomography by spectral radar: dynamic range estimation and in-vivo measurements of skin,” 1999, vol. 3567, pp. 78–87.
[135] Z. Yaqoob, J. Wu, and C. Yang, “Spectral domain optical coherence tomography: a better OCT imaging strategy,” BioTechniques, vol. 39, no. 6 Suppl, pp. S6–13, Dec. 2005.
[136] E. W. Weisstein, “Hadamard’s Maximum Determinant Problem.” [Online]. Available: http://mathworld.wolfram.com/HadamardsMaximumDeterminantProblem.html. [Accessed: 18-Nov-2015].

[137] X. Zhang, S. Yousefi, L. An, and R. K. Wang, “Automated segmentation of intramacular layers in Fourier domain optical coherence tomography structural images from normal subjects,” J. Biomed. Opt., vol. 17, no. 4, pp. 0460111–0460117, 2012.
[138] D. C. Adler, T. H. Ko, and J. G. Fujimoto, “Speckle reduction in optical coherence tomography images by use of a spatially adaptive wavelet filter,” Opt. Lett., vol. 29, no. 24, p. 2878, 2004.